

**VOL II**

## Volume II

LMSC-A964947

1969 DEC 31

VOL II

# HIGH-PERFORMANCE THERMAL PROTECTION SYSTEMS

CONTRACT NAS 8-20758

FINAL REPORT

Volume II

PREPARED FOR  
NASA MARSHALL SPACE FLIGHT CENTER  
HUNTSVILLE, ALABAMA

PROPULSION VEHICLE SYSTEMS

LOCKHEED MISSILES & SPACE COMPANY / SUNNYVALE, CALIFORNIA

PRECEDING PAGE BLANK NOT FILMED.

CONTENTS\*  
APPENDIX

Appendixes		Page
A	BIBLIOGRAPHY OF LITERATURE SURVEY MATERIALS	A-1
✓ B	THERMAL PROTECTION SYSTEM ENVIRONMENTS FOR THE MODULAR NUCLEAR VEHICLE	B-1
✓ C	DERIVATION OF ONE-DIMENSIONAL HEAT TRANSFER RELATION IN MULTILAYER COMPOSITES	C-1
✓ D	FLAT PLATE CALORIMETER APPARATUS	D-1
✓ E	CALORIMETRIC EMITTANCE AND REFLECTANCE MEASURING EQUIPMENT	E-1
✓ F	PROPOSED SPECIFICATION FOR REFLECTIVE-SHIELD EMITTANCE	F-1
✓ G	COMPUTER CODES USED IN STRESS AND THERMAL ANALYSIS	G-1
✓ H	GAS FLOW APPARATUS	H-1
✓ I	TASK 5 OUTGASSING APPARATUS AND GAS ANALYSIS DATA	I-1
✓ J	A METHOD FOR ESTIMATING "AS-INSTALLED" THERMAL CONDUCTIVITY VALUES	J-1
✓ K	SAMPLE EFFECTIVE WEIGHT PENALTY CALCULATIONS	K-1

\*Volume I contains the Information and Summary and Tasks 1 through 7.

PRECEDING PAGE BLANK NOT FILMED

PRECEDING PAGE BLANK NOT FILMED.

## APPENDIX ILLUSTRATIONS

Figure		Page
B-1	Saturn V Two-Stage-to-Orbit Ambient Pressure vs. Flight Time	B-2
B-2	Saturn V Two-Stage-to-Orbit Acceleration vs. Flight Time	B-3
B-3	Meteoroid Shield External Variation During Mars Transfer	B-8
C-1	Variation of Mean Free Path for Air and Helium With Pressure for Temperatures of 200° and 500° R	C-9
C-2	Thermal Conductivity of Air and Helium as a Function of Pressure for Several Characteristic Void Dimensions and Temperature	C-10
C-3	Variation of Thermal Conductivity With Temperature for a Restricted Gas at Low Pressure	C-12
C-4	Prediction Temperature Distribution Through Multilayer Insulation	C-17
C-5	Effective Conductivity With Solid and Radiative Components - NRC-2	C-20
D-1	Flat-Plate Calorimeter Schematic Diagram	D-2
D-2	Flat-Plate Calorimeter	D-3
D-3	Wet-Test Flow Meter Correction	D-6
D-4	Apparatus Configuration for Heat-Leak Test	D-6
D-5	Comparison of Ratio of Electrical Heat Input to Calorimeter to Heat Input Measured From Boiloff Data as a Function of Heat Input	D-8
E-1	Schematic Drawing of Calorimetric Apparatus for Total Hemispherical Emittance	E-2
E-2	Cary Spectrophotometer	E-9
E-3	Lion Research Corporation Optical Surface Comparator	E-14
H-1	Schematic of Gas Flow Apparatus	H-2
H-2	Assembly of Gas Flow Apparatus	H-3
H-3	Spider Fitting at Lower End of Gas Flow Apparatus Test Drum	H-4

Figure		Page
I-1	Outgassing Apparatus Schematic	I-2
I-2	Insulation Specimen in Base of Vacuum Chamber	I-3
I-3	Outgassing Vacuum Test Chamber With Coolant Chamber in Place	I-3
I-4	MKS Baratron Electronic Pressure Gage	I-5
I-5	Connection Schematic of Baratron Absolute Gage	I-6
I-6	Installation of Pressure Pickups and Reference Vacuum System	I-7
I-7	Partial-Pressure Gage Gas Analyzer	I-9
I-8	Outgassing Apparatus and Data Acquisition System	I-11
I-9	Emph Chamber Gas Analysis	I-16
I-10	Background Scan For Gage Region	I-17
I-11	Test 1 - Partial Pressure Gage Scans at Four Different Times from Initiation of Pumpdown for Off-Shelf Double Aluminized Mylar at 530° R: Part A	I-18
I-12	Test 1 - Partial Pressure Gage Scans at Four Different Times from Initiation of Pumpdown for Off-Shelf Double Aluminized Mylar at 530° R: Part B	I-19
I-13	Test 1 - Partial Pressure Gage Scans at Four Different Times From Initiation of Pumpdown for Off-Shelf Double Aluminized Mylar at 530° R: Part C	I-20
I-14	Test 1 - Partial Pressure Gage Scans at Four Different Times From Initiation of Pumpdown for Off-shelf Double Aluminized Mylar at 530° R: Part D	I-21

## TABLES

Table		Page
B-1	Acoustic Environment for Modular Nuclear Vehicle Tank Bottom - Dome Insulation	B-4
B-2	Acoustic Environment for Modular Nuclear Vehicle Tank Cylindrical Insulation Section	B-5
B-3	Neutron Number and Energy Currents Into Tank Bottom Insulation	E-10
B-4	Gamma Ray Energy Current Into Tank Bottom Insulation	B-10
F-1	Comparison of Lion Emittance With Total Hemispherical Emittance	F-2
F-2	Comparison of Short-Wavelength Reflectances	F-3

Appendix A  
BIBLIOGRAPHY OF LITERATURE SURVEY MATERIALS

The publications cited in this appendix were reviewed during the literature survey of data pertaining to high-performance insulation.

A.1 COMPANY PUBLICATIONS

Air Force Materials Laboratory, Aeronautical Systems Div., Air Force Systems Command, Thermal Insulations for Aerospace Applications: -423 to 3000° F, by M. L. Minges, ASD TDR 63 699, DDC AD-425 704, Wright-Patterson AFB, Ohio, Sep 1963

Boeing Company, Advances in the Materials Technology Resulting From the X-20 Program, Final Report, by W. K. Stratton et al., AFML-TR-64-396, Seattle, Wash, Mar 1965

Douglas Aircraft Company, System Effects on Propellant Storability and Vehicle Performance, Final Technical Report, by G. W. Burge, DAC-59314, AFRPL TR-66-258, Oct 1966

General Dynamics/Astronautics, Investigation of Potential Low Temperature Insulators, by J. Hertz, Report GD-A-ERR-AN-668, 31 Dec 1964

General Dynamics/Convair, Cryogenic Insulation Development, Quarterly Progress Report, by R. C. Getty, NASA-CR-80456, Report 584-4-3, San Diego, Calif., 10 Oct 1966

-----, Superinsulation Research Program, Progress Report, by J. P. Clay, R. C. Getty, T. D. Lange et al., GD/C-ERR-AN-863, San Diego, Calif., Dec 1965

General Dynamics/Nuclear Aerospace Research Facility, Evaluation of Cryogenic Insulation Materials and Composites for Use in Nuclear Radiation Environments,

Quarterly Progress Report, by E. E. Kerlin and R. P. Lightfoot, NASA-CR-83058, FZK-328, Fort Worth, Tex., 15 Jan 1967

General Electric Company, Planetary Vehicle Thermal Insulation Systems, Phase I Summary Report, 67504289, 3 Mar 1967

Goodyear Aerospace Corporation, Development of Materials and Materials Application Concepts for Joint Use as Cryogenic Insulation and Micrometeorite Bumpers, GER 11676 S/24, 30 Jun 1966

-----, Development of Materials and Materials Application Concepts for Joint Use as Cryogenic Insulation and Micrometeorite Bumpers, GER 11676 S/36, 30 Jun 1967

Linde Company, Division of Union Carbide Corp., Investigation of a Lightweight Self-Evacuating Prefabricated Multilayer Insulation System for Cryogenic Space Propulsion Stages, by L. R. Niendorf, Tonawanda, N.Y., Monthly Progress Reports

- 1, NASA X65-91695, 16 Jul 1965
- 2, NASA X65-92050, 17 Aug 1965
- 3, NASA X66-90295, 18 Oct 1965
- 4, NASA X66-90731, 18 Nov 1965
- 7, NASA X66-92942, 18 Apr 1966
- 9, NASA X66-93747, 17 Jun 1966

-----, Investigation of a Lightweight Self-Evacuating Prefabricated Multilayer Insulation System for Cryogenic Space Propulsion Stages, Final Report, by L. R. Niendorf, and G. E. Nies, NASA-CR-72012, Tonawanda, N. Y., 15 July 1966

-----, Linde Company Superinsulation Applied to Space Vehicles, by C. R. Lindquist, Tonawanda, N.Y., 1 Dec 1962

-----, Self-Evacuated Multilayer Insulation of Lightweight Prefabricated Panels for Cryogenic Space Propulsion Vehicles, by P. J. Perkins, R. P. Dengler, L. R. Niendorf, and G. E. Nies, NASA-TM-X-52266 (presented at the 8th Struct. Structural Dynm. and Mater. Conf., sponsored by AIAA, Palm Springs, Calif., 29-31 Mar 1967)

Little, Arthur D., Incorporated, Advanced Studies on Multilayer Insulation Systems, First Quarterly Progress Report, ADL-67180-00-01, Cambridge, Mass, Jun 1965



-----, Advanced Studies on Multilayer Insulation Systems, Final Report, NASA CR-54929, Cambridge Mass., 1 Jun 1966

-----, Basic Investigations of Multilayer Insulation Systems, Final Report, NASA CR-54191, Cambridge, Mass., 30 Oct 1964

-----, Design and Optimization of Space Thermal Protection for Cryogenics-Analytical Techniques and Results, by J. M. Bonneville, ADL-65958-02-01, Cambridge, Mass.

-----, Design of Thermal Protection Systems for Liquid Hydrogen Tanks, ADL 65008-03-01, Cambridge, Mass., Apr 1963

-----, Insulated Tank Program, Monthly Progress Report, NASA-CR-58747, Cambridge, Mass., 12 Aug 1964

-----, Liquid Propellant Losses During Space Flight, Quarterly Progress Report, NASA X63-14200, Cambridge, Mass., Jan 1963

-----, Liquid Propellant Losses During Space Flight, Quarterly Progress Report, 65008-00-02, Cambridge, Mass., Apr 1963

-----, Liquid Propellant Losses During Space Flight, Final Report, 65008-00-04, NASA-CR-53336, Cambridge, Mass., Oct 1964

-----, The Development of High Performance Insulation Systems, ADL C-62458, Cambridge, Mass., Apr 1963

Lockheed Missiles & Space Company, A Study of Thermal Conductivity Requirements, First Quarterly Progress Report, LMSC-A784511, Sunnyvale, Calif., 30 Jul 1967

-----, Development of Thermal Protection System for a Cryogenic Spacecraft Module, First Quarterly Progress Report, by W. H. Sterbentz, LMSC-A703794, Sunnyvale, Calif., 1964

-----, Development of Thermal Protection System for a Cryogenic Spacecraft Module, Second Quarterly Progress Report, by J. W. Baxter, LMSC-A729936, Sunnyvale, Calif., 15 Jan 1965

-----, Elevated Temperature Multiple Layer Insulation Study, Interim Technical Report, by G. R. Cunningham, A. Funai, and A. Lindahn, Contract NAS 2-2441, LMSC 4-05-66-4, Sunnyvale, Calif., Nov 1966

-----, Handbook of Thermal Design Data for Multilayer Insulation Systems, by R. T. Parmley, LMSC-A742593, Sunnyvale, Calif., 11 Aug 1965

-----, Handbook of Thermal Design Data for Multilayer Insulation Systems, Vol. II, LMSC-A847882, Sunnyvale, Calif., 25 Jun 1967

-----, Performance of Multilayer Insulation Systems for the 300° to 800° K Temperature Range, Materials Report No. 1, NAS 2-2441, LMSC 4-05-65-9, Sunnyvale, Calif., Aug 1965

-----, Performance of Multilayer Insulation Systems for Temperatures to 700° K, Final Report, by G. R. Cunningham et al., Report 4-05-67-17, Palo Alto, Calif., May 1967

-----, Study on High-Performance Insulation Thermal Design Criteria, Second Quarterly Progress Report, by R. M. Coston, J. J. Brogan, and J. H. Guill, LMSC-A837978, Sunnyvale, Calif., 15 Oct 1966

-----, Thermal Protection System for a Cryogenic Spacecraft Propulsion Module, Vol. 1, by W. H. Sterbentz and J. W. Baxter, LMSC A794993, Sunnyvale, Calif., 15 Nov 1966

-----, Thermal Protection System for a Cryogenic Spacecraft Propulsion Module, Vol. 2, by W. H. Sterbentz and J. W. Baxter, LMSC A794993, Sunnyvale, Calif., 15 Nov 1966

Martin Company, Structure Department, Cryogenic Insulation Research, Final Report, by R. F. Crawford and R. G. Hannah, NASA-CR-61162, Baltimore, Md., 23 Jan 1967

-----, Design Techniques for Structures Cryogenic Insulation Investigations, Report MAR ER 13502, Baltimore, Md., Oct 1964

Midwest Research Institute, Thermophysical Properties of Thermal Insulating Materials, by J. B. Loser, C. E. Moeller, and M. B. Thompson, ML TDR 64 5, ASD TDR62 215 rev, Kansas City, Mo., Apr 1964

National Research Corporation, Development of Techniques and Hardware for Insulation Wrappings of Cryogenic Containers, Eighth Quarterly Progress Report, by

Malcolm E. Reed, NASA-CR-69538, Cambridge, Mass., Dec 1965

Super-Temp Corporation, Cryogenic Division, Communique, Oct 1966

## A.2 JOURNAL ARTICLES AND BOOKS

Black, L. A. and P. E. Glaser, "Effects of Compressive Loads on the Heat Flux Through Multilayer Insulations," Adv. in Cryo. Eng., Vol. 11, 1965, pp. 26-34

Costen, R. M., "Experimental Evaluation of the Equations and Parameters Governing Flow Through Multilayer Insulations During Evacuation," Adv. in Cryo. Eng., Vol. 11, 1965, pp. 56-64

Getty, R. C., J. P. Clay, E. J. Kremzier, and K. E. Leonhard, "Experimental Evaluation of Some Selected Lightweight Superinsulation for Space Vehicles," Adv. in Cryo. Eng., Vol. 11, 1965, pp. 35-48

Glaser, P. E., "Cryogenic Insulations," Mach. Des., Vol. 39, No. 19, 17 Aug 1967, pp. 146-152

Ishaghoff, I. and J. M. Canty, "Quilted Superinsulation," Adv. in Cryo. Eng., Vol. 9, 1963, pp. 46-51

Light, J. S., "Recent Techniques for Insulation in Space Environment," Appl. Adv. Nuc. Phys. Test. Mat., No. 373, 1965, pp. 127-134

Matsch, L. C., "Advances in Multilayer Insulations," Adv. in Cryo. Eng., Vol. 7, 1961, pp. 413-418

Middleton, R. L. et al., "Development of a Lightweight External Insulation System for Liquid-Hydrogen Stages of the Saturn V Vehicle," Adv. in Cryo. Eng., Vol. 10, 1964, pp. 153-160

Moeller, C. E., "Spacecraft Demands Bring New Thermal Insulations," Prod. Eng., Vol. 37, No. 4, 14 Feb 1966, pp. 91-95

Parmley, R. T., D. R. Elgin, and R. M. Coston, "Shingle Multilayer Insulation for Space Vehicles Using Cryogenic Fluids," Adv. in Cryo. Eng., Vol. 11, 1965, pp. 16-25

Perkins, P. J., M. A. Colaluca, and L. S. Smith, "Preliminary Test Results on a Compressed Multilayer Insulation System for a Liquid-Hydrogen-Fueled Rocket," Adv. in Cryo. Eng., Vol. 9, 1963, pp. 38-45

Price, J. W. and T. G. Lee, "Analysis, Design, and Testing of Heat-Short-Isolation Components for High-Performance Insulation System," Adv. in Cryo. Eng., Vol. 12, 1966, pp. 265-273

Ruccia, F. E., R. B. Hinckley, and R. C. Reid, "Thermal Performance of Tank Applied Multilayer Insulations," Adv. in Cryo. Eng., Vol. 12, 1966, pp. 218-228

Streed, E. R., C. R. Cunningham, and C. A. Zierman, "Performance of Multilayer Insulation Systems for the 300° to 800° K Temperature Range," Prog. in Astro & Aero., Vol. 18, 1966, pp. 735-771

Swalley, F. E. and C. D. Nevins, "Practical Problems in Design of High-Performance Multilayer Insulation System for Cryogenic Stages," Adv. in Cryo. Eng., Vol. 10, 1964, pp. 208-215

Thomas, M. and W. Weitzman, "A Comparison of Shroud-Mounted With Tank-Mounted High-Performance Insulation," Adv. in Cryo. Eng., Vol. 12, 1966, pp. 239-249

Wang, D. I., "Multiple Layer Insulations," Aerodynamically Heated Structures, P. E. Glaser, ed., Prentice-Hall, Inc., 1962, p. 45

N70-80603

## **Appendix B**

### **THERMAL PROTECTION SYSTEM ENVIRONMENTS FOR THE MODULAR NUCLEAR VEHICLE**

Throughout the course of the contract program considerable environmental data were used as the bases for selection of material and for compatibility with designs of insulation assemblies and support structure for the Modular Nuclear Vehicle (MNV). The ground rules and assumptions employed in this program are presented in this appendix.

#### **AMBIENT PRESSURE**

Data provided in the contract document (Ref. B-1) established the pressure history for a Saturn V two-stage-to-orbit flight. This is shown in Fig. B-1. Gas evacuation experiments in Task 6 are based on a pressure-time profile which exceeds the slope of Fig. B-1 data.

#### **VEHICLE ACCELERATION**

Acceleration data for a Saturn V two-stage-to-orbit flight was also presented in the contract document (Ref B-1). Figure B-2 presents the data. The maximum acceleration of 5 g occurs at 160 sec. Rebound acceleration can occur at staging. A maximum value of 2.5 g was used in Task 2 as applied to structural support designs.

#### **ACOUSTIC ENVIRONMENT**

The insulation must maintain structural integrity during exposure to Saturn V external sound pressure levels during the liftoff and boost phases of flight. Sound pressure levels anticipated for the MNV are presented in Tables B-1 and B-2 (Refs. B-2 and B-3).

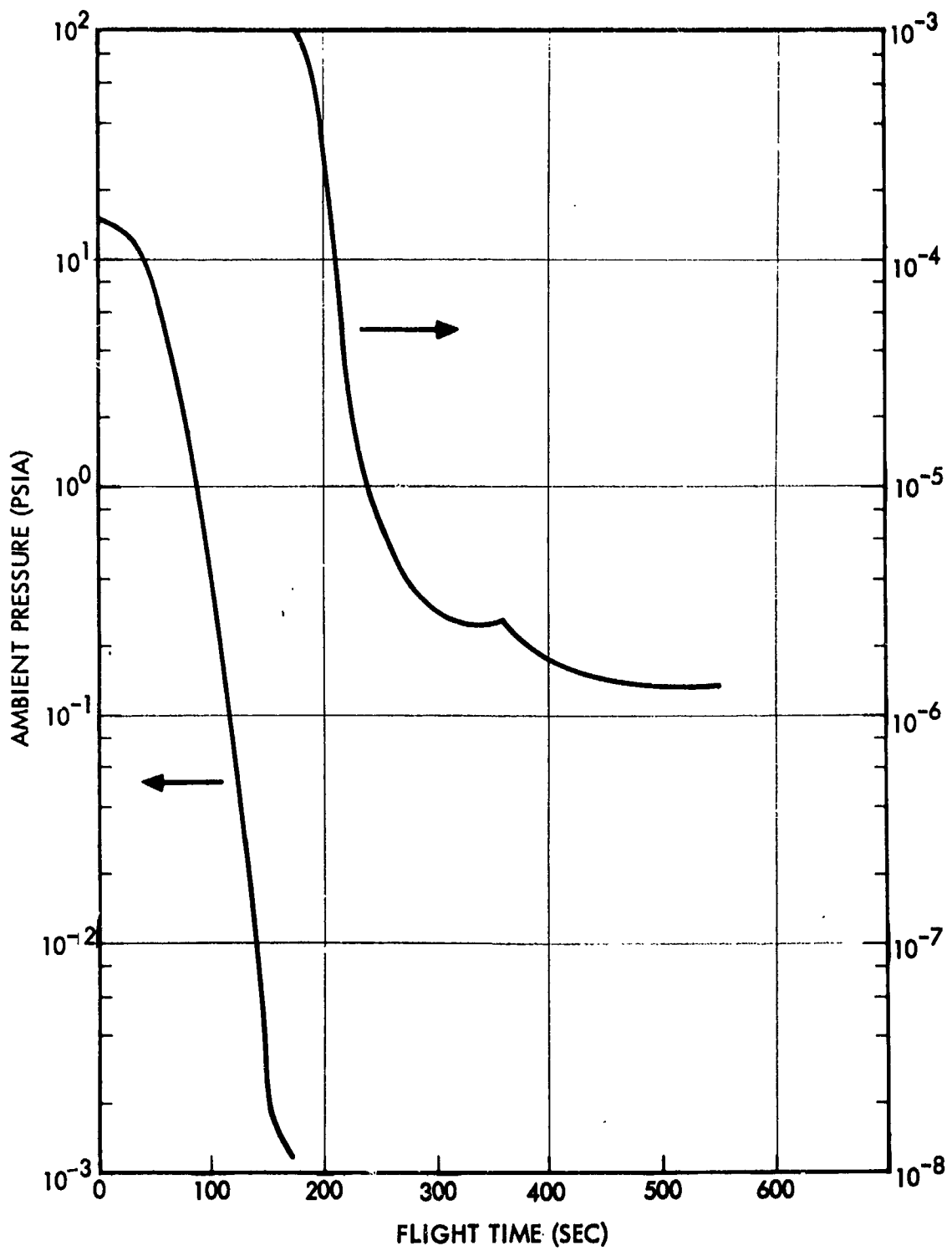


Fig. B-1 Saturn V Two-Stage-to-Orbit Ambient Pressure vs. Flight Time

B-2

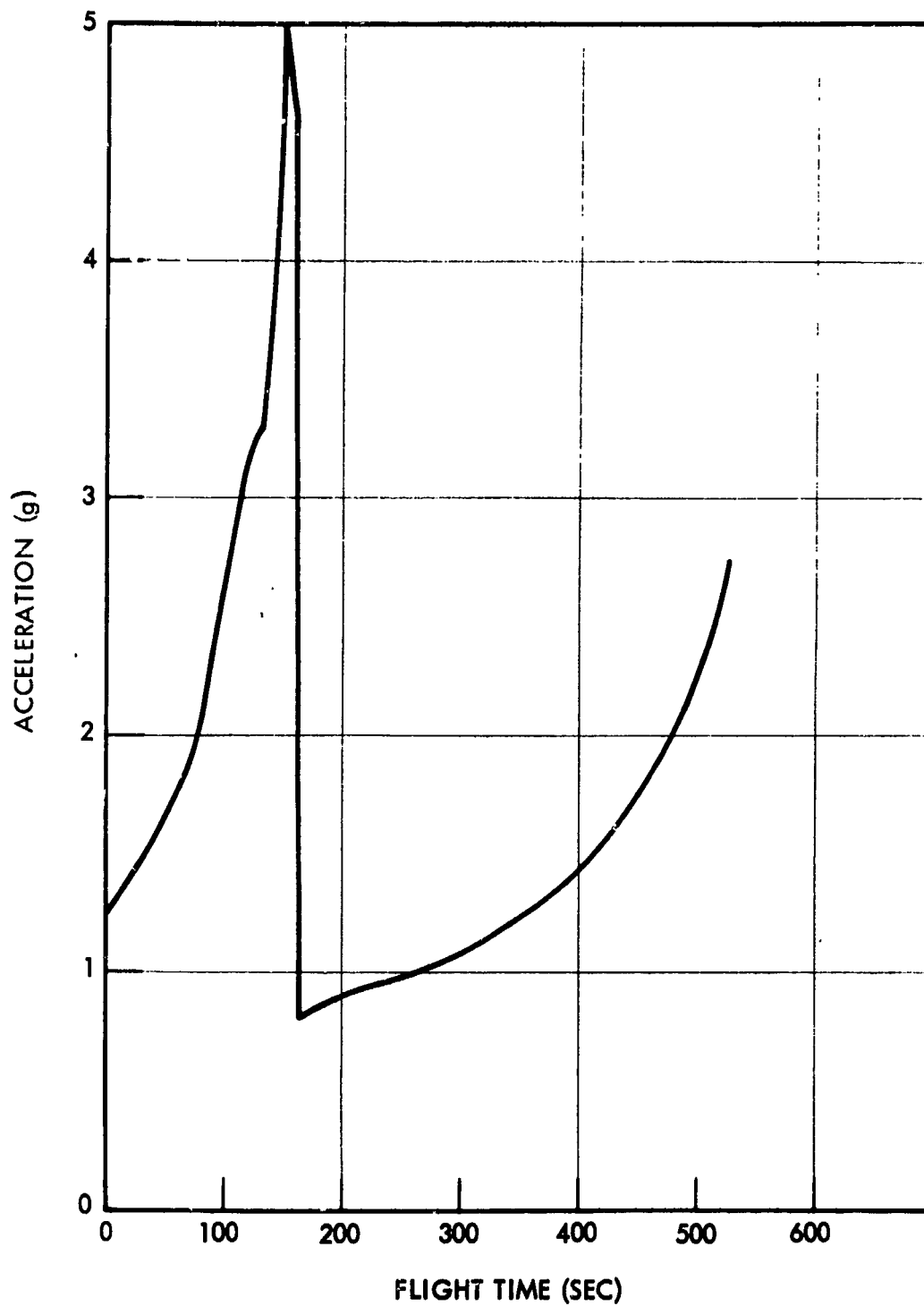


Fig. B-2 Saturn V Two-Stage-to-Orbit Acceleration vs. Flight Time

B-3

Table B-1

ACOUSTIC ENVIRONMENT FOR MODULAR NUCLEAR VEHICLE TANK  
BOTTOM - DOME INSULATION (PREDICTED VALUES FROM REF. B-2)

One-Third Octave Band Geometric Mean Frequency (Hz)	One-Third Octave Band Sound Pressure Levels* (db)
5.0	127.5
6.3	129.0
8.0	130.5
10.0	132.0
12.5	133.0
16.0	134.5
20.0	135.5
25.0	136.5
31.5	137.5
40.0	138.5
50.0	139.5
63.0	140.0
80.0	140.0
100.0	140.5
125.0	140.0
160.0	140.0
200.0	140.0
250.0	140.0
315.0	140.0
400.0	139.5
500.0	139.5
630.0	139.5
800.0	139.0
1,000.0	139.0
1,250.0	139.0
1,600.0	139.0
2,000.0	139.0
2,500.0	139.0
3,150.0	138.5
4,000.0	138.0
5,000.0	137.5
6,300.0	136.5
8,000.0	135.5
10,000.0	133.5
Overall Sound Pressure Level	153.0 db

\*Ref. 0.0002 dynes/cm<sup>2</sup>



Table B-2

**ACOUSTIC ENVIRONMENT FOR MODULAR NUCLEAR VEHICLE TANK  
CYLINDRICAL INSULATED SECTION (PREDICTED VALUES FROM REF. B-3)**

One-Third Octave Band Geometric Mean Frequency (Hz)	One-Third Octave Band Sound Pressure Levels* (db)
5.0	126.5
6.3	128.0
8.0	129.5
10.0	131.0
12.5	132.0
16.0	133.5
20.0	134.5
25.0	135.5
31.5	136.5
40.0	137.5
50.0	138.0
63.0	138.5
80.0	139.0
100.0	139.0
125.0	139.0
160.0	139.0
200.0	139.0
250.0	139.0
315.0	139.0
400.0	139.0
500.0	139.0
630.0	138.5
800.0	138.5
1,000.0	138.5
1,250.0	138.5
1,600.0	138.5
2,000.0	138.5
2,500.0	138.5
3,150.0	138.5
4,000.0	138.0
5,000.0	137.5
6,300.0	136.5
8,000.0	135.0
10,000.0	134.0
Overall Sound Pressure Level	152.0 db

\*Ref. 0.0002 dynes/cm<sup>2</sup>

## VIBRATION ENVIRONMENT

This tank insulation material will be required to conform to basic MNV specifications and be capable of withstanding the maximum vibrational environment generated during the Saturn V liftoff and ascent phases of flight. The insulation for the tank bottom and cylindrical sections will be exposed to the following conditions:

- (1) Sinusoidal Sweep
  - 10 - 14 Hz, 0.4-in. peak-to-peak amplitude
  - 14 - 300 Hz, 4.0-g zero-to-peak acceleration
  - 300 - 470 Hz, 0.0008-in. peak-to-peak amplitude
  - 470 - 2000 Hz, 10.0-g, zero-to-peak acceleration
- (2) Sinusoidal Dwell
  - 10 - 14 Hz, 0.2-g peak-to-peak amplitude
  - 14 - 300 Hz, 2.0-g zero-to-peak acceleration
  - 300 - 470 Hz, 0.0004-in. peak-to-peak amplitude
  - 470 - 2000 Hz, 5.0-g zero-to-peak acceleration
- (3) Random Vibration

Frequency (Hz)	Spectral Density (g <sup>2</sup> /Hz)
20	0.15
2000	0.15

(17.2-g rms)
- (4) Shock

Peak Acceleration	30 g
Pulse Duration*	10 ms
Pulse Shape	Sawtooth

## TEMPERATURE ENVIRONMENT

### Ascent

Temperature effects during ascent consist primarily of possible temperature degradation of system components during the short duration of aerodynamic heating.

---

\*For the sawtooth pulse, the rise time is equal to the pulse duration and the decay time should be less than 1 ms.

Previous studies (Ref. B-5) indicate that maximum temperatures of the shroud outer skin occur between 2 and 3 min after launch. It was shown that an outer shroud consisting of 0.1-in. aluminum sheet reached 220° F. The current design of the outer shroud, consisting of 6.3-in. of aluminum honeycomb with two cover sheets of 0.04-in. beryllium, has a density-times-specific ( $\rho c_p$ ) factor more than three times that of an 0.1-in. aluminum shroud. Therefore, the honeycomb-sandwich shroud should reach a lower ultimate ascent temperature than the calculated 220° F of the aluminum shroud. It was assumed that this is the maximum temperature to which the insulation is exposed.

#### Earth Orbit, Mars Transfer, Mars Orbit

Average outer-surface temperatures employed in this study were obtained from Ref. B-4 and are for a white painted surface ( $\alpha = 0.19$ ,  $\epsilon = 0.85$ ) and for an optical solar reflector (OSR) surface ( $\alpha = 0.05$ ,  $\epsilon = 0.8$ ). The temperatures are as follows:

	<u>Average Surface Temperature (° R)</u>		
	<u>Earth Orbit</u>	<u>Mars Transfer</u>	<u>Mars Orbit</u>
White Paint	400	220	350
OSR	—	185	—

For Mars transfer, a value of 220° R was taken as an average.

An indication of the external temperature variation around the meteoroid shield circumference during Mars transfer can be obtained from Fig. B-3. Similar curves for Earth orbit would indicate a maximum of less than 460° F.

#### TANK-BOTTOM-INSULATION RADIATION ENVIRONMENT

The neutron and gamma environment for the MNV tank bottom was derived from previous work accomplished for the 5000 Mw NERVA (Ref B-6). Using the current NERVA 1 engine rated at 1575 Mw and the appropriate scaling factor, the incident neutron and gamma energy was determined for the tank bottom. This is the highest exposure level expected in the MNV.

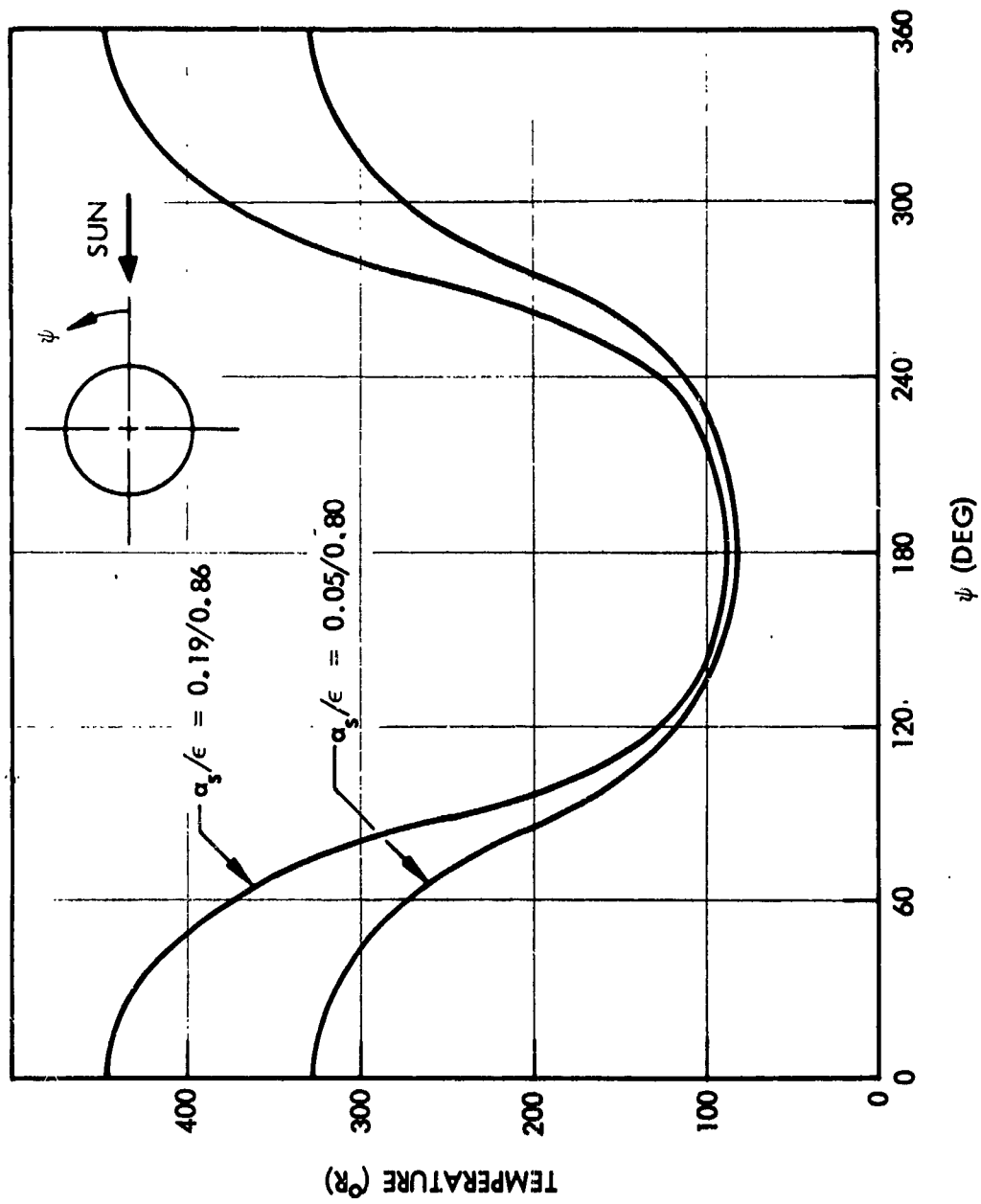


Fig. B-3 Meteoroid Shield External Variation During Mars Transfer

Neutron numbers and energy currents incident to the tank bottom at the insulation/tank-skin interface are listed in Table B-3 for various radii measured from the tank centerline. Incident neutron energy obtained from the product of energy current and corresponding subsurface area is listed in the last column. The table shows kinetic power carried by neutrons above 0.1 Mev entering the tank insulation is 31 kw (29 Btu/sec).

The incident gamma-ray energy current into the tank bottom insulation is presented in Table B-4. The data include primary fission gamma, reactor component secondary gamma, and the integrated total gamma over the radial band area. The total incident gamma energy entering the bottom insulation is 90 kw (85 Btu/sec).

Maximum radiation levels in the region of the tank bottom insulation are estimated at  $7.4 \times 10^{11}$  n/cm<sup>2</sup> sec for neutrons above 0.1 Mev and  $5.8 \times 10^6$  rad/hr for gamma rays, for an equivalent gamma of  $1.5 \times 10^7$  rad/hr.

Total power entering the tank bottom is computed to be 121 kw, 90 kw from gamma radiation and 31 kw from neutron radiation.

#### REFERENCES

- B-1 Lockheed Missiles & Space Company, Investigations Regarding Development of a High Performance Insulation System, Sunnyvale, Calif., 25 May 1967
- B-2 Marshall Space Flight Center, Saturn V Launch Vehicle Design Data (U), (Reissue) IN-P & VE-62-6, Huntsville, Ala., 15 Jul 1964 (C)
- B-3 Lockheed Missiles & Space Company, RIFT Environmental Specification, NSP-6520002A, Sunnyvale, Calif., 31 Jan 1964
- B-4 -----, Modular Nuclear Vehicle Study, Phase II, Vol III, LMSC-A830246, Sunnyvale, Calif., Mar 1967
- B-5 -----, Modular Nuclear Vehicle Design, Vol II, NAS 8-20007, LMSC-A794909, Sunnyvale, Calif., 3 Mar 1966
- B-6 -----, Modular Nuclear Vehicle Study, Phase II, Vol XI, LMSC-A848446, Sunnyvale, Calif., 16 Oct 1967

**Table B-3**  
**NEUTRON NUMBER AND ENERGY CURRENTS**  
**INTO TANK BOTTOM INSULATION**

Radial Band Limits (cm)	Neutron Number Current ( $n \text{ cm}^{-2} \text{ sec}^{-1}$ )	Neutron Energy Current ( $\text{Mev cm}^{-2} \text{ sec}^{-1}$ )	Neutron Power ( $\text{Mev sec}^{-1}$ )
0-50	6.33 (10)	8.64 (10)	6.78 (14)
50-248	2.51 (11)	3.72 (11)	7.18 (16)
248-342	2.84 (11)	4.16 (11)	8.29 (16)
342-407	1.06 (11)	1.56 (11)	3.15 (16)
407-450	2.18 (10)	3.42 (10)	6.58 (15)
450-479	3.23 (8)	4.10 (8)	8.89 (13)
479-487.67	5.85 (6)	2.67 (9)	5.12 (12)

Note: Total incident neutron power -  $1.94 (17) \text{ Mev sec}^{-1} = 31 \text{ kw} = 29 \text{ Btu sec}^{-1}$

**Table B-4**  
**GAMMA RAY ENERGY CURRENT INTO**  
**TANK BOTTOM INSULATION**

Radial Band Limits (cm)	Primary Gamma Energy Current ( $\text{Mev cm}^{-2} \text{ sec}^{-1}$ )	Secondary Gamma Energy Current ( $\text{Mev cm}^{-2} \text{ sec}^{-1}$ )	Total Gamma Power ( $\text{Mev sec}^{-1}$ )
0-50	2.58 (11)	4.09 (11)	5.29 (15)
50-250	7.61 (11)	4.77 (11)	2.42 (17)
250-342	5.92 (11)	3.39 (11)	1.89 (17)
342-410	2.75 (11)	1.42 (11)	8.62 (16)
410-454	1.34 (11)	3.65 (10)	3.39 (16)
454-492	0	0	0

Note: Total incident gamma power =  $5.58 (17) \text{ Mev sec}^{-1} = 80 \text{ kw} = 85 \text{ Btu sec}^{-1}$

N70-20004

## Appendix C

### DERIVATION OF ONE-DIMENSIONAL HEAT TRANSFER RELATION IN MULTILAYER COMPOSITES

This appendix describes the derivation of the engineering relation used to determine one-dimensional heat transfer via conduction and radiation through multilayer insulation composites. The relation was applied in Task 1 to extend measured effective thermal conductivity data obtained at 540°/140°R insulation boundary temperatures for each composite tested to temperatures of 400°/40°R, 350°/40°R, and 220°/40°R for a range of layer densities. These results were then applied in the effective weight parameter and in the sensitivity to compression parameter used for comparing relative performance of candidate composites (see Tables 1-13 and 1-14).

#### NOMENCLATURE

$\text{\AA}$	angstrom unit
A	area, $\text{ft}^2$
a	adsorption coefficient, $\text{ft}^{-1}$
C	constant, dimensionless
$C_v$	heat capacity at constant volume, $\text{Btu/lb-}^\circ\text{R}$
c	$\sqrt{3\lambda}\tau$ , radiation parameter, dimensionless
D	diameter, ft
E	modulus of elasticity, psi
F	radiant heat flux, $\text{Btu/hr-ft}^2$
h	conductance, $\text{Btu/hr-ft}^2\text{-}^\circ\text{R}$
$\Delta h$	latent heat of vaporization, $\text{Btu/lb}$
I	radiant intensity, $\text{Btu/hr-steradian}$
k	thermal conductivity, $\text{Btu/hr-ft-}^\circ\text{R}$
L	characteristic dimension of an enclosed volume with respect to gas flow, ft

$\ell$	length, ft
$m, n, p$	exponent, dimensionless
$\bar{n}$	defined by Eq. (C.9), dimensionless
$N$	number of radiation shields, dimensionless
$\bar{N}$	number of radiation shields per inch of insulation thickness, $\text{in.}^{-1}$
$o$	surface geometry parameter, dimensionless
$P$	pressure, psia
$q$	heat flux, $\text{Btu/hr-ft}^2$
$Q$	power or heat rate, Btu/hr
$s$	scattering cross section, $\text{ft}^{-1}$
$R$	resistance, $\text{Hr-}^\circ\text{R/Btu}$
$r$	radius, ft
$t$	thickness of insulation, ft
$T$	absolute temperature, $^\circ\text{R}$
$u$	velocity, ft/sec
$V$	voltage, volts
$\dot{v}$	volumetric flow rate, $\text{ft}^3/\text{sec}$
$x$	distance measured parallel to the X axis, ft
$\alpha$	accommodation coefficient, dimensionless
$\beta$	extinction coefficient, $\text{ft}^{-1}$
$\epsilon$	total hemispherical emittance, dimensionless
$\lambda$	mean free path, ft, or wavelength, micro-meter
$\lambda'$	ratio of absorption to extinction coefficient, dimensionless
$\mu$	Poisson's ratio, dimensionless, micro-meter
$\rho$	density, $\text{lb/ft}^3$
$\sigma$	Stefan-Boltzmann constant, $1.713 \times 10^{-9} \text{ Btu/ft}^2\text{-hr-}^\circ\text{R}^4$



$\tau$	optical thickness, dimensionless
$\eta$	defined by Eq. (C. 2), dimensionless
Subscripts	
c	refers to cold boundary of insulation
e	refers to effective value
g	refers to a gas phase
S	refers to spacer
m	refers to mean condition
h	refers to hot boundary of insulation

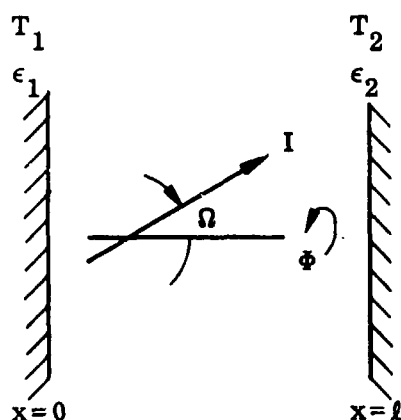
## SIMULTANEOUS RADIATION AND CONDUCTION

In evacuated multilayer insulations, heat transfer occurs simultaneously by conduction and radiation between the reflective layers. For many systems the total transport is a function of the interactions between these two mechanisms, and the strength of their interactions is dependent on the radiative properties of the surfaces and the separating media as well as the relative magnitudes of the solid and radiative fluxes. For the analysis, solid-to-solid conduction, as well as conduction through any residual gas, will be considered as one process. This is based on the assumption that although the transport processes in each medium may not be the same, the flux for both may be expressed by the product of a temperature gradient and a conductivity. Thermal energy leaving one surface passes through a conductive phase, as well as by radiation through the intervening space. The latter may be transmitted directly through void and solid phases, may be scattered by dispersed solid phases, and may be absorbed and re-emitted by the solid phase.

A number of investigators (Refs. C-1 through C-4) have studied the simultaneous radiation and conduction problem, and their results form the basis for the present analysis. The steady-state conservation of energy equation for the one-dimensional case is given by Eq. (C. 1).

$$-k \frac{d^2 T}{dx^2} + \frac{d(F)}{dx} = 0 \quad (C.1)$$

Wang and Tien (Refs. C-3 and C-4) have developed heat-flux equations that are applicable to the multilayer insulations studied in this program. The model of the problem is depicted in the sketch below.



The rate of change of the radiant flux with distance through the layer is related through the intensity  $I$  and the temperature of the layer. The orientation of the ray is described by angles  $\Omega$  and  $\Phi$ .

The physical system is characterized by three dimensionless parameters defined by Eq. (C.2).

$$\eta = \frac{k\beta}{4\sigma T_1^3} \quad , \quad \tau = \beta l \quad , \quad \lambda' = \frac{a}{\beta} \quad (C.2)$$

The parameter  $\eta$  relates the magnitude of conductive to radiative energy transport; for  $\eta \gg 1$ , conduction is predominant, whereas, for  $\eta \ll 1$ , radiation dominates. Optical thickness of the media is represented by  $\tau$ , and  $\lambda'$  relates the absorption to the extinction properties of the material. For scattering and absorbing media, the extinction coefficient includes both scattering and absorption coefficients. If  $\lambda \ll 1$ , scattering dominates.

Consider a system of parallel boundaries of emittance  $\epsilon$ . For the strongly interacting radiation-dominant case,  $\eta \ll 1$  and  $(\eta/\lambda'\tau^2) \ll 1$ , Wang and Tien show that

$$q = \frac{\frac{3}{4} k_3 (T_1 - T_2) + \sigma (T_1^4 - T_2^4)}{\frac{3}{4} \tau + \frac{\frac{3}{8} + \frac{1}{3} (1 - \epsilon)}{\eta + \frac{2}{3} \epsilon} + \frac{\frac{3}{8} + \frac{1}{3} (1 - \epsilon)}{\frac{\eta}{\left(\frac{T_2}{T_1}\right)^3 + \frac{2}{3} \epsilon}} \quad (C. 3)$$

Similarly, for an optically thin or conduction-dominant case,  $\eta \gg 1$  or  $(\eta/\lambda'\tau^2) \gg 1$ , the solution for heat flux is given by

$$q = \frac{k}{\ell} (T_1 - T_2) + \frac{\sigma (T_1^4 - T_2^4)}{\frac{3}{4} \tau} \left[ \frac{\frac{3}{4} \tau \left( \frac{\epsilon}{2 - \epsilon} \right) + \frac{1}{2} \frac{\sqrt{3\lambda'} \tau}{\tanh \sqrt{3\lambda'} \tau} + \frac{1}{2} \frac{\sqrt{3\lambda'} \tau}{\sinh \sqrt{3\lambda'} \tau} - 1 \right] \quad (C. 4)$$

If the spacer media has a very small absorption coefficient  $\sqrt{3\lambda'} \tau \ll 1$ , and Eq. (C. 4) becomes

$$q = \frac{k}{\ell} (T_1 - T_2) + \frac{\sigma (T_1^4 - T_2^4)}{\frac{3}{4} \tau + \left( \frac{2}{\epsilon} - 1 \right)} \quad (C. 5)$$

Equation (C. 5) shows that for this case interaction is negligible, and total heat flux may be considered simply as the sum of the individual fluxes. For shields not having a spacer layer but that are separated by crinkling or dimpling of the radiation shield, as well as those separated by a nonradiative layer such as an open netting, the extinction coefficient is zero and  $\tau = 0$ ; the equation for the heat transfer across such a system is

$$q = \frac{k}{\ell} (T_1 - T_2) + \frac{\sigma(T_1^4 - T_2^4)}{\left(\frac{2}{\epsilon} - 1\right)} \quad (C.6)$$

and for a system of  $N$  reflective shields between boundaries  $T_h$  and  $T_c$

$$q = \frac{k}{\ell} (T_h - T_c) + \frac{\sigma(T_h^4 - T_c^4)}{(N - 1)\left(\frac{2}{\epsilon} - 1\right)} \quad (C.7)$$

Next, consider the case of a spacer layer for which  $\tau \neq 0$ . Fibrous spacers, while having finite absorption and extinction coefficients, are generally of small thickness so that  $\lambda'\tau^2 < 1$ , and for the optimum layer density for minimum effective thermal conductivity,  $\eta \geq 1$ , resulting in  $(\eta/\lambda'\tau^2) > 1$ . For these materials,  $\sqrt{3\lambda'}\tau < 1$  and typical values are  $1.0 > \sqrt{3\lambda'}\tau > 0.1$  (Ref. C-5). For  $N$  reflective shields, the equation for heat transfer from Eq. (C.4) and for  $\sqrt{3\lambda'}\tau = c$  is

$$q = \frac{k}{\ell} (T_h - T_c) + \frac{\sigma(T_h^4 - T_c^4)}{(N - 1)\frac{3}{4}\tau} \left[ \frac{\frac{3}{4}\tau\left(\frac{\epsilon}{2 - \epsilon}\right) + \frac{1}{2}\frac{c}{\tanh c} + \frac{1}{2}\frac{c}{\sinh c} - 1}{\frac{3}{4}\tau\left(\frac{\epsilon}{2 - \epsilon}\right) + \frac{1}{2}\frac{c}{\tanh c} + \frac{1}{2}\frac{c}{\sinh c}} \right] \quad (C.8)$$

The effect of the interaction is no longer negligible and the total flux is increased over that of the case of  $c \ll 1$ . This increase may be expressed as some factor  $\bar{n}$  times the noninteracting condition. The numerical value of  $\bar{n}$  is calculated from

$$\bar{n} = \frac{\left(\frac{2}{\epsilon} - 1\right)}{\frac{3}{4}\tau} \left[ \frac{\frac{3}{4}\tau\left(\frac{\epsilon}{2 - \epsilon}\right) + \frac{1}{2}\frac{c}{\tanh c} + \frac{1}{2}\frac{c}{\sinh c} - 1}{\frac{3}{4}\tau\left(\frac{\epsilon}{2 - \epsilon}\right) + \frac{1}{2}\frac{c}{\tanh c} + \frac{1}{2}\frac{c}{\sinh c}} \right] \quad (C.9)$$

Typical values of  $\bar{n}$  are 1.7 for Tissuglas and 2.7 for Dexiglas.

Heat transfer for highly efficient multilayer insulations should be accurately predicted by the method of superimposing the conductive and radiative fluxes. Considering only radiation transport, this heat flux is increased by the use of a finite thickness of an adsorbing spacer material. This is illustrated by the values of  $\bar{n}$  for Tissuglas and Dexiglas. Both materials have essentially the same adsorption and scattering coefficients. However, the thickness of Tissuglas is  $6 \times 10^{-4}$  in., as compared to  $3 \times 10^{-3}$  in. for Dexiglas; thus,  $\tau$  of the former is approximately 1/5 of that of the latter. This is reflected in the values of  $\bar{n}$  for these two materials. A second consideration is the increase in reflective shield total hemispherical emittance for the metal dielectric interface case over that into air or vacuum. Caren (Ref. C-6) has reported the increase in emittance to be approximately 1.3 to 1.4 for glass fiber media.

#### GASEOUS CONDUCTION

Although thermal conductivity of the residual gas in a multilayer insulation in vacuum is very small, it should be examined to evaluate its effect on thermal conductivity of advanced, high-performance insulations for space applications. From kinetic theory, the thermal conductivity of a gas is given by

$$k = C_p C_v u \lambda \quad (C.10)$$

Conductivity at constant temperature is then proportional to the density of the gas and its molecular mean free path. As the mean free path is inversely proportional to the number of molecules per unit volume and the density is directly proportional to the number of molecules, the conductivity of a free gas is essentially constant over a wide range of pressures at low densities. However, for the case of a restricted or contained gas, as occurs in the interstices of a multilayer insulation, the mean free path of the gas becomes larger than the characteristic dimensions of the void space as pressure is reduced. Thermal conductivity of the unrestricted gas is then directly proportional to pressure as density decreases with decreasing pressure, but the effective path length is constant.

Considering both molecule-molecule and molecule-surface collisions, Verschoor (Ref. C-7) derived an effective mean free path for the restricted gas, which is given by

$$\lambda^* = \lambda \left( \frac{L_S}{L_S + \lambda} \right) \quad (C. 11)$$

The pressure-dependent thermal conductivity of a gas contained within the insulation voids is

$$k_g = \alpha C \rho C_v u \lambda \left( \frac{L_S}{L_S + \lambda} \right) \quad (C. 12)$$

or

$$k_g = \alpha k_g^* \left( \frac{L_S}{L_S + \lambda} \right) \quad (C. 13)$$

Where  $k_g^*$  is the thermal conductivity of the free gas at a specified temperature. The accommodation coefficient  $\alpha$  represents the ratio of actual-to-equilibrium energy transfer, and it may vary between zero and unity, depending upon gas specie and surface conditions.

Variation of mean free path with temperature and pressure are of the form  $P_0/P$  and  $(T/T_0)^{n+(1/2)}$ , where the subscript denotes reference conditions and the exponent  $n$  is dependent on the Lennard-Jones parameter and the collision function. Values of the mean free path as a function of pressure for two temperatures are given in Fig. C-1 for air and helium. At a pressure of  $10^{-5}$  torr, or less, and for the void dimensions typically found in multilayer insulations ( $5 \times 10^{-4}$  to  $3 \times 10^{-2}$  in.), the gas conductivity is less than  $10^{-5}$  Btu/hr-ft-°R. Thermal conductivity as a function of pressure is shown in Fig. C-2 for air and helium at 200° and 500° R for three characteristic void

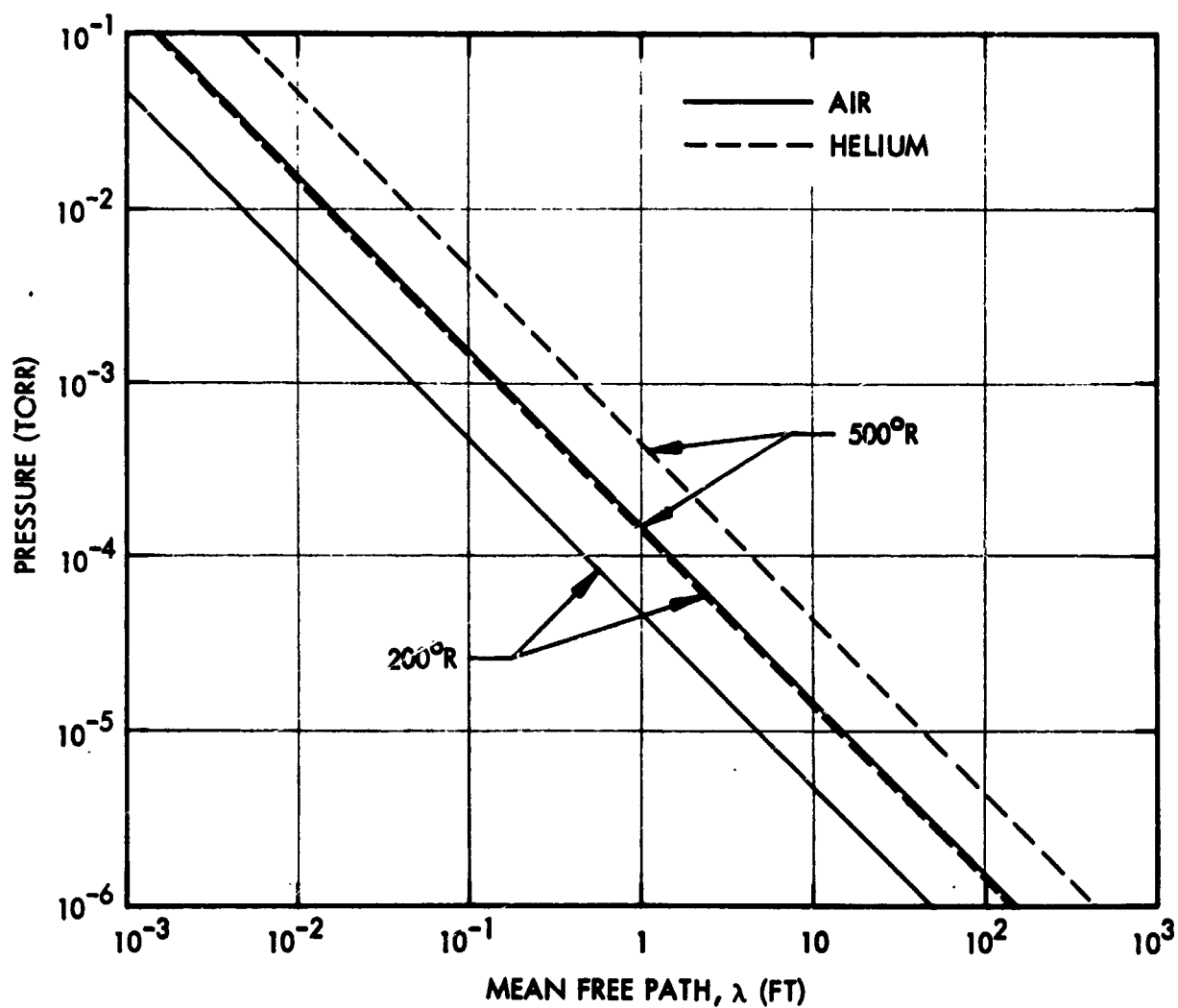


Fig. C-1 Variation of Mean Free Path for Air and Helium With Pressure for Temperatures of 200° and 500°R

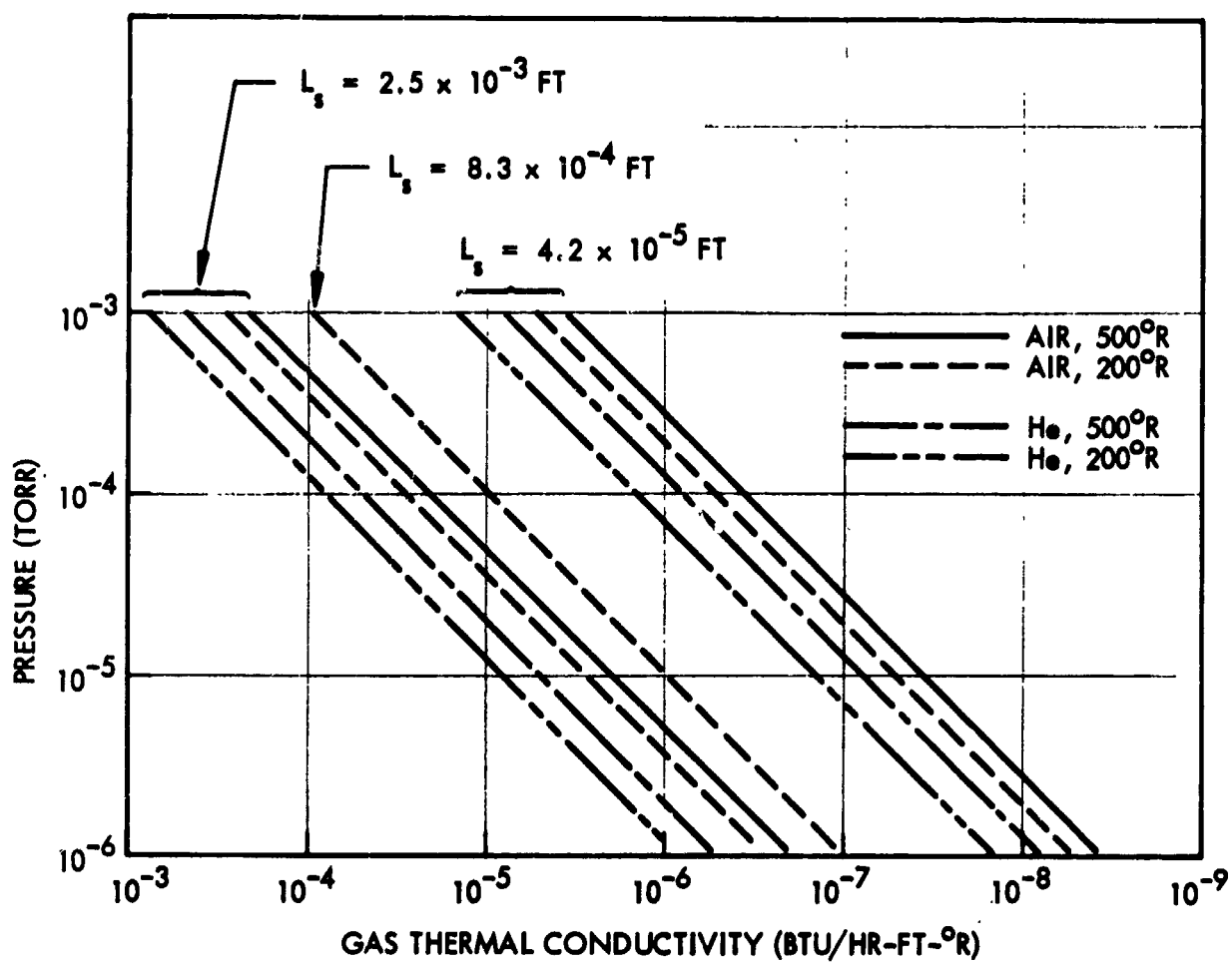


Fig. C-2 Thermal Conductivity of Air and Helium as a Function of Pressure for Several Characteristic Void Dimensions and Temperatures



or cell dimensions that are typical of those found in multilayer insulation systems. The dimensions of  $8.3 \times 10^{-4}$  and  $2.5 \times 10^{-3}$  ft correspond to lengths occurring in systems having integral spacers (NRC-2, Superfloc, etc.) or the cells in foams. The smallest dimension corresponds to a micron-size fiber spacer. Thermal conductivity of a gas in a multilayer insulation increases slightly with decreasing temperature, as shown in Fig. C-3. This is due to a greater change in mean free path than in conductivity as a function of temperature. At pressures above  $10^{-5}$  torr, residual gas conductivity should be considered in high-performance systems having relatively large void dimensions. However, for the systems and gas pressures under consideration in this study, gas conductivity is negligible compared with radiation and solid conduction.

#### SOLID-PHASE CONDUCTION

For the general case of the multilayer system, the overall solid conduction is a function of the contact area per interface, the number of interfaces, the thermal conductivity of the spacer layers, and the thermal conductivity of the shield materials.

Treating these as thermal resistances in series, the overall solid phase conductivity  $k_s$  becomes

$$k_s = \frac{t}{AR_t} \quad (C. 14)$$

and

$$R_t = \sum_0^t (R_i + R_s + R_r) \quad (C. 15)$$

where  $R_i$ ,  $R_s$ , and  $R_r$  are the thermal resistances of the interfaces, spacer, and shields, respectively. For a system consisting of  $N$  radiation shields and  $N-1$  spacers, the total resistance is

$$R_t = 2(N - 1)R_i + (N - 1)R_s + NR_r \quad (C. 16)$$

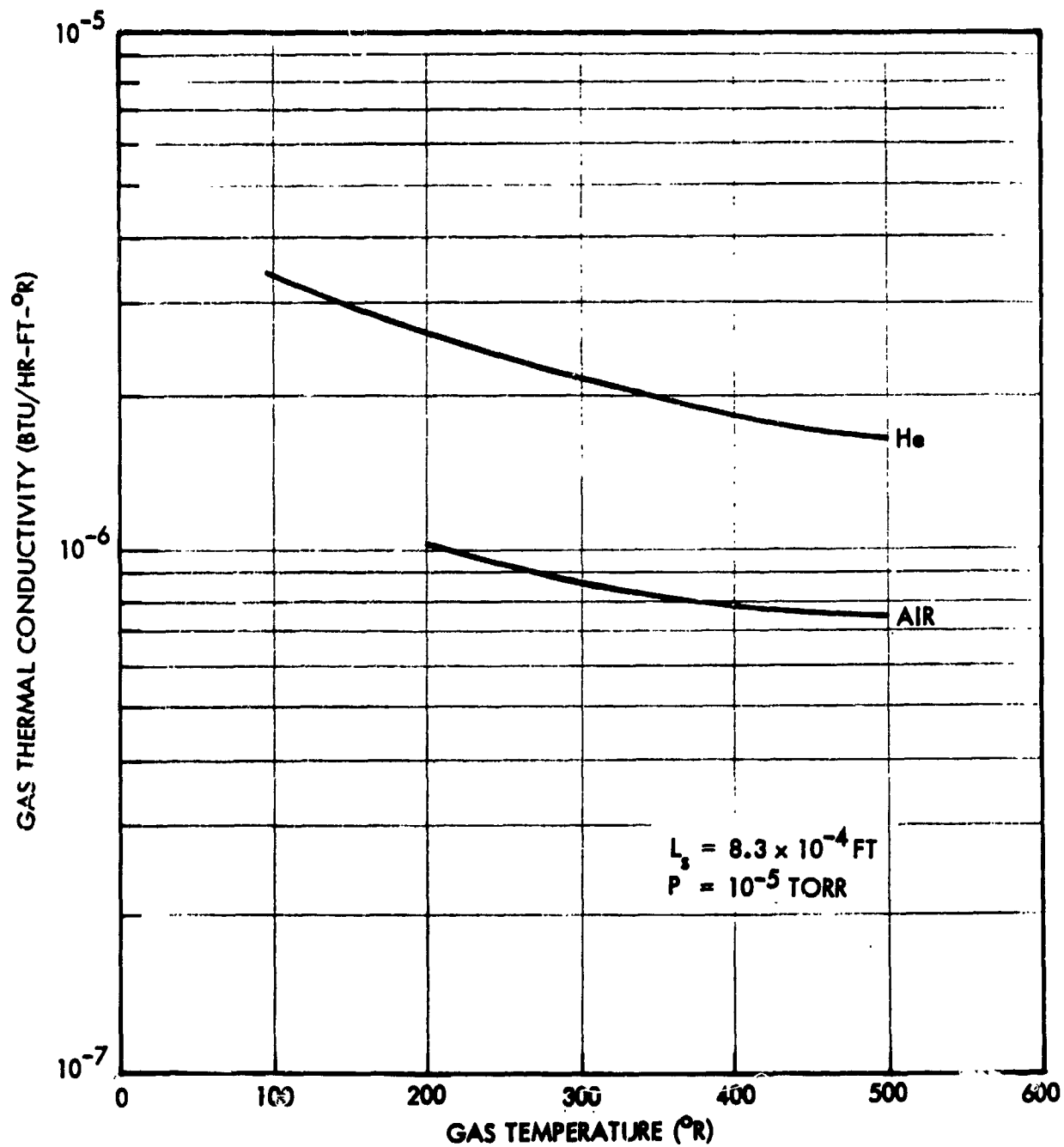


Fig. C-3 Variation of Thermal Conductivity With Temperature for a Restricted Gas at Low Pressure

For high performance multilayer insulations, the resistance of the radiation shield layer is several orders of magnitude less than that of either the interface or spacer and may be neglected.

Considering the spacer material to have a thermal conductivity  $k_s^*$  (which is at the bulk density of the particular spacer and is not the conductivity of the material from which it is fabricated), the resistance of a spacer layer is

$$R_s = \frac{t_s}{k_s^* A} \quad (C.17)$$

The resistance at each interface cannot be determined easily because of the complexity of the surfaces (which are generally not well characterized) and the non-uniformity of load or pressure distribution at the interface. However, identification of the principal physical parameters provides a method to semi-empirically analyze this mechanism. Consider this resistance to be that between two wavy, dissimilar surfaces, one of which also may be very rough. The conductance across the surfaces, their thermal conductivities, roughness and waviness characteristic dimensions, deformation of the materials under a load, and geometry of the contact area are the primary parameters. The conductance may be expressed as

$$h_c \propto [k] \left[ \frac{P, \mu}{E} \right]^m [r][o]^r \quad (C.18)$$

The  $[k]$  term considers the thermal characteristics and  $\left[ \frac{P, \mu}{E} \right]^m$  the deformation characteristics of the materials, whereas, the geometries of surfaces and asperities are related by  $[r]$  and  $[o]^n$ . Combining the surface, deformation, thermal, and geometric parameters and their exponents into a single coefficient, the conductance for a specific combination of shield and spacer materials is given as a function of a pressure or compressive load by

$$h_c = Cp^n \quad (C.19)$$

This form permits a comparison to be made of the conductance as a function of layer density for a given system because the pressure is related to the number of layers per unit thickness.

The thermal resistance at each interface is

$$R_i = \frac{1}{h_c A} \quad (C.20)$$

and the overall solid-phase conductivity, considering interface and spacer resistance, is

$$k_s = \frac{t}{(N - 1)} \left( \frac{1}{\frac{2}{h_c} + \frac{t_s}{k_s^*}} \right) \quad (C.21)$$

The term  $t/(N - 1)$  is the reciprocal of layer density,  $\bar{N}$ , and by substitution of Eq. (C.19), the solid-phase thermal conductivity becomes

$$k_s = \frac{1}{\bar{N}} \left[ \frac{1}{\frac{2}{CP^n} + \frac{t_s}{k_s^*}} \right] \quad (C.22)$$

For many of the high-performance cryogenic multilayer systems, the term  $t_s/k_s^*$  is small compared to the interface resistance term, and solid-phase thermal conductivity is then proportional to the pressure to some power and inversely proportional to the number of layers, as shown by

$$k_s \propto \frac{CP^n}{\bar{N}} \quad (C.23)$$

## EFFECTIVE THERMAL CONDUCTIVITY

The total heat flux through evacuated cryogenic multilayer insulations is accurately predicted by the method of superimposing the individual fluxes caused by conduction and radiation. The effect of spacer materials on radiation transfer must be considered, and the solution proposed includes such corrections when required. The conditions governing the application of the corrections are established by the dimensionless parameters relating to the optical character of a spacer material. The general equation used for the analysis of cryogenic multilayer insulation heat flux is

$$q = \frac{k_s (T_h - T_c)}{t} + \frac{\bar{n} \sigma (T_h^4 - T_c^4)}{(N - 1) \left( \frac{2}{\bar{\epsilon}} - 1 \right)} \quad (\text{C. 24})$$

where  $\bar{\epsilon}$  is the effective emittance of the reflective shield, (i. e., total hemispherical emittance corrected for metal-to-dielectric emission when applicable) and  $\bar{n}$  is given by Eq. (C. 9). The effective thermal conductivity of the insulation is

$$k_e = k_s + \frac{\bar{n} \sigma (T_h^2 + T_c^2) (T_h + T_c) t}{(N - 1) \left( \frac{2}{\bar{\epsilon}} - 1 \right)} \quad (\text{C. 25})$$

Considering that the mechanical and thermal properties are linear functions of temperature, the equation for effective thermal conductivity becomes

$$k_e = C' (N)^{\bar{n}} T_m + \frac{\bar{n} \sigma (T_h^2 + T_c^2) (T_h + T_c) t}{(N - 1) \left( \frac{2}{\bar{\epsilon}} - 1 \right)} \quad \text{or} \quad (\text{C. 26})$$

$$k_e = \frac{C(P)^{\bar{n}}}{\bar{N}} T_m + \frac{\bar{n} \sigma (T_h^2 + T_c^2) (T_h + T_c) t}{(N - 1) \left( \frac{2}{\bar{\epsilon}} - 1 \right)}$$

The terms defining the radiative properties of the shields and spacer materials ( $\bar{\epsilon}$  and  $\bar{n}$ , respectively) are based on experimentally determined shield total hemispherical emittance and spacer absorption and extinction coefficients for each type of insulation composite. Substitution of the appropriate values in Eq. (C.26) for each multilayer composite provides an equation that may be used to predict the insulation conductivity at any temperature, thereby extending the experimental data obtained from the flat plate calorimeter (at 540°/140° R).

Derivation of the constants in Eq. (C.26) for each multilayer composite is accomplished by first determining the  $k_{\text{rad}}$  term, which constitutes the right-hand portion of the equation. The factor  $\bar{n}$  is determined from Eq. (C.9) and is a function of experimentally determined values of optical thickness  $\tau$  and the shield total hemispherical emittance,  $\epsilon$ .

Emittance of pure metal surfaces is temperature dependent over the range of cryogenic insulation temperatures,  $\epsilon = \phi T$ . Substitution of this relationship in Eq. (C.26) results in an extremely complex equation. To evaluate this temperature effect, a computer program was developed to use the form  $\epsilon = a_0 + a_1 T$ . This solution was based on  $Q_{\text{total}} = Q_{\text{solid cond}} + Q_{\text{rad}}$ , where

$$Q_{\text{rad}} = \sum \frac{A\sigma (T_n^4 - T_{n-1}^4)}{\frac{1}{\epsilon_n} + \frac{1}{\epsilon_{n-1}} - 1} \quad \text{and} \quad Q_{\text{solid cond}} = \sum \frac{Ak_s (T_n - T_{n-1})}{\Delta x} \quad (\text{C.27})$$

These equations were used to determine temperature distributions through the multilayer composites. The solid curves of Fig. C-4 show the predicted temperature distribution through 10-, 50-, and 200-layer composites of double-aluminized Mylar with no solid conduction ( $k_s = 0$ ). The dashed curve of Fig. C-4 shows the predicted temperature distribution for 10 and 50 layers of double-aluminized Mylar with a finite solid conduction, namely,  $k_s = 1 \times 10^{-5}$  Btu/hr-ft-°R. Effective emissivities were approximated from these data. Without solid conduction ( $k_s = 0$ ),

$$\bar{\epsilon} \approx 1.3 \left( \frac{\epsilon_h + \epsilon_c}{2} \right) \quad (\text{C.28a})$$

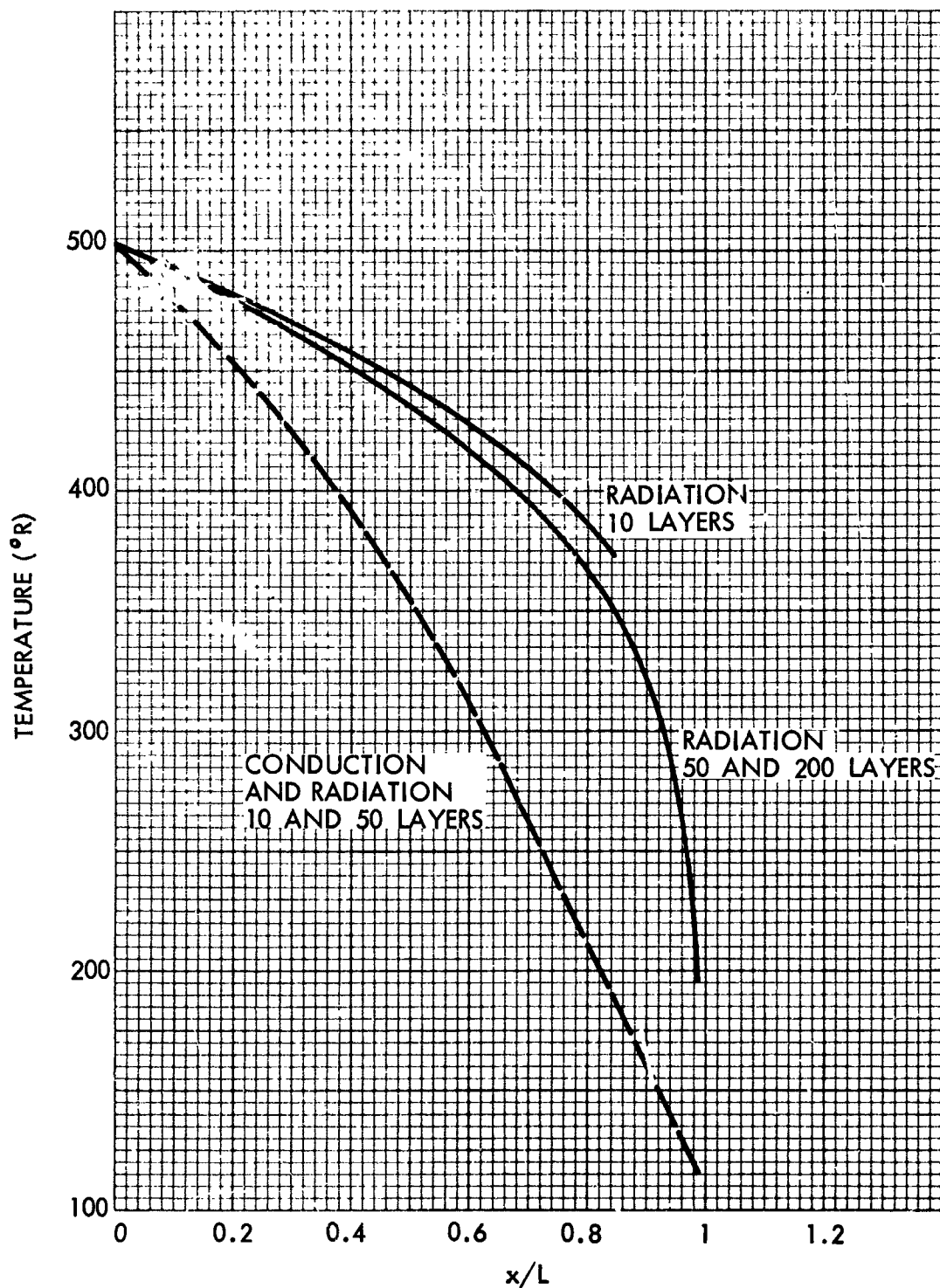


Fig. C-4 Prediction Temperature Distribution Through Multilayer Insulation

and, with solid conduction,

$$\bar{\epsilon} \approx 1.1 \left( \frac{\epsilon_h + \epsilon_c}{2} \right) \quad (C.28b)$$

For analysis of each composite investigated, it was not deemed necessary to attempt further refinement of the effective emittance relationship [ Eq. (C.28b)] to account for each value of solid conduction ( $k_s$ ). At optimum layer densities, the solid conductivity is reasonably approximated by  $1 \times 10^{-5}$  Btu/hr-ft-°R, and the use of Eq. (C.28b) is sufficiently accurate for characterizing the data. At higher layer densities,  $k_s$  becomes larger and  $\bar{\epsilon} \rightarrow \left( \frac{\epsilon_h + \epsilon_c}{2} \right)$ . These two equations may, however, explain the rapid increase in effective conductivity of multilayer composites as the layer density decreases below the optimum. At low layer densities, the solid conduction term is much smaller than the radiative term. For  $k_s \ll k_{rad}$ , the emittance correction factor increases from 1.1 to 1.3, which increases  $k_e$  by a corresponding amount.

When the layers are separated by a dielectric, such as Dexiglas or Tissuglas, a correction must be made in Eq. (C-28b). For these cases,

$$\bar{\epsilon} = (1.35) (1.1) \frac{\epsilon_h + \epsilon_c}{2} \quad (C.29)$$

Values for  $\tau$  and  $\lambda'$  are obtained from absorption and extinction coefficients, Eq. (C.2), which are used with  $\bar{\epsilon}$  to obtain  $\bar{n}$  in Eq. (C.9). This provides adequate data for determination of the radiation conductivity ( $k_r$ ) in Eq. (C.26).

Figure C-5 shows experimental values of effective thermal conductivity for NRC-2 plotted versus layer density. Also shown are values of radiation conductivity ( $k_r$ ) as calculated using the right-hand term in Eq. (C.26). Subtracting values of  $k_r$  from the experimental values of  $k_e$  produces values for the solid conductivity  $k_s$ . Again,



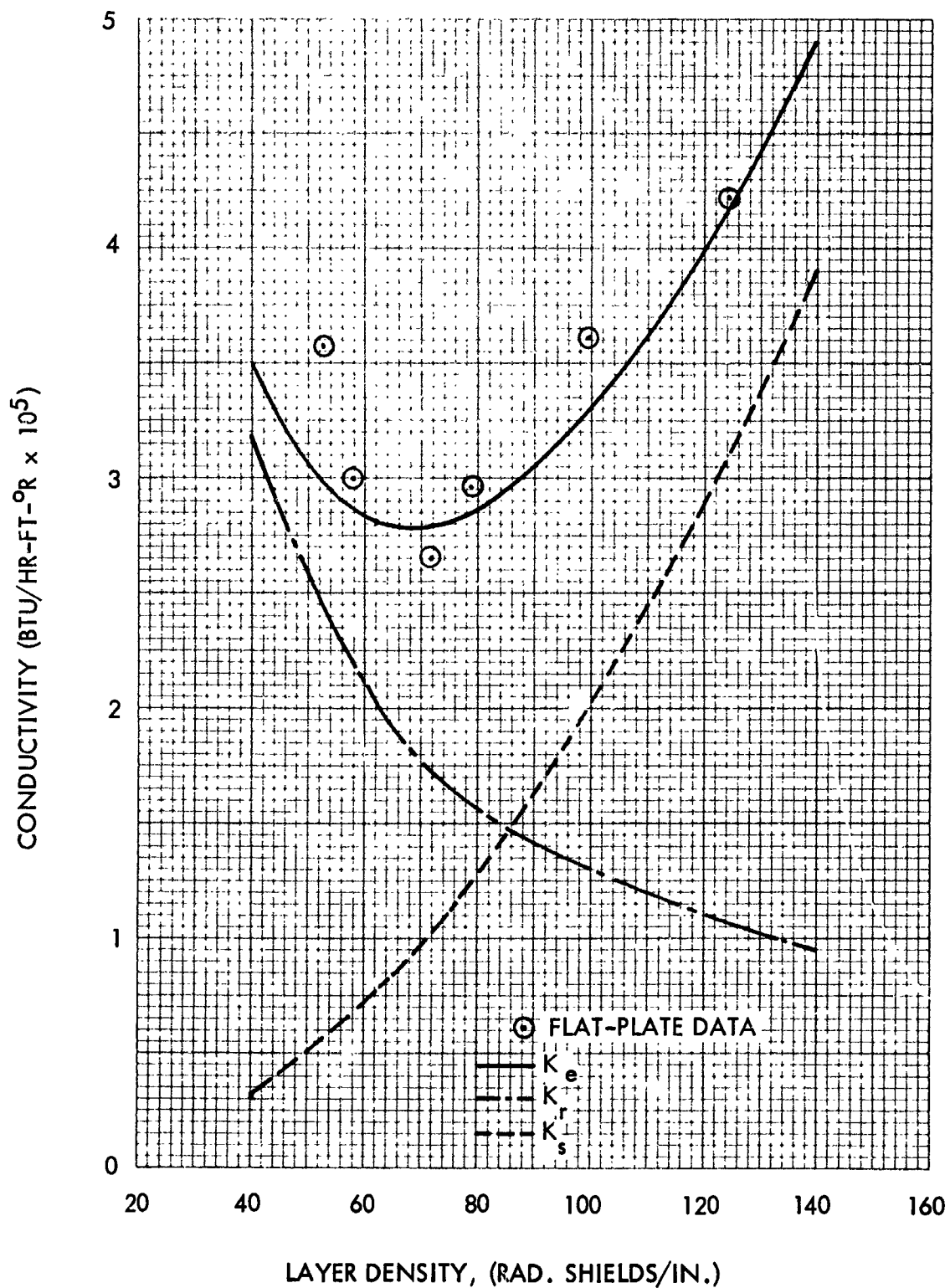


Fig. C-5 Effective Conductivity With Solid and Radiative Components – NRC-2

by use of Eq. (C.26) and curve-fitting techniques, both  $C'$  and  $n$  are established. In the case of NRC-2, the final equation is

$$k_e = 5.90 \times 10^{-12} (\bar{N})^2 T_m + \frac{\sigma(T_h^2 + T_c^2)(T_h + T_c)t}{(N-1)\left(\frac{1}{\epsilon_a} + \frac{1}{\epsilon_b} - 1\right)} \quad (C.30)$$

This equation was used to extend the 540°/140° R data obtained from the FPC to other boundary temperatures. The equation for each composite was derived in a similar manner.

#### REFERENCES

- C-1 R. Viskanta, "Heat Transfer by Conduction and Radiation in Absorbing and Scattering Materials," J. Heat Transfer, Vol. 87 C, 1965, p. 143
- C-2 W. Lick, Proceedings of the 1963 Heat Transfer and Fluid Mechanics Institute, Stanford Univ. Press, Stanford, Calif., 1963, p. 14
- C-3 L. S. Wang and C. L. Tien, Proceedings of the Third International Heat Transfer Conference, ASME, 1966, p. 190
- C-4 L. S. Wang and C. L. Tien, Int. J. Heat Mass Transfer, Vol. 10, Pergamum Press, Ltd., Great Britain, 1967, p. 1
- C-5 G. R. Cunningham et al., Performance of Multilayer Insulation System for Temperatures to 700 °K, NASA CR-907, 1967
- C-6 R. P. Caren "Radiation Transfer from a Metal to a Finely Divided Particular Medium" (to be published J. Heat Transfer)
- C-7 J. D. Verschoor and P. Greebler, Trans. ASME, Vol. 74, 1952, p. 961

N70-20305

## Appendix D FLAT PLATE CALORIMETER APPARATUS

A description of the Flat Plate Calorimeter (FPC), used in Task 1 for the measurement of effective thermal conductivity as a function of insulation layer density, is presented in this Appendix.

### DESCRIPTION

The major elements of the FPC are calorimeter and guard cryogen reservoirs, a hot-boundary heater plate, a vacuum chamber and pumping system, and means for remotely changing and measuring specimen thickness. A schematic of the FPC is shown in Fig. D-1. The apparatus is shown in Fig. D-2.

The calorimeter portion is a 6.25-in.-diameter by 8-in.-high vessel constructed of stainless steel with a 0.25-in.-thick copper plate that contacts the specimen. It is filled with copper wool to improve internal heat transfer and has concentric fill and vent tubes entering at the top. The guard reservoir is 16-in. OD and 6.5-in. ID, and surrounds the sides and top of the calorimeter vessel. The surfaces of both vessels which contact the insulation are painted with a flat black paint ( $\epsilon \approx 0.90$ ). Compressive forces on the calorimeter section are transmitted to the guard section through three spherical glass contacts. Adjustment means are provided to maintain the surfaces contacting the insulation within 0.002 in. in the same plane. The calorimeter section vent and fill lines are thermally grounded to the guard reservoir, and a radiation baffle is provided in the fill line.

Hot-boundary temperature is maintained by a copper heater plate 16 in. in diameter, and 0.25 in. thick. This heater is painted black on the surface that contacts the insulation. A stainless-steel-sheathed "Kanthai" heater winding is brazed to the under side of this plate, and the assembly is thermally insulated from the water-cooled support plate below the specimen with a loading bearing block-type insulating material.



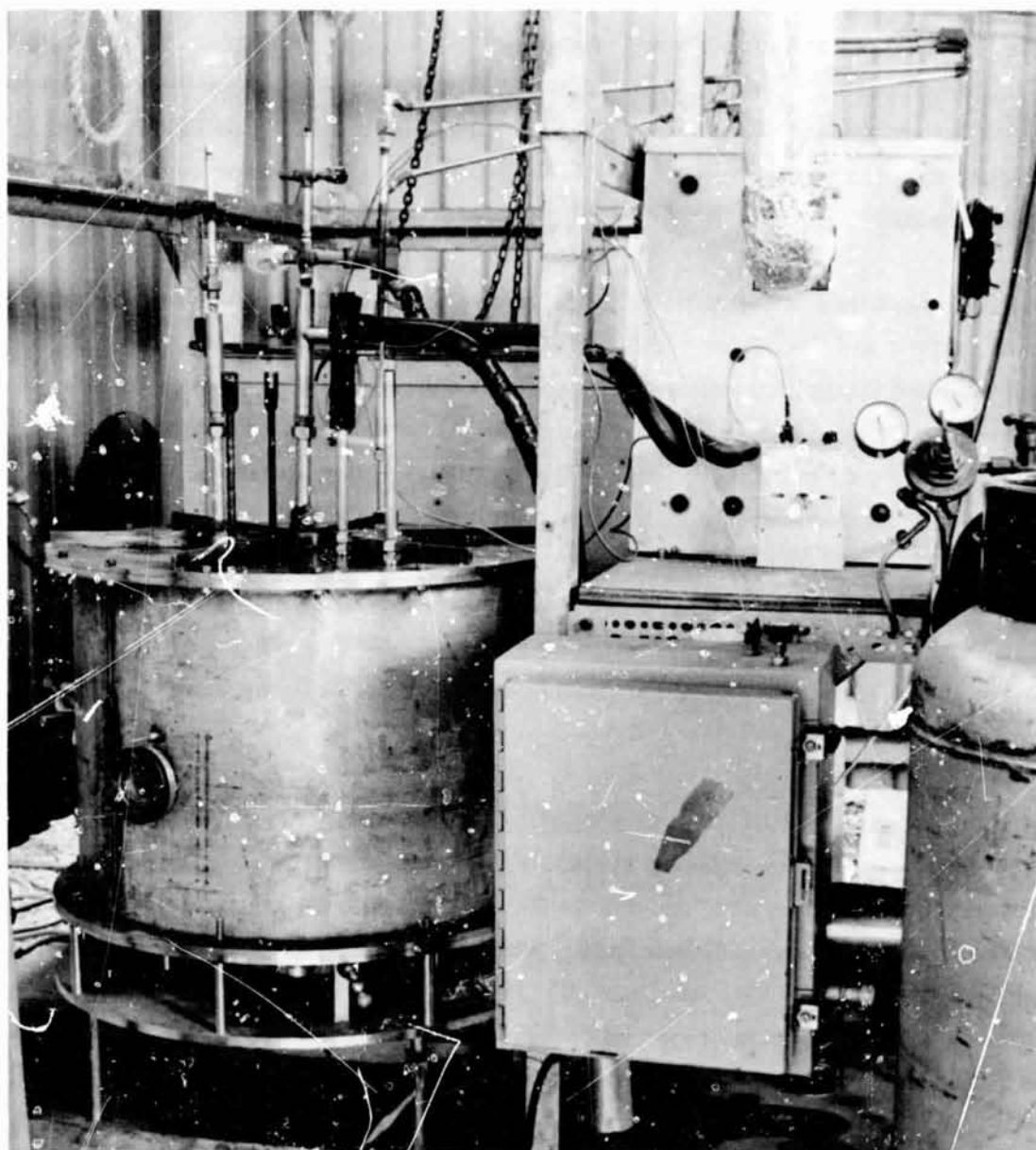


Fig. D-2 Flat-Plate Calorimeter

Five chromel-alumel thermocouples are peened into the plate, one for control and four for hot-boundary temperature measurement. Control of heater temperature to  $\pm 0.5^\circ\text{F}$  is achieved using a Leeds and Northrop CAT controller with null detector and set point units. Heater power is from a well regulated DC supply. An edge-guard unit is provided, which permits control of the radiative environment viewed by the circumferential edge of the specimen. This unit may be operated between  $540^\circ$  and  $145^\circ\text{R}$ . Five chromel-alumel thermocouples are attached to the ring for temperature control and measurement.

Specimen thickness is determined by the separation between the fixed calorimeter and guard surface and the heater plate surface, which is movable. This movement is accomplished through a hydraulic ram and vacuum bellows unit, which positions the support plate and heater assembly. Height of the heater surface above a fixed datum plane is measured to 0.001 in. with a dial indicator having a least count of  $5 \times 10^{-4}$  in. The dial indicator contacts a rod that is rigidly attached to the support plate.

The vacuum chamber is fabricated from stainless steel and is 30 in. in diameter and 24 in. high. The pumping system includes a 4-in.  $\text{LN}_2$  trap diffusion pump and a 15 cfm pump. During testing, chamber pressure is normally maintained at  $1 \times 10^{-5}$  torr or less.

Instrumentation provided for data acquisition is primarily that required for temperature, pressure, and calorimeter section boiloff measurements. A 10-in., 12-point strip chart recorder is used for monitoring hot-boundary, edge-guard, and guard-reservoir temperatures. Hot-boundary temperatures are measured with a Leeds and Northrop Model 8687 potentiometer. Boiloff-gas temperature is measured with a mercury in glass thermometer in the wet-test meter. Ionization gages are used for vacuum chamber pressure measurement. The calorimeter boiloff-gas flow is measured simultaneously by a thermal-type mass flow meter (Schucoco), and a precision wet-test meter connected in series. Gas pressure in both calorimeter and guard reservoir is maintained within 0.03 in. of Hg by cartesian manostats connected to both flow circuits and located upstream from a mechanical vacuum pump. The manostats are adjusted to maintain the guard reservoir at a pressure of  $0.1 \pm 0.03$  in.

of Hg greater than that in the calorimeter vessel. As the flow measuring devices are sensitive to ambient temperature changes, they are located in a constant temperature box maintained at  $555 \pm 1^\circ\text{R}$ . The mass flow meter output is continuously recorded on a 6-in. strip-chart recorder. Also, a record of the wet-test meter flow, based on one complete revolution (3 liters), is recorded as a function of time. Auxiliary equipment is provided for control of heater temperatures and automatic filling of the guard reservoir.

#### APPARATUS CALIBRATION

During the course of Task 1, calibration tests were made on the apparatus to ensure consistency of the test data.

Experiments were conducted for the following purposes:

- Calibrate wet test and thermal mass flow meters
- Determine any heat leak into the calorimeter section
- Compare heat rate calculated from calorimeter boiloff data with known electrical power input into the calorimeter surface plate
- Evaluate effect of temperature gradients on the apparatus (across the specimen) on specimen thickness measurement

The wet-test meter was calibrated using a water displacement method to force a known volume of gas (saturated air) through the meter. Calibration data for several flow rates are shown in Fig. D-3. The thermal mass flow meter then was calibrated against the wet-test meter using a dry nitrogen gas. The meters were installed in the constant-temperature chamber and operated at the pressure and temperature that are maintained during the conductivity testing. This meter is used both to obtain a continuous record of boiloff and as a check for the wet-test meter.

The heat leak into the calorimeter section through supports, fill and vent tubes, etc., was measured using the configuration illustrated by Fig. D-4. A negligible amount of

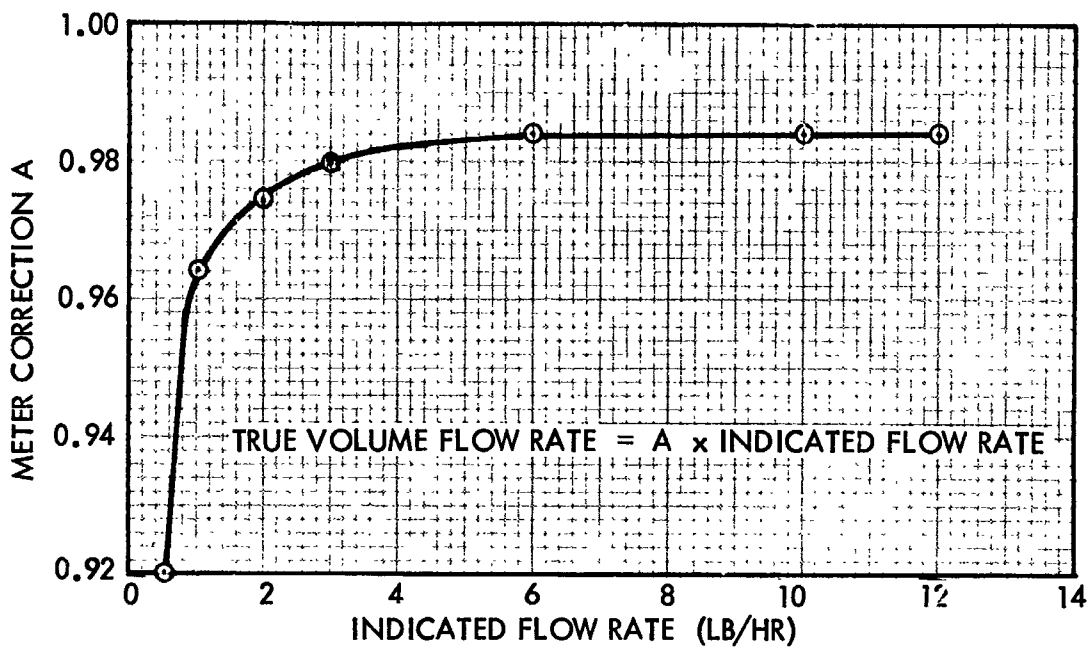


Fig. D-3 Wet-Test Flow Meter Correction

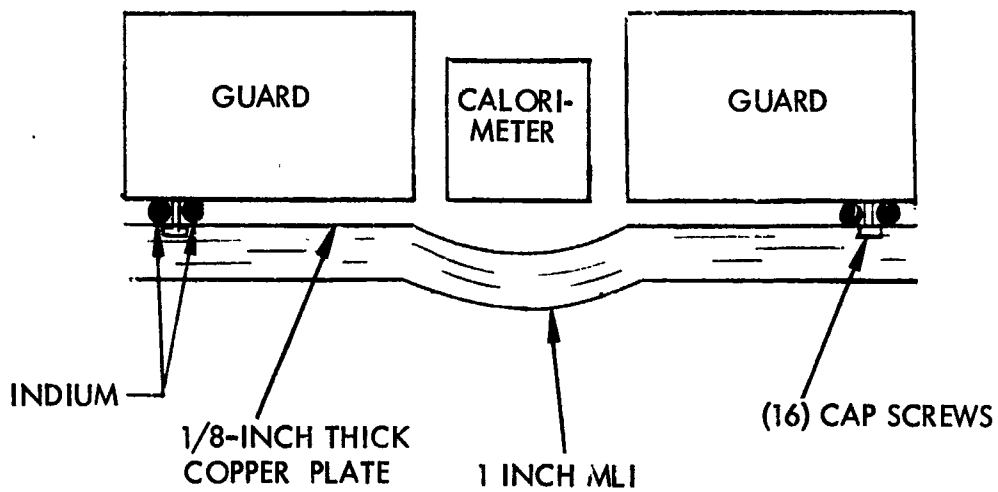


Fig. D-4 Apparatus Configuration for Heat-Leak Test



heat enters the bottom of the calorimeter as it can only transfer heat by radiation exchange with an environment that is at its own temperature because of the thermal shorting of the plate to the guard section. For a  $0.5^{\circ}\text{R}$  temperature difference, a heat rate of  $2 \times 10^{-3}$  Btu/hr would enter the calorimeter across the bottom surface. The heat rate into the calorimeter was measured at three different times during this test program. Measurements were made at the beginning, one-third through, and two-thirds through the program. Heat rates were measured as  $5 \times 10^{-3}$ ,  $3 \times 10^{-3}$ , and  $8 \times 10^{-3}$  Btu/hr. For the last value, the plate temperature was  $1^{\circ}\text{R}$  above the cryogen temperature, which accounts for a heat leak of  $5 \times 10^{-3}$  Btu/hr. A final calibration experiment was conducted at the start of the test program to compare calorimeter heat rate based on boiloff conditions with a known electrical power input to the bottom plate. A 0.5-w resistor was attached to the calorimeter surface plate, using a thermally conductive silver-filled epoxy adhesive. The comparison between electrical power input to the resistor and calorimeter heat rate is shown by Fig. D-5. The maximum deviation between electrical and boiloff heat rates is 8 percent and this occurred at the minimum heat input condition of 0.1 Btu/hr.

The effect of temperature gradients within the apparatus on the specimen thickness measurement was evaluated during the course of Task 1 testing, using a fused-silica disc 3.5 in. in diameter by 0.5 in. thick. This block was placed in the calorimeter, and the hot- and cold-boundary plates were brought in contact with the disc. A thickness measurement was made using the dial indicator with the apparatus at room temperature. The reservoirs were then filled with  $\text{LN}_2$  and after thermal equilibrium was established the dial indicator reading was again recorded. This reading was checked four times by bringing the ram to the fully closed position as determined by pump pressure. The dial indicator reading was within  $1 \times 10^{-3}$  in. of the disc thickness. Correction for contraction of the specimen is less than  $10^{-5}$  in.

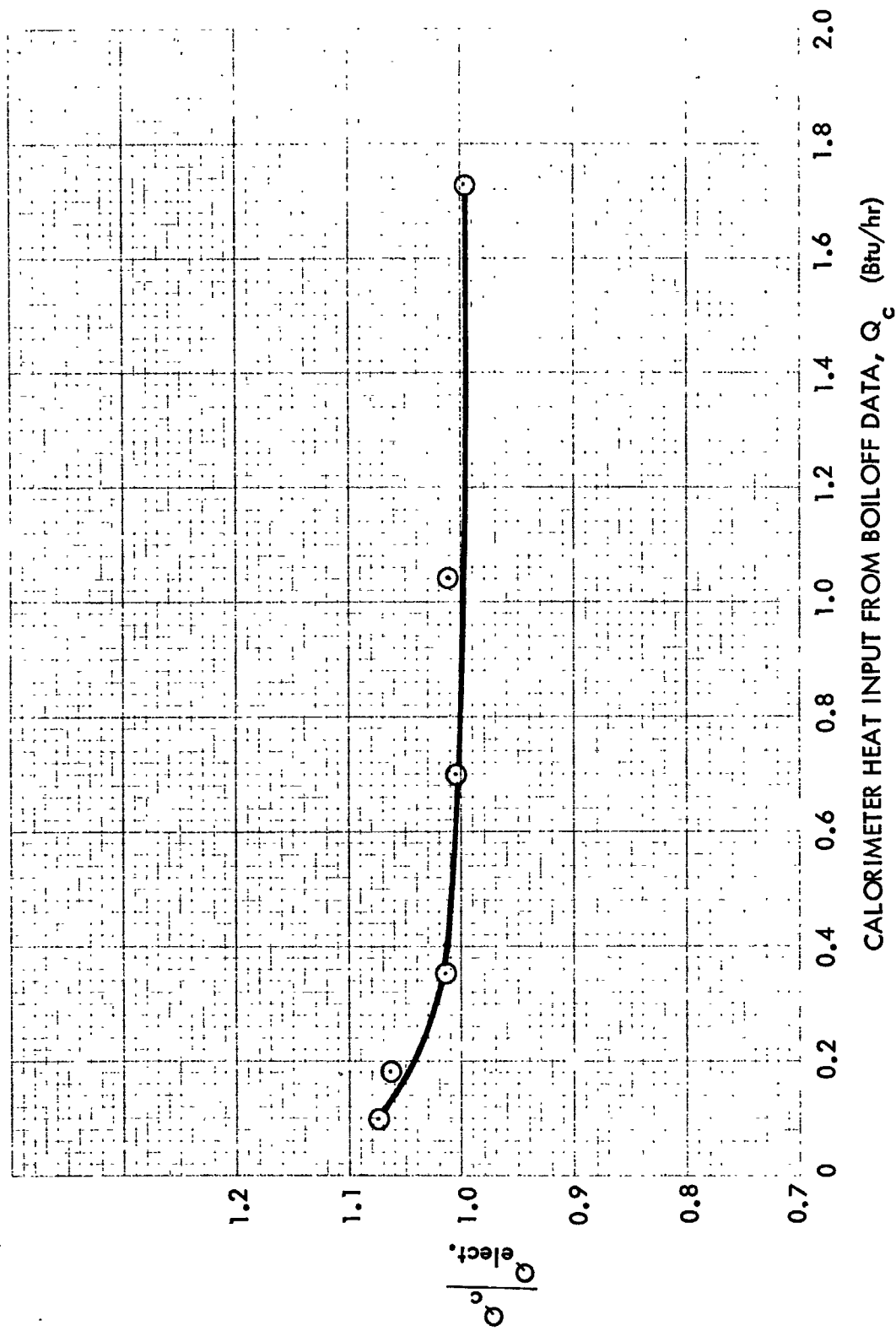


Fig. D-5 Comparison of Ratio of Electrical Heat Input to Calorimeter to Heat Input Measured from Boiloff Data as a Function of Heat Input

## EXPERIMENTAL UNCERTAINTIES

The uncertainty of effective thermal conductivity is a function of the errors associated with the experimental data (i.e., boiloff, temperature, etc.) and those caused by the insulation anisotropy. The latter two-dimensional effect was evaluated experimentally for several of the specimens tested to assess the effects of heat transfer across the sample edge.

The sources of error in the experimental data are as follows:

- Sample thickness measurement. This is a direct function of the specimen thickness and the gage error. Based on the maximum uncertainty of the latter at  $3 \times 10^{-3}$  in., the maximum uncertainty in thickness varies inversely in the form,  $\delta(\Delta x) = \frac{0.3}{\Delta X}$ , where  $\Delta X$  is in inch units. The percentage maximum uncertainty for the thinnest specimen tested is 6.09.
- Mass flow rate. Based on meter calibration data, the volume flow rate has a maximum uncertainty of 1 percent. The gas density uncertainty is 2 percent (considering errors in pressure and temperature measurement), which yields a maximum uncertainty of 3 percent in mass flow rate.
- Calorimeter heat rate. This error is calculated from the electrical input calibration data. For the lowest effective thermal conductivity values measured with the apparatus, the calorimeter heat rate was 0.09 Btu/hr. This corresponds to an error of 10 percent, which decreases to less than 0.5 percent for the highest measured heat rates.
- Temperature difference. The maximum uncertainty in temperature difference between hot and cold boundaries is 1 percent.

The maximum error, based upon the measured data, in the sum of the above individual maximum errors.

$$\delta(k_e) = \delta(\Delta x) + \delta(\Delta T) + \delta(Q_c)$$

The errors associated with two-dimensional heat transfer in the specimens were evaluated from experiment data for several edge-guard temperatures. Heat flux is measured with the edge at 520° R and at 145° R for the maximum specimen thickness. The maximum error is then assumed to be the difference between these two conditions. Maximum error measured was 10 percent and this was for the Mylar closed-cell foam composite, which was 1/2-in. thick. A 4-percent maximum error was determined for the Mylar/silk netting at a thickness of 1/4 in. For thicknesses less than 1/8 in., the two-dimensional uncertainty is less than 1 percent. This error is applied only in the minus direction; that is, the measured heat flux may be high due to the edge temperature so the calculated conductivity is probably a maximum of 10 percent too high from two-dimensional effects.

On the basis of the measured experimental parameters, the maximum uncertainty in effective thermal conductivity varies from 5 to 14 percent as conductivity decreases from  $5 \times 10^{-4}$  to  $2 \times 10^{-5}$  Btu/hr-ft-°R. The maximum uncertainty is between 10 and 24 percent for the data reported herein. Error bands for each data point appear in the graphical presentations of the data.

#### EXPERIMENTAL PROCEDURE

After assembly of the insulation specimen, its uncompressed height is measured. The specimen is placed on a flat surface and a dial gage is used at four locations around the specimen. An average is used in reporting the data. The FPC specimen thickness gage is verified by comparison with gage blocks placed between the hot- and cold-boundary surfaces. The specimen is then placed in the apparatus, the cryogen reservoirs are installed, and the chamber is evacuated. When chamber pressure reaches  $1 \times 10^{-5}$  torr, the specimen thickness is set to 90 percent of its uncompressed thickness. The cryogen reservoirs are filled and power is applied to the heaters. Use of slight compression merely ensures that the specimen and plate are in contact. The test is continued until equilibrium conditions are achieved as determined by pressure, temperature, and bolloff data over a 6- to 10-hr period.

Typically, test periods are 24 to 48 hr. At the completion of a test, the specimen thickness is decreased to the next desired setting. Normally the procedure has been to continually decrease thickness. In Specimen 11 tests, however, the hysteresis of the specimen was checked and the thickness at first decreased; increased thickness was then tested.

Data recorded during a test for heat-transfer calculations are boiloff flow, as determined by both wet-test and mass flow meters; gas temperature at the wet-test meter; calorimeter, guard, wet-test meter, and vacuum chamber absolute pressures; hot surface, edge, and guard reservoir temperatures; and sample thickness. Effective thermal conductivity of the sample is calculated from

$$K_c = \frac{Q_c \Delta X}{A_c \Delta T}$$

Where  $Q_c$  is the calorimeter heat rate (Btu/hr),  $\Delta X$  is sample thickness based upon distance between hot and cold surface plates (ft),  $A_c$  is calorimeter plate area (ft<sup>2</sup>) and  $\Delta T$  is the temperature difference between hot and cold surface plates (°R).

$Q_c$  is calculated from the mass flow rate of the boiloff gas times the latent heat of vaporization of the nitrogen at 30 in. of Hg and 139°R (86 Btu/lb). Mass flow rate is calculated from the wet-test meter data and verified by the thermal mass flow meter. Volume flow rate is converted to mass flow rate using wet-test meter pressure and temperature with the correction for gas saturated with water vapor. Agreement between mass flow rates is within 3 percent.

N70-30606

## Appendix E

### CALORIMETRIC EMITTANCE AND REFLECTANCE MEASURING EQUIPMENT

This appendix describes all of the equipment and procedures used to measure the shield emittance and reflectance data presented in Task 1.

#### DESCRIPTION OF CALORIMETRIC APPARATUS

The apparatus shown in Fig. E-1 consists of a copper supporting structure for the sample and black body receiver and a vacuum-tight stainless steel shell that surrounds the supporting structure. Vacuum access to the shell is provided through a 1-in. stainless steel tube welded in place.

The entire apparatus is fitted to a 30-liter, double-walled dewar. The dewar's inner section can be filled with either liquid nitrogen or liquid hydrogen, thus providing a low-temperature thermal ground for the apparatus. With liquid nitrogen in the dewar's guard section the shell assembly can be kept completely covered with a cryogenic fluid for a period of 24 hr.

The 2-1/2-in. diameter by 3/16-in.-thick aluminum sample substrate is clamped to the supporting structure through a 1/2-in. OD by 10 mil (wall thickness) stainless steel tube, which is epoxied to its back face. Sample temperature is controlled from 100° to 540° R by a 200-ohm spiral-wound heater mounted to its back face. Also, clamped to the sample's back face is a Rosemont Engineering Co. 104 AH1 platinum resistance thermometer. Using calibration data supplied by Rosemont, this thermometer is accurate to  $\pm 0.05^\circ \text{R}$ .

The black body receiver consists of a 2-1/2-in.-OD by 1-1/4-in.-high aluminum shell assembly, which is open at one end. The interior of the shell is fitted with an array of



1-1/2-in.-long aluminum tube and painted with Cat-a-Lac flat black paint. The geometry of the assembly, coupled with the high absorptance of the black paint, produces a very effective black body with an absorptance of 0.98 for the thermal radiation involved in this experiment.

The black body is clamped to the supporting structure through a 1/2-in. rod or tube of varying materials. By using different thermal links the black body equilibrium temperature can be controlled.

The black body back face is equipped with a Texas Instruments germanium resistance thermometer or a Rosemont Engineering Co. platinum resistance thermometer, depending on the expected temperature of the black body receiver. For calibration purposes the black body is also equipped with a 200-ohm carbon resistor heater.

#### EXPERIMENTAL PROCEDURE

The procedure consists of first making emittance power measurements and then calibration measurements.

##### Emittance Measurement

The black body and sample are clamped in place with the front faces spaced approximately 30 mils apart. The shell assembly is then bolted together and lowered into the 30 liter dewar. While at room temperature the apparatus is evacuated to a pressure of  $10^{-5}$  mm Hg. Liquid nitrogen is then added to the dewar's guard section while the space surrounding the shell assembly is filled with liquid hydrogen. The pressure is then reduced to  $10^{-7}$  mm Hg.

After allowing both the sample and black-body receiver to cool to ground temperature, the sample heater is set for the desired sample temperature. The thermal energy from the sample's front surface increases the temperature of the body. For this



series of measurements, the black-body thermal link was chosen so that black-body temperature would not exceed 70° R when using liquid hydrogen as the thermal ground. This minimizes the radiation energy lost by the black-body receiver, both to the blackened shell walls and to the front face.

Once sample and black-body temperature equilibrium are attained (approximately 18 hr), their respective temperatures are recorded. A four-lead technique is used for these measurements. A Leeds and Northrop K-3 potentiometer is used for voltage measurements. Current measurements are made using a precision standard resistor in conjunction with the K-3 potentiometer.

#### Calibration Measurements

To define the thermal energy reaching the black body from the sample, it is necessary to calibrate the black-body receiver. This is accomplished by allowing the sample to cool to the cryogenic bath temperature and supplying heat energy to the receiver through a 200-ohm carbon resistor heater mounted to its back face. Once black-body thermal equilibrium is attained, the power dissipated in the carbon resistor is measured and the temperature (thermometer resistance) is recorded. The process is then repeated for different power levels. A curve of black-body temperature versus power input to the black body then can be generated. This technique produces a very reproducible curve, since not only the black-body thermal link but all the leads to the resistances mounted on its back face are thermally grounded to the cryogenic bath. Power measurements are made using the four-lead technique with the K-3 potentiometer and a precision standard resistor.

## EMITTANCE CALCULATIONS

### Nomenclature

$A_b$	black body functional area, $\text{ft}^2$
$A_s$	sample frontal area, $\text{ft}^2$
$a_b$	black body absorptance, dimensionless
$a'_b$	black body absorptance for sample radiation at $T_C$ and sample at $37^\circ$ or $140^\circ\text{R}$ , dimensionless
$a_s$	sample absorptance for black body radiation at $T_b$ and sample at $T_s$ , dimensionless
$a'_s$	sample absorptance for black body radiation at $T_b$ and sample at $37^\circ$ or $140^\circ\text{R}$ , dimensionless
$F$	sample to black body view factor = black body to sample view factor, dimensionless
$Q_C$	calibration power input (heat flux), BTU/hr
$Q_L$	heat flux to black body thermal link, BTU/hr
$T_b$	black body temperature, $^\circ\text{R}$
$T_C$	sample temperature for calibration ( $37^\circ$ or $140^\circ\text{R}$ )
$T_s$	sample temperature, $^\circ\text{R}$
$Y_C$	heat flux from black body to wall during calibration, BTU/hr
$Y_s$	heat flux from black body to wall during sample run, BTU/hr
$\sigma$	Stefan-Boltzmann constant, $1.71 \times 10^{-9} \text{ BTU/hr-ft}^2\text{-}^\circ\text{R}^4$
$\epsilon_b$	black body emittance at $T_b$ , dimensionless
$\epsilon_s$	sample emittance at $T_s$ , dimensionless

With a radiating sample present the heat flux reaching the black body thermal link is equal to the radiated sample energy, which is absorbed by the black body, minus the radiated black body energy which is absorbed by the sample or the chamber walls.

Therefore:

$$Q_L = A_s \sigma T_s^4 F \frac{a_b \epsilon_s}{1 - F^2 (1 - \epsilon_s)(1 - a_b)} - A_b \sigma T_b^4 F \frac{a_s \epsilon_b}{1 - F^2 (1 - \epsilon_b)(1 - a_s)} - Y_s \quad (E.1)$$

and during calibration the heat flux reaching the link is

$$Q_L = Q_C - Q_R - Y_C$$

where

$$Q_R = A_b \sigma T_b^4 F \frac{a'_s \epsilon_b}{1 - F^2 (1 - \epsilon_b)(1 - a'_b)} - A_s \sigma T_c^4 F \frac{a'_b \epsilon_s}{1 - F^2 (1 - \epsilon_s)(1 - a'_s)} \quad (E.2)$$

Thus,  $Q_L$  has been defined with a radiating sample present and for a calibration heat input  $Q_C$ ; therefore, for corresponding black body temperatures combining Eqs. (E.1) and (E.2) yields

$$\begin{aligned} & A_s \sigma T_s^4 F \frac{a_b \epsilon_s}{1 - F^2 (1 - \epsilon_s)(1 - a_b)} - A_b \sigma T_b^4 F \frac{a_s \epsilon_b}{1 - F^2 (1 - \epsilon_b)(1 - a_s)} - Y_s \\ &= Q_C - A_b \sigma T_b^4 F \frac{a'_s \epsilon_b}{1 - F^2 (1 - \epsilon_b)(1 - a'_s)} + A_s \sigma T_c^4 F \frac{a'_b \epsilon_s}{1 - F^2 (1 - \epsilon_s)(1 - a'_b)} - Y_C \end{aligned} \quad (E.3)$$

At equal black body temperatures  $Y_s = Y_C$ . Also, since  $T_b$  and  $T_c \ll T_s$  the second term on the left side and the second and third terms on the right side of Eq. (E.3) can be neglected which introduces an error calculated to be less than 1 percent.

The resulting equation is

$$Q_C = A_s \sigma T_s^4 F \frac{a_b \epsilon_s}{1 - F^2 (1 - \epsilon_s)(1 - a_b)} \quad (E.4)$$

The emittance  $\epsilon_s$  can now be calculated because all of the terms in Eq. (E.4) are known, including  $a_b$ . The latter was calculated using an iterative process and data obtained by substituting a black body radiator identical to the absorber for the sample. The emittance, or absorptance, of the black body was found to be  $0.98 \pm 0.01$  from  $100^\circ$  to  $470^\circ R$ .

#### ERROR ANALYSIS

Most of the errors in this measurement technique can be attributed to errors in measuring the terms in Eq. (E.4)

$$\text{Probable Error} = \sqrt{\left(\frac{\Delta Q_c}{Q_c}\right)^2 + \left(\frac{\Delta T_s}{T_s}\right)^2 + \left(\frac{\Delta F_{sb}}{F_{sb}}\right)^2 + \left(\frac{\Delta a_b}{a_b}\right)^2}$$

where

$$\frac{\Delta Q_c}{Q_c} \approx 0.5\%$$

$$\frac{\Delta T_s}{T_s} \approx 1.0\%$$

$$\Delta F_{bs} \approx 1.0\%$$

$$\frac{\Delta a_b}{a_b} \approx 1.0\%$$

In addition to these, other errors include:

- Heat transfer due to residual gas conduction,  $< 0.1$  percent
- At the lowest sample temperature, changes in both temperature due to shifts in vapor pressure over the bath,  $< 2$  percent
- Error introduced because  $a'_g \neq a''_g < 0.5$  percent

Thus, the approximate error for the values of  $\epsilon_g$  in the  $200^\circ$  to  $540^\circ$  R range is 2.0 percent. For the lowest sample temperatures ( $\approx 140^\circ$  R) the estimated error is 2.5 percent.

## DESCRIPTION OF REFLECTANCE APPARATUS

### Cary Spectrophotometer

A Cary Model 14 double-beam spectrophotometer (Fig. E-2) is used for the measurement of near-normal reflectance in the spectral range of 0.27 to 1.8 microns. The sample surface and the standard (vacuum-deposited silver) are diffusely illuminated by the sphere, and continuous comparison is made between the near-normal reflectance of the specimen and that of the standard.

### Gier-Dunkle Integrating Sphere With Monochromator

A Gier-Dunkle Model SP 210 integrating sphere with Perkin-Elmer Model 98 monochromator is used for the measurement of near-normal and angular absolute spectral reflectance from 0.20 to 2.5 microns. In this apparatus the specimen, mounted inside the sphere, is illuminated monochromatically, and the reflected energy is collected by the high-reflectance surface of the sphere. Reflectance measurements are made using single-beam, point-by-point measuring techniques.

The apparatus has a higher degree of accuracy than the Cary Model 14. The Cary sphere is small and has relatively large apertures for entrance and exit of sample,

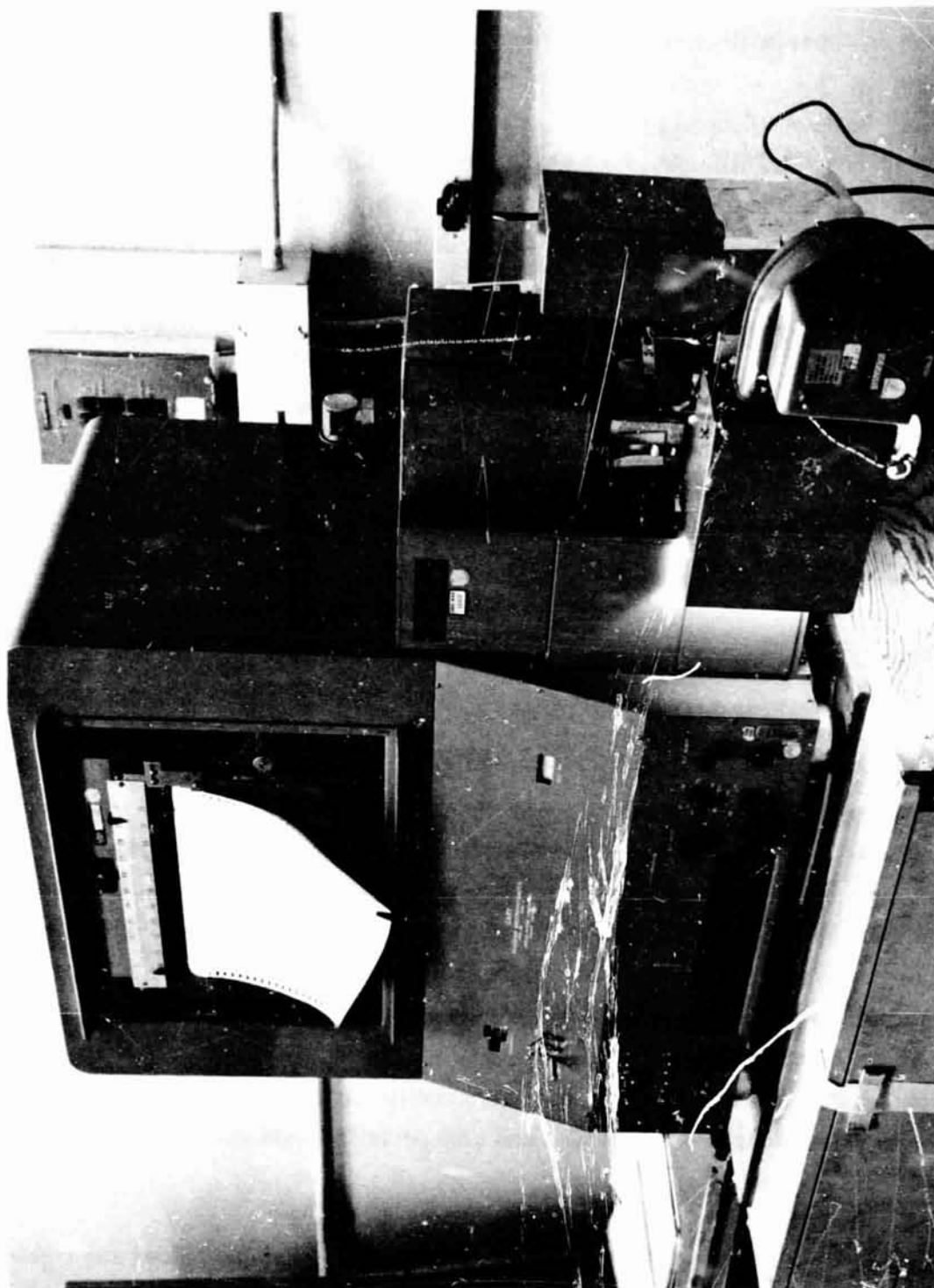


Fig. E-2 Cary Spectrophotometer

reference, and sphere illumination beams. The sphere is illuminated by external optics, and the reflected sample energy is directed to the entrance slits of the monochrometer. Because of large apertures, a bright spot from the illuminating beam, and the small sphere size, it is obvious that the instrument has significant sources of error. The absolute magnitude of error is considerably reduced by establishing operational procedures which circumvent the major difficulties. Normal operations in this laboratory call for calibration of the system against a known first-surface aluminum mirror. This is done by setting reflectance values at each wave-length to correspond to the known mirror properties. Unknown samples are then run, and the reading is obtained in absolute reflectance units. This procedure minimizes but does not eliminate effects of the apertures and bright spot. The data obtained are relative in the sense that the instrument is initially calibrated against a known surface. Therefore, continuous checks must be made to assure the validity of the values used for the calibration. The instrument is used as a control for large numbers of samples since it is fast, easily operated, and within limits has reasonable accuracy. Where changes in spectrum or comparisons among identical samples are desired, it is a highly useful laboratory pool.

In view of the relative nature of Cary results, it is also necessary to obtain a limited number of absolute measurements to verify the Cary spectrum. These measurements are performed using a single-beam Gier-Dunkle integrating sphere attached to a Perkin-Elmer Model 98 monochrometer. This sphere is much larger than the Cary (9.5-in. diam.), has only two small apertures (entrance port 1-in. diam., detector area 1-in. diam.), and does not suffer from direct sample illumination of the detector. The sample is centrally mounted in the sphere and may be rotated at angles from 0 to 90 deg relative to the entrance port. When the sample is normal to the port, its shape factor to the hole is approximately 0.011. This construction permits direct measurements of the absolute reflectance of test samples and also permits cross checks which verify the validity of data obtained.

In normal operation, a 1-in. disc sample is mounted on the sample holder and rotated 10 deg off axis from the entry port. Monochromatic energy is then directed alternately

to the sphere wall and then to the sample. Detector response is ratioed for each beam position with the ratio of response being the absolute reflectance of the sample. This procedure is repeated for each required wavelength throughout the spectral region 0.50 to 2.5  $\mu\text{m}$ .

The Gier-Dunkle instrument can determine spectral reflectance with an accuracy of 1 percent, and can be cross-checked to assure that operation is producing this precision. Sample rotation may also be used to determine the extent of entry port losses so corrections can be applied for this effect. However because of its manual operation the measurements are time consuming and must be accomplished by highly skilled personnel. Therefore, only a limited number of such determinations were made on test samples.

When initial measurements were made using the Gier-Dunkle sphere and the results used to calibrate Cary measurements on identical samples, it was possible to obtain accuracies of  $\pm 2$  percent in reflectance.

#### GIER-DUNKLE HEATED-CAVITY REFLECTOMETER

To measure spectral reflectance between 2 and 25 microns, a Gier-Dunkle Model HC-300 heated cavity reflectometer is used in conjunction with a Perkin-Elmer Model 98 monochromator and a Brewer Model 129 chopper-amplifier system. The optical system is a single-beam, double-pass arrangement. Near-normal reflectance measurements are made point-by-point at each wavelength of interest. For most sample surfaces, the limit of precision for each reflectance measurement is on the order of  $\pm 0.001$  to  $\pm 0.002$ , and the maximum absolute error lies between  $\pm 0.005$  and  $\pm 0.010$ , depending on the surface characteristics and reflectance of the sample. A brief discussion of the major sources of measurement error is given in the following paragraphs.

The heated cavity reflectometer contains a cooled sample that is irradiated by a surrounding hot cavity. Radiant flux, reflected from the sample in a small solid angle about the polar and azimuthal angles to the surface, is viewed. The major



sources of error are associated with nonuniformity of the cavity wall intensity and with sample emission. Principal factors contributing to nonuniform intensity are (1) the presence of the water-cooled sample and sample holder, (2) specularity of the cavity walls, (3) temperature gradients along the cavity walls, and (4) the presence of the viewing port. By careful design of the cavity and sample-holder geometry and of the cavity heater circuits, the effects of the first three factors are reduced to negligible proportions relative to the viewing-port error. For a perfectly diffuse sample, the shape factor from the sample to the viewing port is  $0.035 \cos \theta$ . Thus, at near-normal viewing angles, an error of 3.5 percent is introduced. For a perfectly specular sample, the measurement at  $\theta = 0$  deg is invalid since the reflected flux viewed from the sample originates from the viewing port itself. At angles of  $\theta$  greater than about 15 deg, however, there is no error for a specular sample since the reflected flux then originates entirely from the cavity wall. For an arbitrary sample that is neither perfectly diffuse nor perfectly specular, some knowledge of the reflectance distribution function or bidirectional reflectance is necessary to assess the viewing-port error.

Measurement error due to sample emission is negligible for high-reflectance, metallic samples because of their low emittance characteristics. For low reflectance, poorly conducting dielectric sample materials, the emission error can usually be minimized by using thin specimens on good conducting substrates and by increasing the sample coolant flow rate to maintain the surface temperature of the sample near room temperature. For severe cases, where sample emission cannot be avoided, a thermocouple can be attached to the sample to obtain a measure of its temperature, and an analytical correction applied to subtract out the emitted energy at each wavelength.

Sources of error associated with stray energy scattering by the optical components of the monochromator are minimized by the use of a scatter plate of long wavelengths (i.e.,  $\lambda > 11 \mu\text{m}$ ) and by filters. A glass filter with a long wavelength cutoff of  $4.5 \mu\text{m}$  is used for measurements at  $\lambda < 4 \mu\text{m}$ , and black polyethylene filters are used for measurements at  $\lambda > 20 \mu\text{m}$ . For measurements between 2 and  $14 \mu\text{m}$ , a sodium chloride prism is used in the monochromator; for measurements between 11 and  $25 \mu\text{m}$ , a potassium bromide prism is used.

## COMPARITIVE EMITTANCE MEASUREMENT

### Lion Optical Surface Comparator (Emissometer)

Lion Research Corporation Model 25 emissometer (Fig. E-3) is used for comparative measurement of the emittance of reflective coatings on multilayer radiation shields. This unit is a radiometric comparison instrument that functions in the following way: First, the detector views a 1.5-in.-diam. surface area. Energy emitted from the surface passes through a KRS-5 window and is detected with a cooled thermopile that is mounted in an evacuated chamber. Before each measurement, the detector output is calibrated using three standards. The temperatures of the standard and the specimens are kept the same for a measurement. An aluminum standard having a total hemispherical emittance of 0.035 is used for the reflective shield materials.

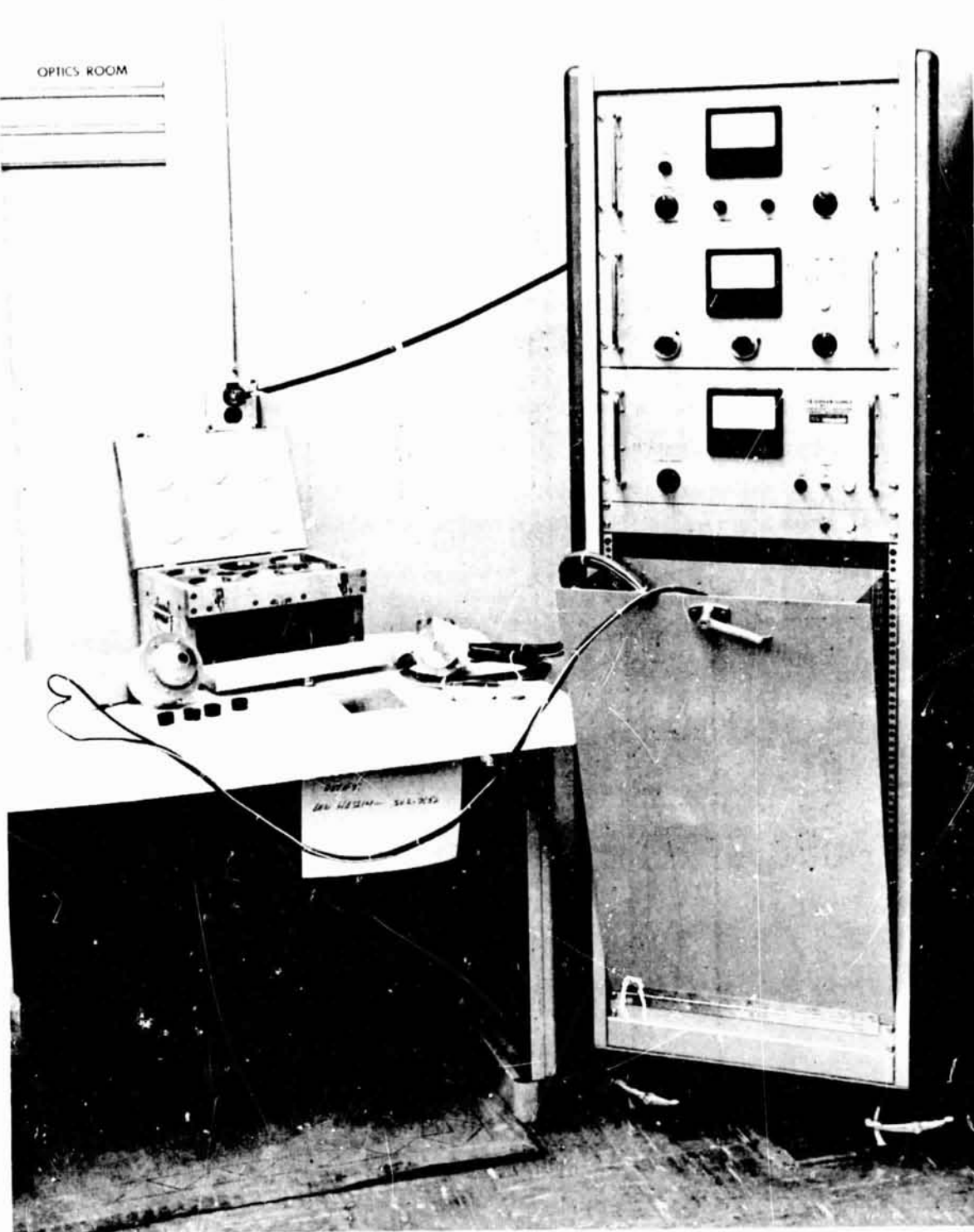


Fig. E-3 Lion Research Corporation Optical Surface Comparator

N70-20607

## Appendix F

### PROPOSED SPECIFICATION FOR REFLECTIVE-SHIELD EMITTANCE

The purpose of this proposed specification is to present methods which can be used by the suppliers and the customers (Government and aerospace industry) to evaluate the emittance of vacuum-metallized plastic-film materials that are used as the reflective shields of multilayer insulation. The customer could specify material of a certain emittance (at room temperature) and would employ the methods proposed herein to ensure compliance with the specification. The supplier could use the same measurement techniques for quality control.

The ideal test method is one that directly and accurately measures the total hemispherical emittance of the material over the temperature range at which it is to be used. This type of test, however, is time consuming and costly. For example, the test equipment is expensive and typical test times are 1 to 2 days for each temperature point. Also the complex apparatus requires skilled technical personnel to perform the measurement and to interpret the raw data. Ideally, the method should be one which can be accomplished in a short time by general quality assurance laboratory technicians. The proposed method meets the time requirement, but the tests must be performed by qualified laboratory personnel.

Two basic methods fulfill the requirements for inspection of the metallized material. One employs a radiometric comparison of the energy over a wide spectral band from the specimen to that from a well-characterized standard.

The second is based upon spectral reflectance measurements. Both methods are used to compare a number of metallized films and their calculated emittance values with total hemispherical emittance data. The Lion Model 25 emissometer was used for comparative data. Another device (Ref. F-1) is on the market which should be an

acceptable substitute for the Lion apparatus, and it does not require the careful specimen and standard temperature control necessary for the Lion.

A Gier-Dunkle heated cavity reflectometer and integrating sphere and a Beckman DK-2 spectrophotometer were used for the reflectance measurements. The heated cavity is suitable for measurement to long wavelengths, which is desirable for calculation of total normal room-temperature reflectance. The integrating sphere device covers the ultraviolet, visible, and near-infrared spectral regions (2.5 to 2.8 $\mu$ ). They are somewhat less costly and are in more general use in the laboratories of vacuum metallizing. If these are used, certain assumptions must be made regarding the correlation between short- and long-wavelength reflectance of the metallized surfaces.

For the comparative method, the room-temperature emittance data from the Lion are compared with calorimetric total hemispherical emittance data in Table F-1. An aluminum-foil standard of  $\epsilon_{TH} = 0.035$  was used for all comparative measurements.

Table F-1

COMPARISON OF LION EMITTANCE WITH TOTAL HEMISPHERICAL EMITTANCE

Material	$\epsilon_L$ (arc)	$\epsilon_{TH}$
Gold/Kapton	0.023	0.027
D-A-M (0.25 mil)	0.028	0.029
S*-A-M (0.15 mil)	0.035	0.032
D-A-M (crinkled)	0.030	0.030
S-A-M (0.25 mil)	0.040	0.030

\*Silver.

The Lion emissometer emittance agrees with the calorimetric values within  $\pm 0.005$  except for the NRC-2 material which was 0.010 higher. This is due to the effect of

the crinkled surface on the Lion measurement. The D-A-M crinkled material was smooth and the surface effect was not as pronounced. As a specification,  $\epsilon_{TH}$  is 0.03 or less, and  $\epsilon_{Lion}$  should not exceed 0.030.

This device should be used for receiving or acceptance testing. The reference standard should be verified by the customer and duplicate standards prepared; one should be used by the supplier and one by the customer. Also, it is recommended that a procedure be established for periodic verification of the condition of the standards. An acceptable standard for the device is Fasson aluminum foil (Lockheed spec-LAC 24-4051 Type II) which was used in the present contract program.

The spectral reflectance method covers two wavelength regions. The heated cavity uses the region of 5 to 25  $\mu\text{m}$ , while the integrating sphere covers the region of 2.5 to 2.8  $\mu\text{m}$ . The former yields absolute near-normal spectral reflectance values. These are integrated over the room temperature blackbody spectrum to obtain room-temperature reflectance. The room-temperature normal emittance is calculated from  $\epsilon_N = 1 - \rho_N$ . To obtain a room-temperature total hemispherical emittance of 0.030, near-normal emittance should not exceed 0.022. Similarly, for  $\epsilon_{TH}$  of 0.035 and 0.025,  $\epsilon_i$  should not exceed 0.025 and 0.018, respectively.

For the integrating sphere (MgO coated), spectral reflectance is measured from 1.5 to 2.5  $\mu\text{m}$ . This region was chosen because the gold and aluminum reflectance remain relatively constant from 1.5  $\mu\text{m}$  to much longer wavelengths. The Gier-Dunkle sphere yields absolute reflectance, but the Beckman DK-2 measures reflectance relative to a standard. For this work, the standard was a second surface mirror (8 mils of fused silica with a silver coating). The reflectance data from both devices for the test specimen of this program are given in Table F 2.

Table F-2

## COMPARISON OF SHORT-WAVELENGTH REFLECTANCES

Material	$\rho_{\text{NHC}}^{(a)}$	$\rho_{\Delta\lambda \text{ G-D}}^{(b)}$	$\rho_{\Delta\lambda \text{ DK-2}}^{(c)}$
Gold/Kapton	0.990	0.995	0.986
D-A-M	0.979	0.976	0.961
D-A-M	0.976	0.975	0.967
D-A-M, Crinkled	0.981	0.985	0.989
S-A-M	0.975	0.967	0.957
S-A-M Crinkled	0.975	0.960	0.945 (0.860) <sup>(d)</sup>

(a) Heated cavity from 2 to 25 $\mu\text{m}$

(b) Absolute value from 1.5 to 2.5 $\mu\text{m}$

(c) Relative to second surface mirror standard ( $\rho = 0.990$  at 1.5, 0.966 at 2.0, and 0.996 at 2.5  $\mu\text{m}$ ) from 1.5 to 2.5  $\mu\text{m}$

(d) Surface striations in vertical directions. This shows effect of surface specularity on measurement in the sphere.

The short-wavelength reflectance data show a large variation when compared to the heated-cavity data. The results for the crinkled surfaces are particularly poor with this method as is shown by the S-A-M crinkled specimen with the structures in two directions. The DK-2 has a small integrating sphere, which makes the measurement much more sensitive to the specimen surface geometry. Based upon these limited data, poor correlation was obtained between short-wavelength reflectance, total normal reflectance, and total hemispherical and emittance.

As a result, it is recommended that either a comparison apparatus (such as the Lion) or heated-cavity reflectance measurement to 25 $\mu\text{m}$  be used for the inspection of metallized plastic substrate reflective-shield material.

N70-30000

## Appendix G

### COMPUTER CODES USED IN STRESS AND THERMAL ANALYSIS OF SUPPORT STRUCTURE AND INSULATION

In the course of providing the best possible stress and thermal analysis of the support structure and insulation in Task 2, several digital computer codes were used. A brief summary of each code used is presented in subsequent paragraphs.

#### STRESS ANALYSIS

Three computer codes were employed in the stress analysis of the conical and strut supports considered in Task 2. These include the following programs.

##### SAND Program

The computer code SAND, developed under the Lockheed Independent Development Program, performs a stability analysis for honeycomb sandwich cylinders subjected to combined uniform axial compression and lateral pressure, either burst or collapse. Cylinder construction details, together with the applied lateral pressure, are required input to the program.

Critical axial loads for general instability, wrinkling instability, and face dimpling are calculated and presented as output, along with the critical core-crushing pressure. General instability is calculated using the methods and data of Ref. G-1, which have been extended to apply to cylinders subjected to the combined load environment.

These methods are similar to methods for analyzing conventionally stiffened cylinders for panel and overall instability, except that the present methods also consider transverse shear effects because of their importance in sandwich construction. Methods for the remaining instability modes are taken from MIL-HDBK-23 (Composite Construction). The SAND computer program is coded for sandwich constructions having



the same effective core shear modulus in all in-plane directions; i. e., it applies primarily to square-cell core geometries.

#### MARK IV Program

The MARK IV computer program performs a structural optimization analysis on cylinders stiffened with rings and/or stringers of rectangular cross section and subjected to axial compression plus radial pressure, either burst or collapse. Three buckling modes are considered: local instability, panel instability involving the stringer-wall combination between rings, and overall instability involving the stringer-ring-wall composite. Panel and overall instability are predicted using equation similar to those derived by Baruch and Singer (Ref. G -2). Reduction factors based on work performed at LMSC are applied as needed to these predictions. The criterion for optimum design is identical to that utilized by Zahorski (Ref. G -3) as well as many subsequent investigators. The MARK IV computer program features a minimum of input. It permits the user to place several constraints on the design in order to meet manufacturing and other nonstructural requirements. A detailed description of the optimization analysis, together with nondimensional parametric study results, is presented in Ref. G -4.

#### SCAR Program

The SCAR computer program (Stiffened Cylinder Analysis Routine) solves for the critical buckling loads for cylinders described in input. This program is essentially identical to the MARK IV program except for the driving main program. It is written in general terms and is not limited to integral, rectangular ring/stringer geometries. Any conventional ring/stringer configuration may be analyzed; however, since transverse shear deformations are neglected, sandwich constructions, in which this effect may be important, may not be handled. SCAR may be used to analyze cylinders subjected to hydrostatic pressure, or pure radial collapse pressure may be analyzed as special cases. Input consists of cylinder geometry, material, and

applied radial pressure (materials may be varied in the rings/stringers/wall). Predictions for panel and overall instability are printed out, together with local instability predictions for those elements defined by the input data. A detailed description of the SCAR computer program is presented in Ref. G -5.

#### THERMAL ANALYSIS

The computer code used in computing heat transfer through the tank supports and surrounding insulation was the Complete System Thermal Model (CSTM) program. A description of this code is as follows:

##### Complete System Thermal Model

This computer code was developed under NAS8-11347 and incorporates the ability to perform three-dimensional transient or steady-state heat transfer analysis. The code is written to use a complete difference-formulation of the basic energy relations. As used in Task 2 analysis, steady-state heat transfer was computed and temperature-dependent conductivity of the structure and insulation were used.

The CSTM is capable of simulating by computation in a continuous manner the thermal environments during the tank fill and hold operations, during boost into orbit, in earth orbit, and in deep space. In Task 2 the latter two environments were used.

The code incorporates several valuable features. One feature of the code is the building block routine which automatically mocks-up insulated propellant tank configurations with minimum input information by the engineer. Another feature is the incorporation of gas flow relations which are employed during simulated ascent flight to compute the helium purge gas pressure within the insulation. A detailed description of the CSTM and its capabilities is provided in Ref. G-6.

This code is in frequent use at Lockheed in analyzing heat transfer for cryogenic and noncryogenic applications.

#### REFERENCES FOR APPENDIX G

- G-1 Lockheed Missiles & Space Company, Buckling of Axially Compressed Sandwiched Cylinders, by B. O. Almroth, LMSC Report 6-62-64-9, Sunnyvale, Calif., Jul 1964
- G-2 M. Baruch and J. Singer, "Effect of Eccentricity of Stiffeners on the General Instability of Stiffened Cylindrical Shells Under Hydrostatic Pressure," J. Mech. Engr. Sci., Vol. 5, 1963, pp 23-27
- G-3 A. Zahorski, "Effects of Material Distribution on Strength of Panels, "J. Aeronaut. Sci., Vol. 2, 1944, pp. 247-253
- G-4 Lockheed Missiles & Space Company, Optimum Stiffened Cylinders for Combined Axial Compression and Internal or External Pressure, by A. Bruce Burns, LMSC Report 6-76-66-11, Palo Alto, Calif., May 1967
- G-5 Lockheed Missiles & Space Company, Computer Program for the General Instability Analysis of Ring-Stringer Stiffened Cylinders Subjected to Axial Compression and Lateral Pressure, LMSC Report 4-11-66-1, Palo Alto, Calif., Mar 1966
- G-6 Lockheed Missiles & Space Company, Complete System Thermal Model, Vol. II Final Report, LMSC-A742593-2, Contract NAS 8-11347, Sunnyvale, Calif., 20 Aug 1965

N70-2305

## Appendix H GAS FLOW APPARATUS

The gas flow apparatus used in Task 4 to determine the specific mass flow conductance is described in this appendix.

### DESCRIPTION OF APPARATUS

The experimental apparatus was constructed to obtain data on gas pressure drop and mass gas flow through insulation systems with the gas in viscous, transition, and free molecular conditions. Insulation specimens were constrained in a manner similar to that occurring on an actual installation. Provision was made for cryogenic cooling of the insulation.

Figures H-1, H-2, and H-3 show the apparatus. The insulation sample is wrapped around the 4-in.-diam. by 4-ft-long stainless-steel inner specimen can to a depth of 1 in. The guard can, constructed in two clamshell sections, fits over the outer layer of insulation. The guard can is insulated, and the entire assembly is enclosed in a vacuum case. All insulation joints are sealed with aluminized Mylar tape; and longitudinal movement of the insulation is restricted by a spider fitting at the lower end of the drum, as shown in Fig.H-3.

The drums are installed vertically (Fig.H-2) and gas flow is from top to bottom. Gas is metered before entering the header at the top of the apparatus. For test at cryogenic temperatures ( $\text{LN}_2$  or  $\text{LH}_2$ ), both the outer and inner drums contain the cryogenic at its normal boiling point. Nylon supports and radiation shields are employed to obtain adequate thermal isolation. Fill, vent, and service lines enter the vacuum case through the removable cover plates with O-ring fittings.

Both mechanical and diffusion pumps are used to obtain vacuum conditions. As shown in Fig.H-2, the apparatus is set on the base plate of a standard commercial 6-in.

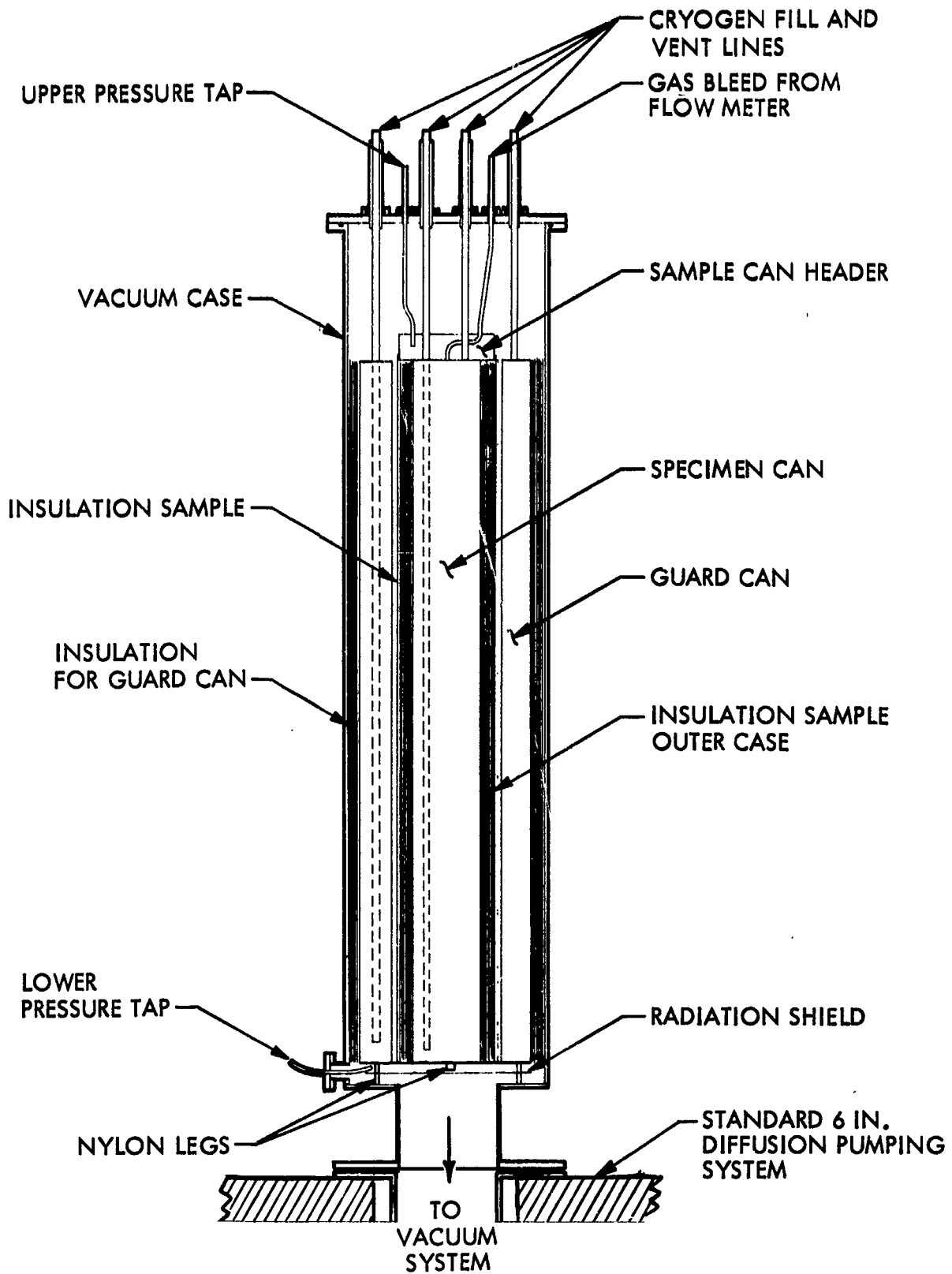


Fig. H-1 Schematic of Gas Flow Apparatus

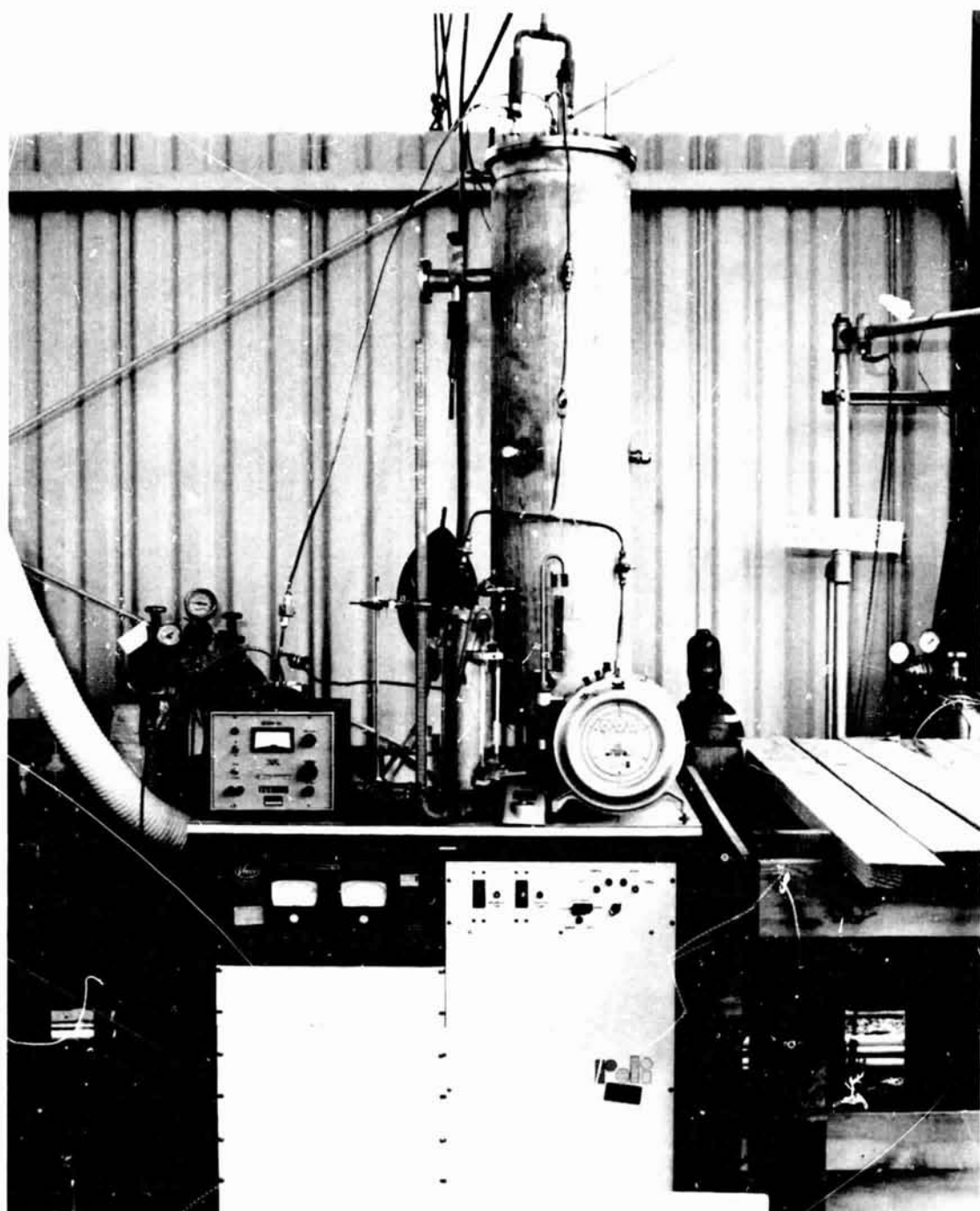


Fig.H-2 Assembly of Gas Flow Apparatus

H-3

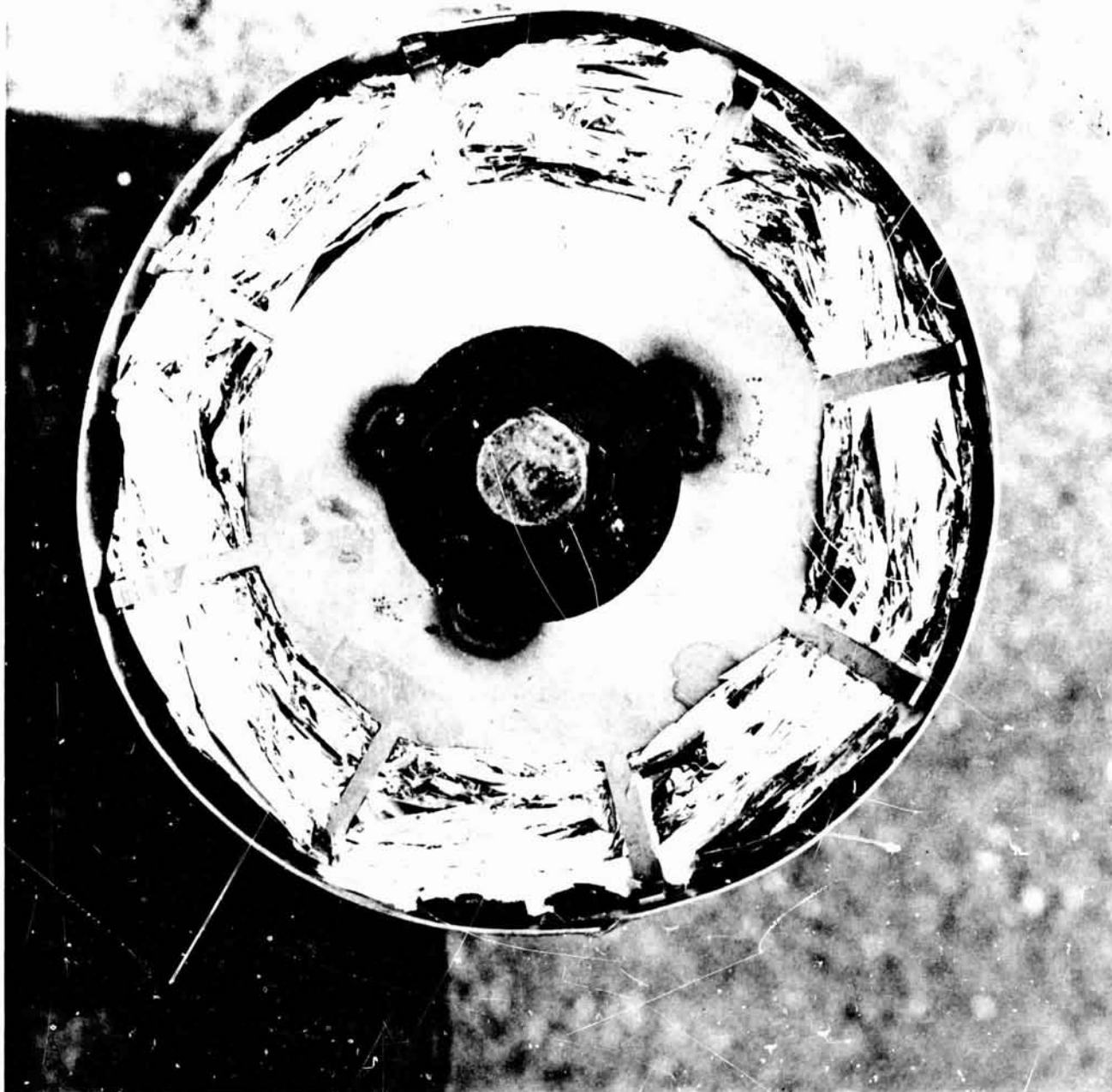


Fig. H-3 Spider Fitting at Lower End of Gas Flow Apparatus Test Drum

H-4

diffusion pump system; at high flow rates, where the downstream pressure increases to  $10^{-3}$  torr, the diffusion pump is bypassed; only the mechanical pump is used. This causes the downstream pressure to rise by one order of magnitude.

## INSTRUMENTATION

Two pressure gages are used for pressure measurement. A Texas Instrument Company fused-quartz pressure gage is used to obtain pressures down to its minimum of  $10^{-2}$  torr, and an alphatron gage is employed to obtain lower pressures. The fused-quartz gage consists of a 20-turn quartz Bourden tube enclosed in a transparent capsule. The tube interior is connected to the unknown pressure, and the capsule interior is connected to a known pressure. Differential pressure across the Bourden tube wall causes a tube deflection which is measured by deflections in an optical mirror system. The gage is insensitive to the nature of the gas, and, after calibration by the LMSC Primary Standards Laboratory, it was found to be as accurate as the comparison standard ( $\pm 0.01$  percent) used by the laboratory. However, the smallest detectable change in pressure on the digital readout amounted to  $1 \times 10^{-2}$  torr. A mechanical pump is used to maintain a pressure in the capsule at less than  $1 \times 10^{-2}$  torr.

The pressure gages are used to determine both upstream and downstream pressures through the use of valves. The gages can be switched from one pressure to the other. Pressure transients are negligible during these changeovers. Also, the data are taken at equilibrium conditions, and the lines from each tap are the same length to reduce possible outgassing errors.

Gas flow rates are measured by two methods. One is a wet-test meter with a range of 17 to more than 200 cc/sec. The other is an oil-displacement meter with a range of 0.05 cc/sec to 3.0 cc/sec. (Experimental flow rates range from 0.06 to 100 cc/sec.) The oil-displacement meter was constructed under a previous contract (Ref. G-1); however, another tube was added to extend its range. Further extension of the meter's range was not practical because of size limitations of the meter. The accuracy of



both meters was determined by calibration to be  $\pm 3$  percent; a volumetric displacement gage was used for the wet-gas meter and dimensional measurements for the oil-displacement meter.

Bottled helium is used in the insulation in all tests and is supplied through a regulator at one-atmosphere pressure. This pressure is maintained constant by using a flexible bag on the supply line downstream of regulators. The two flow meters are placed in parallel between the flexible bag and the test apparatus.

#### INSTALLATION OF INSULATION

Multilayer insulation specimens are wound onto the specimen can using a semi-automatic apparatus which is in regular use for such purposes at the Lockheed Research Laboratory. The insulation is applied by winding it onto the specimen can as the can is rotated on its centers. Installation is straightforward. The only need for extra care is in ensuring that the apparatus is reassembled in a leak-tight condition.

#### TEST PROCEDURE

Flow experiments are begun with low flow rates measured with the oil-displacement meter. Pressure and flow-rate readings are made when the pressure readings reach equilibrium. About 15 min are required to obtain each data point. Further data points are taken at gradually increasing flow rates until the flow rate is too high for measurement by the oil-displacement meter. A five-fold increase in flow rate is necessary between this point and the point at which the wet-test meter can be used. This increase is usually sufficient to require bypassing the diffusion pump at the same time that meters are changed. Tests are made at increasing flow rates until the mechanical pump shows signs of being overworked.

During the testing of the 40-layer/in. specimen of double-aluminized Mylar/Tissu-glas, some unsteady behavior was observed at the higher flow rates, probably due to movement of the insulation. Otherwise, no unusual behavior was observed.

N70-20610

## Appendix I

### TASK 5 OUTGASSING APPARATUS AND GAS ANALYSIS DATA

#### APPARATUS DESCRIPTION

A schematic of the outgassing apparatus is shown in Fig. I-1. The insulation specimen is placed in the specimen chamber, which is 6 in. in diameter and 1-1/2 in. deep (Fig. I-2). The chamber walls and all plumbing lines are of stainless steel because of the low outgassing characteristic of this material. The specimen chamber is sealed from above by a 6-in. Varian vacuum flange with a Teflon gasket. Three thermocouples are provided within the specimen chamber. The top of the chamber is the base of the cryogen tank. The tank is used to provide a constant temperature environment to the specimen chamber. Low-thermal-conductivity fill-and-vent lines enter the cryogen tank through its top (Fig. I-3). The cryogen tank/specimen chamber assembly is enshrouded within an outer vacuum jacket used to assist in thermally isolating this assembly.

The specimen chamber can be either evacuated or purged by a 1-in. -diam., 15-in. -long tube (designated "evacuation tube" in Fig. I-1), which enters the chamber through its bottom. This tube reduces to a 1/4-in. line containing a Nupro bellows needle valve and a Circle-Seal 1/4-in. -diam. shutoff valve. In series with these valves and downstream from them is a second Circle-Seal 1/4-in. -diam. shutoff valve. The 1/4-in. line then leads to a high-vacuum plenum chamber to which the port of a Varian partial pressure gage is attached. The evacuation tube is shaped to direct the pumped gases towards the interior of this partial pressure gage to ensure good sampling.

The high-vacuum plenum chamber is attached to a gate valve and a 6-in. NRC diffusion pumping system (including LN<sub>2</sub> cold trap). The main roughing line, a thermocouple gage, and a line to the reference side of the pressure gage are also connected to the high-vacuum plenum.

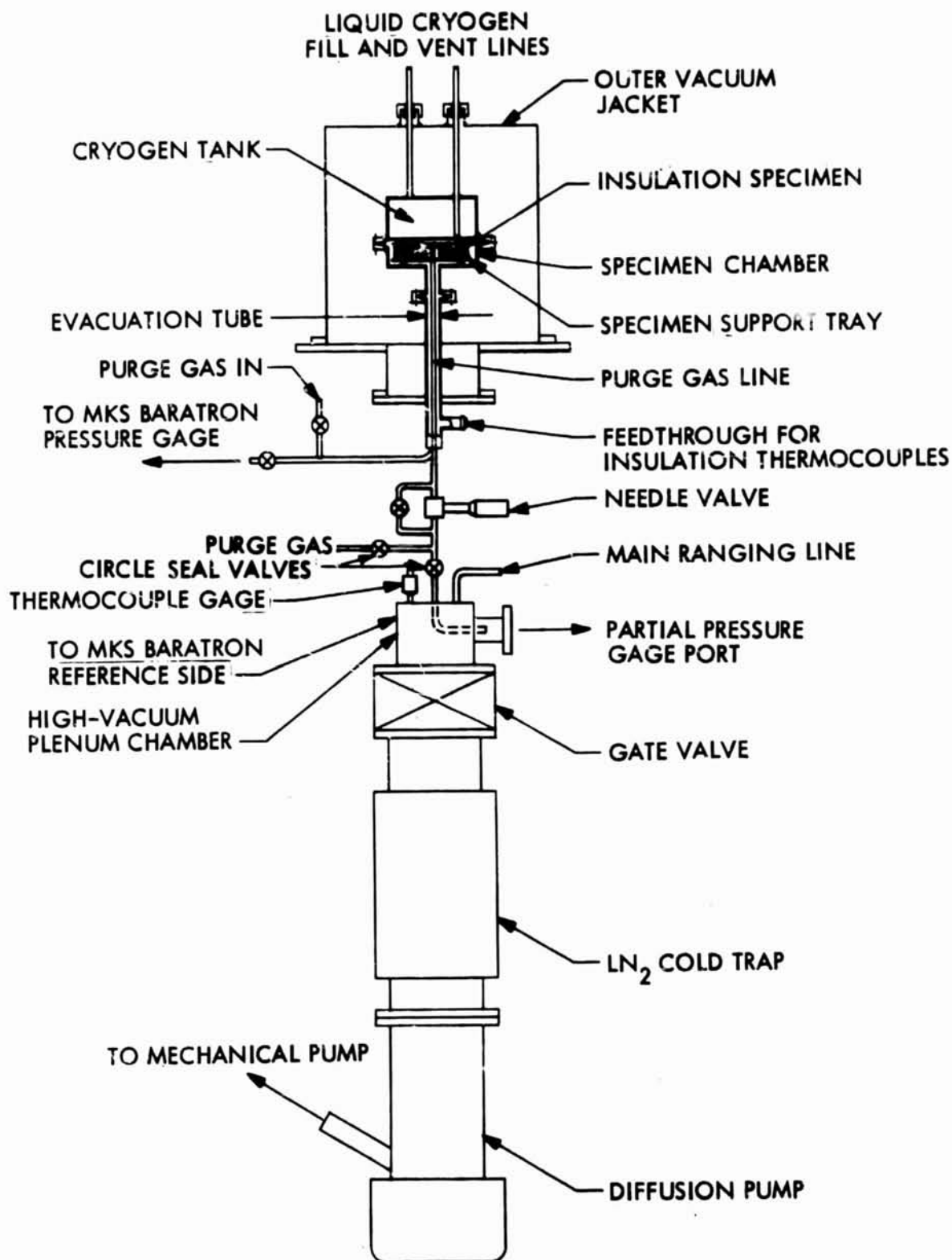


Fig. I-1 Outgassing Apparatus Schematic

I-2



Fig. I-2 Insulation Specimen in Base of Vacuum Chamber



Fig. I-3 Outgassing Vacuum Test Chamber With Coolant Chamber in Place

## PRIMARY INSTRUMENTATION

### Pressure Gage

The pressure gage chosen is an MKS Baratron (Fig. I-4), which senses pressure by the deflection of a thin metal diaphragm. The movement of the diaphragm under a pressure load is detected as a change in capacitance between it and a fixed electrode. The diaphragm is held in a sensing head that isolates it from extraneous strains, maintains pressure communication to both sides of the diaphragm, and picks up electronically any movement of the diaphragm. The instrument primarily measures pressure differential. By maintaining one pressure at a very low value or any known value, the instrument can be used as an absolute pressure gage as shown in Fig. I-5. For calibration, the two sides are isolated from the outside and the pressure equalized. In operation, one side is connected to the unknown, and the other is held at reference pressure. In the system shown, the reference side is initially evacuated by the main vacuum system and then isolated. An ion pump is used to maintain the low pressure. A Varian 8-liter/sec unit was used in the present setup, and  $10^{-7}$  torr was maintained. Figure I-6 shows the experimental installation. The changes in capacitance on the two sides of the diaphragm are picked up by an ac bridge circuit in the control base. The ac voltage output is rectified and the dc output may be read in one of three ways:

- (1) The dc output voltage can be read as a meter deflection
- (2) The dc output voltage can be balanced out by the decade switches, which is the most accurate method
- (3) The voltage output can be used to drive a recorder, external voltmeter, etc.

Two sensing heads are needed to cover the range of 1,000 torr to  $10^{-5}$  torr. One head has full-scale deflection of 1,000, 300, 100 torr, etc., to 0.3 torr. The other has a similar range of from 1 torr to 0.0003 torr. This gage is insensitive to the nature of the gas being monitored.

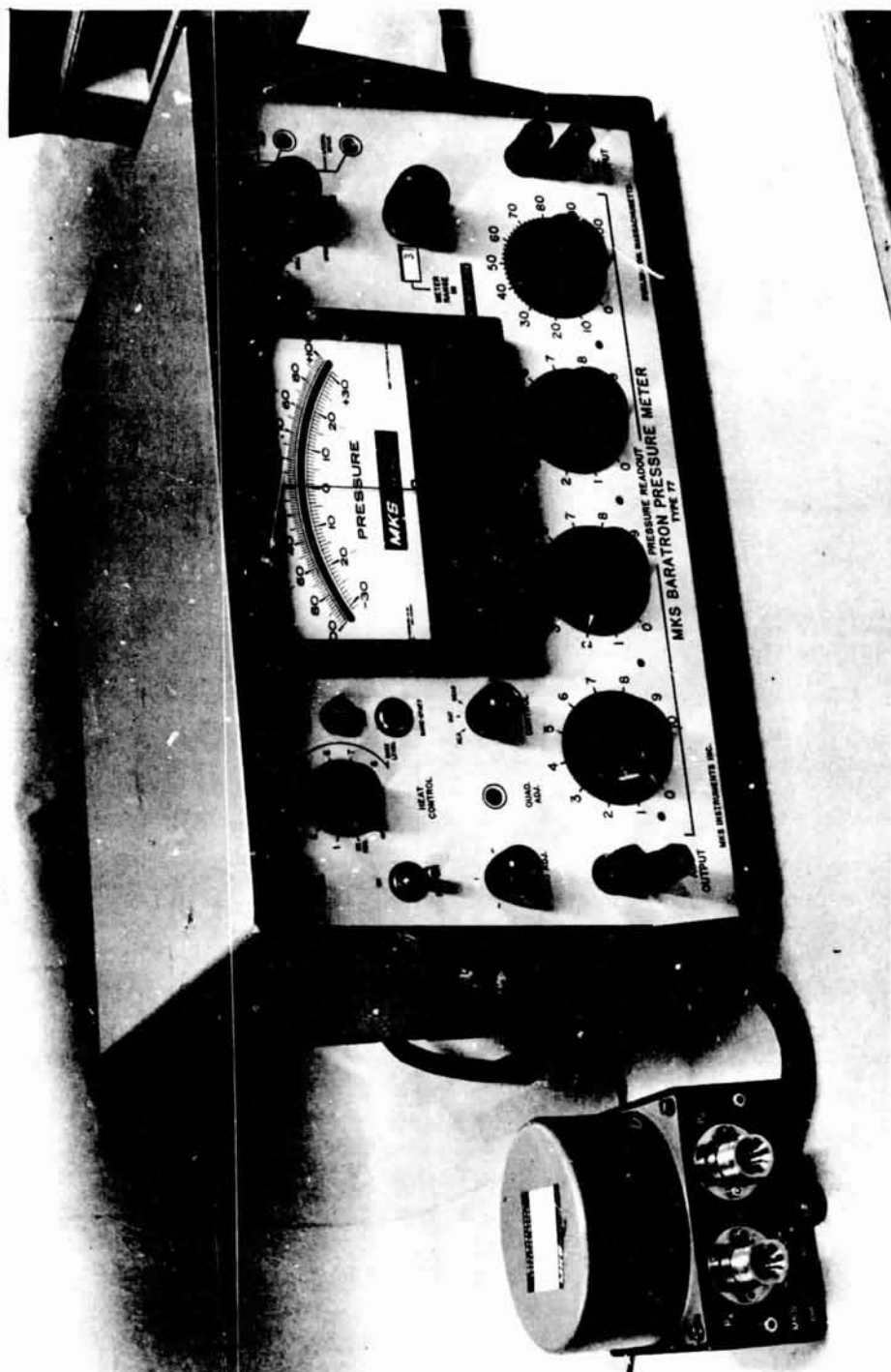
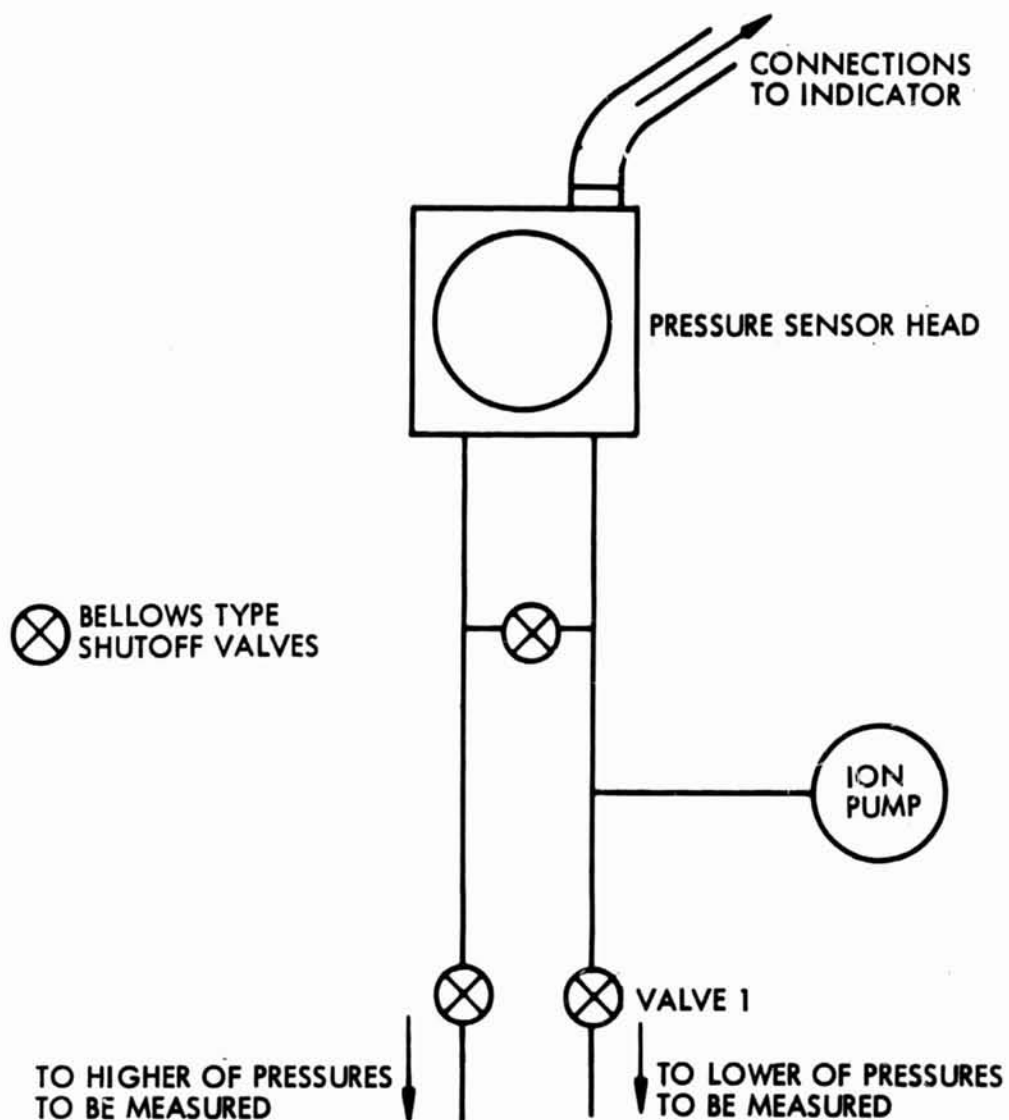


Fig. I-4 MKS Baratron Electronic Pressure Gage



**NOTE:**

IF DIFFERENTIAL PRESSURE IS TO BE MEASURED,  
VALVE 1 IS OPEN AND ION PUMP IS OFF.  
IF ABSOLUTE PRESSURE IS TO BE MEASURED,  
VALVE 1 IS CLOSED AND ION PUMP IS ON.

Fig. I-5 Connection Schematic of Baratron Absolute Gage



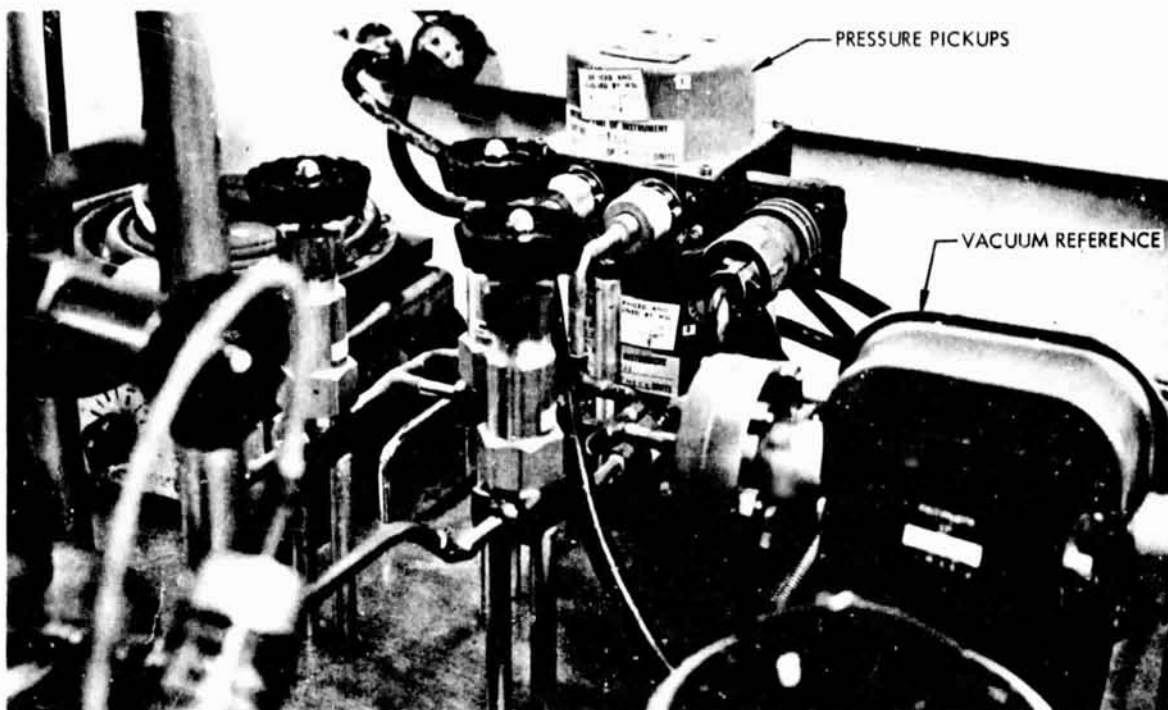


Fig. I-6 Installation of Pressure Pickups and Reference Vacuum System

A full investigation of the accuracy of the Baratron gage has been reported by Utterback and Griffith (Ref. I-1). This study shows that this type of capacitance manometer is probably the best available universal pressure sensor and that it should be reliably accurate to within a few percent at pressures as low as  $10^{-4}$  torr. The precise accuracy of this instrument in this low pressure range has not been determined because of the absence of standards. The Baratron gage was calibrated at pressures above 0.1 torr by the LMSC Primary Standards Laboratory and was found to have the following characteristics:

Hysteresis:	$\pm 0.005\%$ full scale on 1-torr head
	$\pm 0.1\%$ full scale on 1,000-torr head
Repeatability:	$\pm 0.02\%$ full scale plus 0.5% of reading
Linearity:	$\pm 0.15\%$ full scale

The zero drift of the gage over periods of days was on the order of  $3 \times 10^{-5}$  torr. This could be corrected rapidly by trimmers on the front of the control base. When adjusted



correctly and independently, both heads agreed to within 0.002 torr at 1 torr, which was the switching point from the high-pressure head to the low-pressure head. The extreme sensitivity of the gage was also helpful in checking for leaks. It was believed that  $4 \times 10^{-5}$  torr was about as low a reading as could reasonably be made. Below this pressure, the gage was too sensitive to read consistently because of its sensitivity to very slight system changes such as cycling of its own thermostat (which maintains the gage at a fixed temperature). The only problems associated with this instrument were the increased complexity of the installation and the high regulation temperature of its heads. They were controlled at 120° F and were a major contributor to the background outgassing.

Pressure and time readings were taken at all times by the test engineer. During the early stages of evacuation, while the specimen-chamber pressure was falling rapidly, an operator was present to change valve settings (described in a later section entitled "Pumpdown Technique"). The pressure subsequently changed less rapidly, and readings could be made less frequently. This also permitted the Baratron gage to be nulled so as to obtain more accurate data.

#### Partial-Pressure Gage

The partial-pressure gage used was a Varian gage. This gage is a type of magnetic mass spectrometer with two ion collectors arranged to operate for masses of 1 to 10 atomic mass units (amu) and 10 to 70 amu, respectively. This gage has an ion source that also acts as a total pressure gage. The ionized gas molecules are focused into a beam and directed toward the magnetic analyzer. Mass scanning is achieved by varying the ion accelerating voltage. Compared with other types of gas analyzers the resolution of this type of instrument is not exceptional; however, it is inexpensive and permits adequate detection of the most common outgas components, i. e., nitrogen, oxygen, carbon dioxide, and water.

The partial-pressure gage was inserted downstream from the chamber as shown in Fig. I-7. This gage inevitably picked up a certain amount of background gases. By

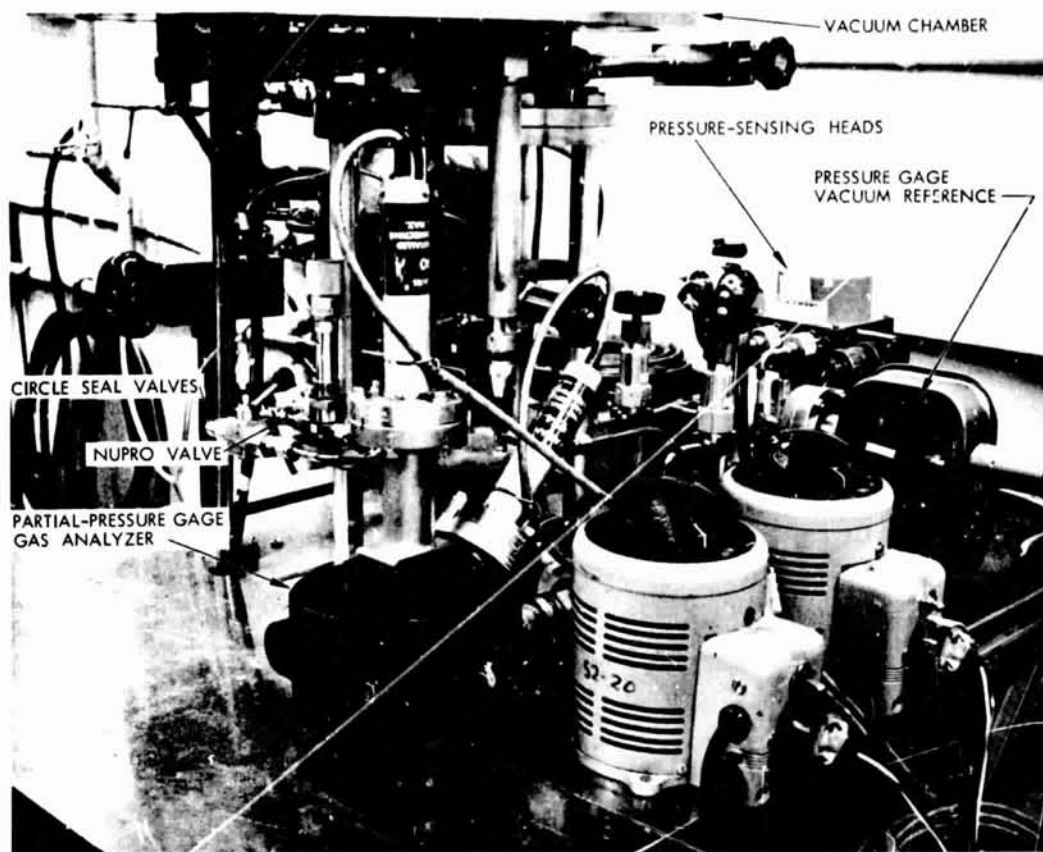


Fig. I-7 Partial-Pressure Gage Gas Analyzer

closing the series Circle-Seal Valve, it was possible to establish with great certainty whether a gas component was coming from the sample chamber or from the downstream area. This test was positive; in fact, the indicated background pressures often increased when the valve was closed.

The partial-pressure gage was easy to use and seemed well suited to testing of this type. When the first analyses were made, the principal constituent appeared to be nitrogen. However, the accelerating voltages for nitrogen, etc., did not coincide with those cited in the Varian manual; therefore, the gage was calibrated to known gases such as argon, nitrogen, oxygen, carbon dioxide, water vapor, and helium. After this calibration, the principal outgassing constituent was identified as water vapor.

## CHECKOUT OF APPARATUS

The apparatus was leak tested and the two Baratron heads baked out for a period of several days. Several days were required for the ion pumping system on the gage reference side to settle down before reaching a steady value of about  $10^{-7}$  torr. During this period, heat was applied to the insulation specimen chamber to speed outgassing. Thereafter, when the chamber was open for specimen insertion, a small steady flow of helium through the system was maintained via the purge-gas outlet valve, exhausting upward through the open chamber. Preliminary pumpdown runs on the empty insulation specimen chamber were made to establish appropriate procedures. Concurrently, modifications were made to the original valving between the chamber and the pumping system. As cited previously, the final arrangement was a 1/4-in. Circle-Seal valve in parallel with a Nupro bellows needle valve, both in series with another 1/4-in. Circle-Seal valve (Fig. I-7 ).

## PUMPDOWN TECHNIQUE

In the selected pumpdown technique, pumping was started by opening the series Circle-Seal valve with the Nupro valve open two turns. When the chamber pressure had fallen to 80 torr, the Nupro valve was opened fully (about seven turns). At 2 torr, the parallel Circle-Seal valve was opened. These stages corresponded to the speeds tabulated below.

<u>Adjustment</u>	<u>Pressure Range (torr)</u>	<u>Pumping Speeds (liters/sec)</u>
1	760 - 80	1.1
2	80 - 2	2.6
3	$2 - 3 \times 10^{-5}$	5.4

Another stage of pumping would have permitted  $10^{-6}$  torr to be reached; however, the reasonable limit of the Baratron gage is on the  $10^{-5}$  torr scale.

Pumping was achieved through use of the diffusion pump even when the specimen chamber pressure was one atmosphere. Upon opening the series Circle-Seal chamber valve, the pressure upstream of the diffusion pump rose to about 2 torr and then fell to normal pressures ( $<10^{-3}$  torr) in approximately 100 sec. It took slightly longer to reach normal pressures when the specimen chamber was cold. When the first valve adjustment was made at 80 torr, the pressure upstream of the diffusion pump rose to about 0.050 torr. The third adjustment caused no noticeable jump. These pressures were read on the upstream thermocouple gage. With the sample chamber pressure at 0.2 torr and steady (specimen in place), the high-vacuum plenum pressure was about  $10^{-7}$  torr. The control afforded by the valves using this technique was excellent. The needle valve was ideally sized for controlling low flow. An overall view of the test vacuum chamber and data acquisition system is shown in Fig. I-8.

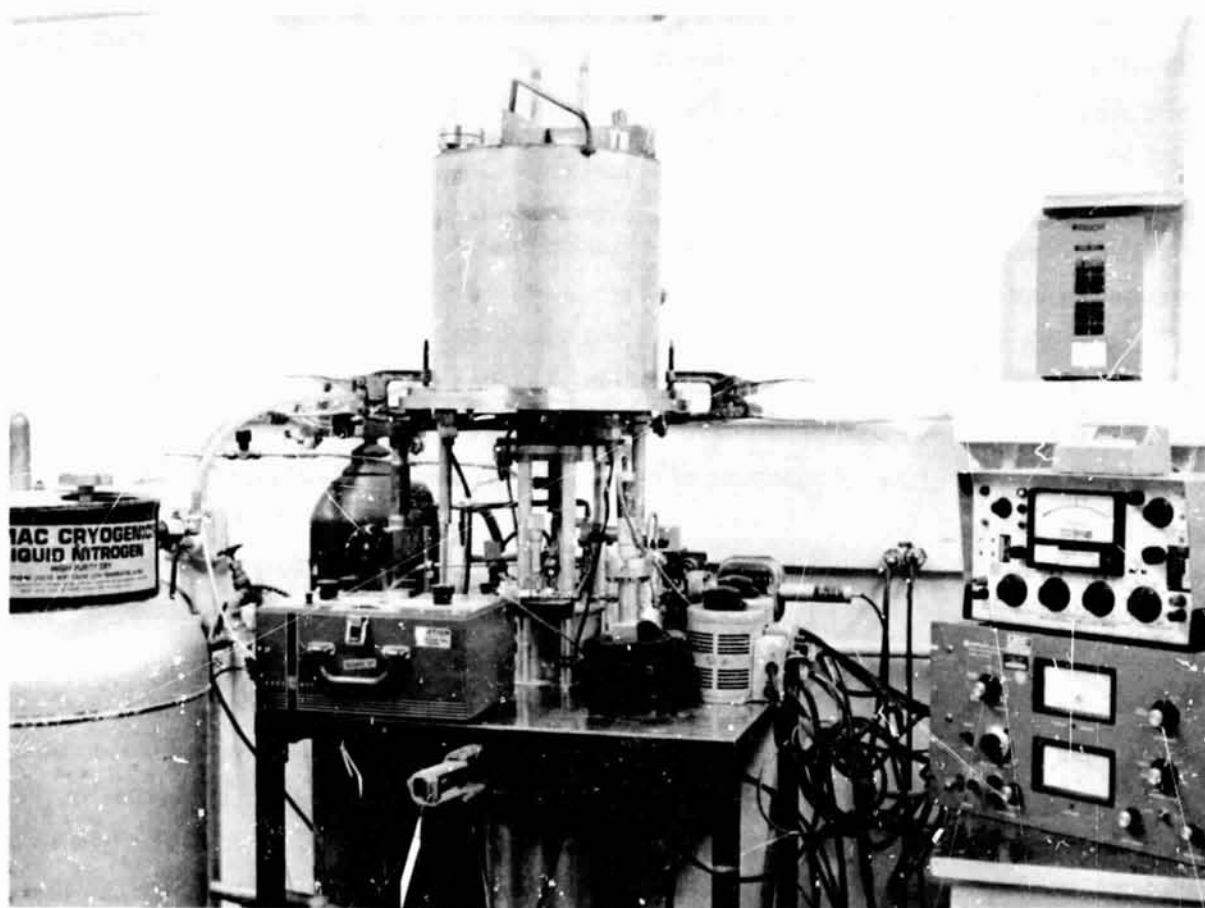


Fig. I-8 Outgassing Apparatus and Data Acquisition System

I-11

## REPRODUCIBILITY TESTS

Experimental procedures were set up based on the pumpdown technique just described. Initially, a series of empty-chamber tests were conducted to establish reproducibility. The insulation specimen chamber was evacuated and then filled to one atmosphere with helium. The cryogen tank was then removed and a gentle flow of helium maintained to prevent moist air from entering the system.

The specimen chamber was left open for 10 minutes, the estimated time required to insert a specimen for a full chamber run. The cryogen tank was then replaced, and a slight overpressure of 100 torr was maintained in the sample chamber while the flange bolts were tightened. It was not practical to leak-test the flange seal after every test; therefore, a very useful feature of the Baratron was employed: the Baratron can be nulled and the gage switched to more sensitive scales; a pressure of 860 torr then can be read by nulling on the 0.1-torr scale. (This can be done to within  $\pm 0.020$  torr.)

The cyclic temperature changes of the pressure-head thermostats produced similar pressure fluctuations, with the period being on the order of 1 minute when the specimen chamber was isolated, i. e., with all valves closed. Thus, satisfactory sealing was assumed when the pressure variation measured on the 0.1-torr scale showed only these background pressure oscillations. This criterion proved adequate. Pumpdown tests usually began from a pressure of 860 torr because of this procedure.

Initially, the test cycle consisted of pumpdown, chamber opening, chamber closing, and pumpdown, and was repeated four times before low-pressure repeatability was established. The first specimen was inserted on the fifth opening. Empty-chamber runs were made before each specimen test. As the tests proceeded, only two, and later only one, empty-chamber runs were made between tests since reproducibility was shown to be adequate. Empty-specimen-chamber runs lasted about 24 hr, while runs with specimens in the chamber lasted 72 to 96 hr. Correspondence between the two conditions was assumed between points on the pumpdown curves

at equal pressure rather than equal time. Errors introduced by this assumption cannot be eliminated from any outgassing tests unless elaborate compensatory devices are used to maintain identical pressure histories for full and empty systems. It is more practical to design the system so that the problem is minimized. In the present case, this was achieved by selecting a specimen-area-to-chamber-volume relationship that would cause most of the outgassing to take place at pressures above 0.02 torr. Above this pressure it was apparent that system outgassing was negligible, and the only variable was pumping speed which is not time dependent.

#### TEST PROCEDURES

The procedures used to conduct the tests in Task 5 were essentially the same for each test. Any differences pertained to the time between closing the specimen chamber and the beginning of the pumpdown. This was the period in which preconditioning took place.

Insulation material specimens were stacked so that with the chamber top in place a very slight pressure was applied to the layers. For the Mylar specimens the stack was 500 circular sheets; for the Tissuglas specimens the stack was 250 sheets. This number of sheets provided stack heights that filled the available 0.400-in space.

Purging at ambient temperatures was a straightforward operation. Helium was forced to flow through the insulation via the valves described earlier. The flow rate was monitored by a wet-test meter in the purge-gas outlet line. Hot purge was accomplished by heating flowing nitrogen/helium electrically to about 672°R. The gases did not have enough thermal capacity to warm the specimen chamber; therefore, electric heaters were placed on the outside of the chamber, and water was boiled in the cryogen tank. By these means, a purge temperature of approximately 670°R was achieved in 4 hr.

Cooling of the specimen was accomplished by filling the cryogen tank with an appropriate coolant. In the case of the liquid nitrogen tests, about 4 hr were necessary for the

insulation to reach a steady temperature of 160° R. The helium pressure was maintained at 760 torr throughout this period. The cooldown period required nearly 10 hrs, and an additional 24 hr passed between insertion of the sample and beginning of pumpdown. Tests at the ice point and at 430° R were made with water and 50/50 water/acetone in the cryogen tank, respectively. The tests at 472° R and 506° R were made with ethylene glycol/water and glycerine/water, respectively. A cooling coil was built into the cryogen tank for these cases so that the liquid could be partly frozen with liquid nitrogen to provide a constant-temperature, two-phase system.

In all tests, the outer vacuum jacket was in position and a vacuum of 0.001 torr provided to reduce heat leak to and from the specimen chamber.

#### DATA-REDUCTION TECHNIQUE

The primary measured data were pressure-time histories. Outgassing mass rate data were determined by applying Eq. (5.1).

$$Q_s = V \left[ \left( \frac{dP}{dt} \right)_o - \left( \frac{dP}{dt} \right)_s \right]_p \quad (5.1)$$

where  $\left( \frac{dP}{dt} \right)_o$  is the slope of the measured pressure-time curve for the empty chamber at pressure  $p$ ,  $\left( \frac{dP}{dt} \right)_s$  is the slope of the measured pressure-time curve for the chamber plus the insulation sample at the same pressure  $p$ , and  $V$  is the volume of the specimen chamber. This relation provides the outgassing rate,  $Q_s$ , as a function of pressure. A time is assigned to  $Q_s$  from the measured pressure-time curve for the full chamber. During pumpdown the empty chamber reaches a given pressure in a shorter time than for the full chamber; therefore, an assumption was made that  $\left( \frac{dP}{dt} \right)_o$  is independent of time and is only a function of pressure. This will be the case so long as the background outgassing is low. Another assumption implicit in the data evaluation is that the pumping speed is independent of the gas species being pumped from the specimen chamber.

## GAS ANALYSIS DATA

The partial pressure gauge could not operate at pressures above  $10^{-4}$  torr and was thus located downstream of the evacuation line, just above the diffusion pump. Even so, the pressure in the vicinity of the gage did not fall to  $10^{-4}$  torr until about 20 minutes of pumping so that all data taken were for times greater than this. The downstream location permitted the background outgassing to be determined by valving off the specimen chamber so that the partial pressure gauge sampled only the outgasses from itself and the plenum chamber.

It was originally intended to sample the outgasses continuously during all tests. However, it was found that in all cases the outgas was between 96 and 100 percent water vapor, with the balance being carbon dioxide and a trace of nitrogen. Since this data spread is about equal to the experimental accuracy, it is presented as a general conclusion that in all of the materials tested the outgas constituents were water vapor  $98 \pm 2$  percent, carbon dioxide  $\pm 1$  percent and nitrogen, traces.

To show how the data were taken Figs. I-9 through I-14 are presented. Figure I-9 shows a background scan for the region of the partial pressure gauge. Figure I-10 is a scan at the same elapsed time for the empty chamber. The difference between the scans of Figs I-9 and I-10 is due to the chamber and is principally due to carbon dioxide and water vapor. The nitrogen levels are practically identical. The peak on the left hand end of Fig. I-9 is a characteristic of the measuring device. Fig. I-11 to I-14 show scans for Test 1, plain double-aluminized mylar, at four elapsed time values. It is quite apparent that water vapor is the major constituent. In Fig. I-14, the absolute pressure values have fallen enough so that the chamber background, carbon dioxide, and nitrogen components, (see Fig. I-10) can be seen. Their magnitudes are not identical in Figs. I-10 and I-14 but are close enough to be assumed so in view of the differences in elapsed time, and by comparison with the earlier time scans.

All the scan data for all tests were similar to those presented for Test 1 and their presentation would be redundant.



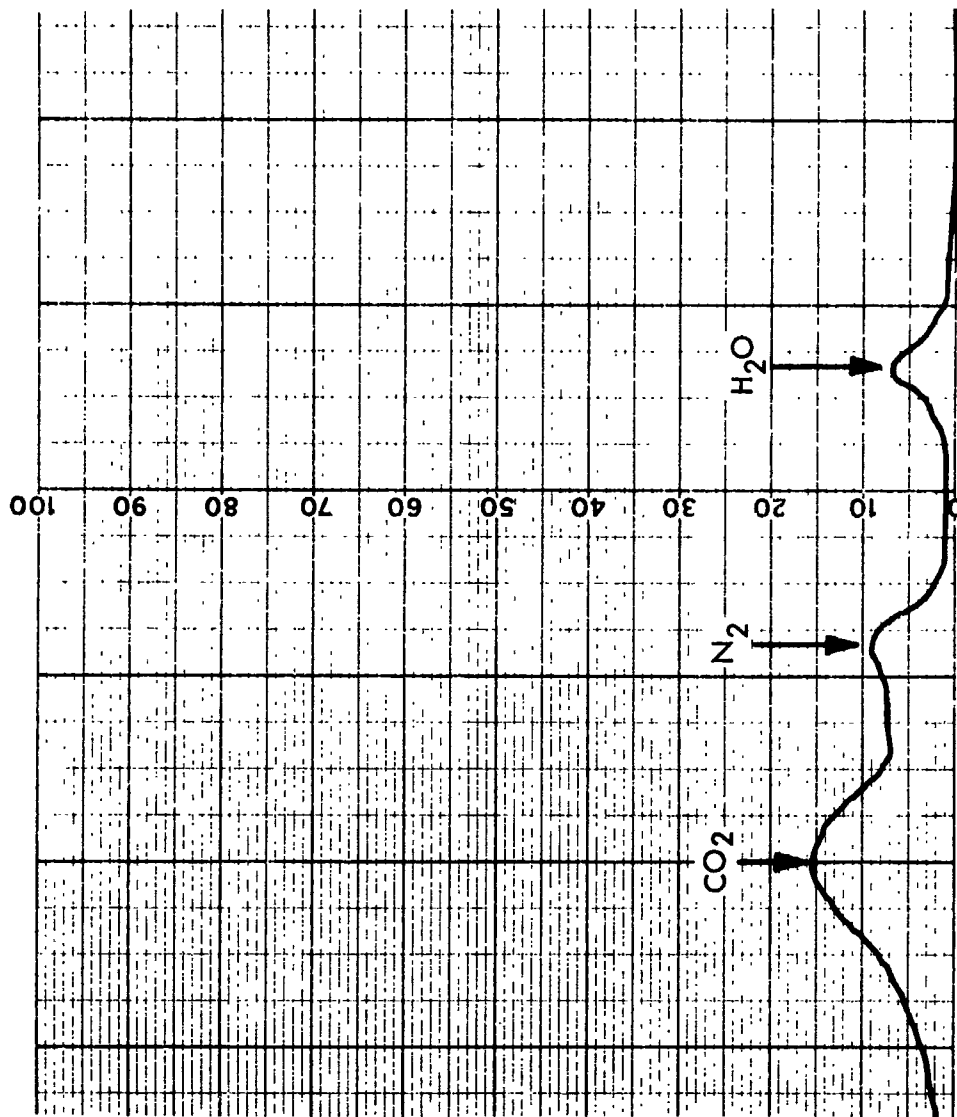


Fig. I-9 Empty Chamber Gas Analysis. Full Scale:  $10^{-8}$  Torr; Pumping Time: 5.45 hr; Chamber Pressure:  $5 \times 10^{-4}$  Torr

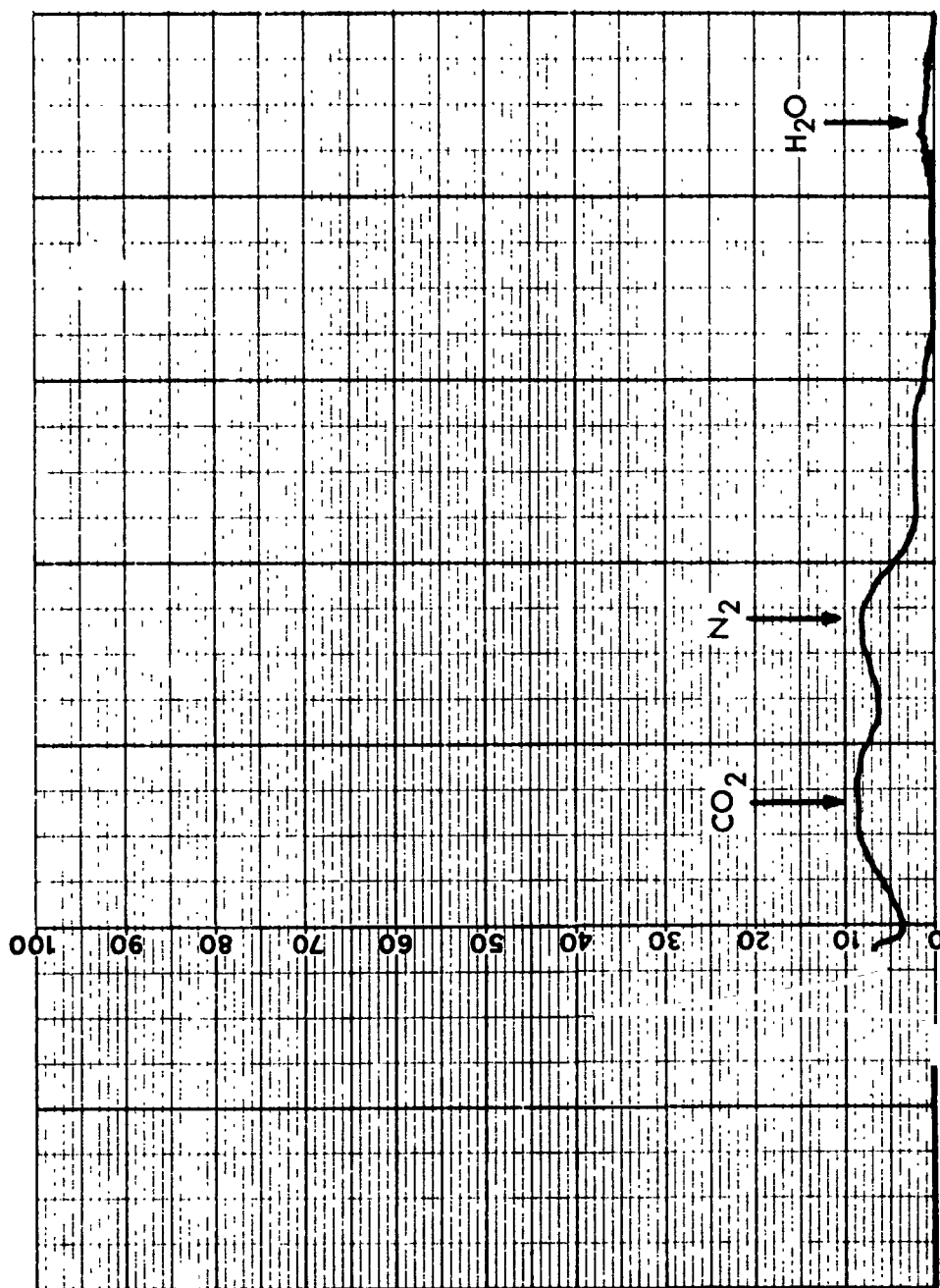


Fig. I-10 Background Scan for Gage Region. Full Scale:  $10^{-8}$  Torr; Pumping Time: 5.45 hr

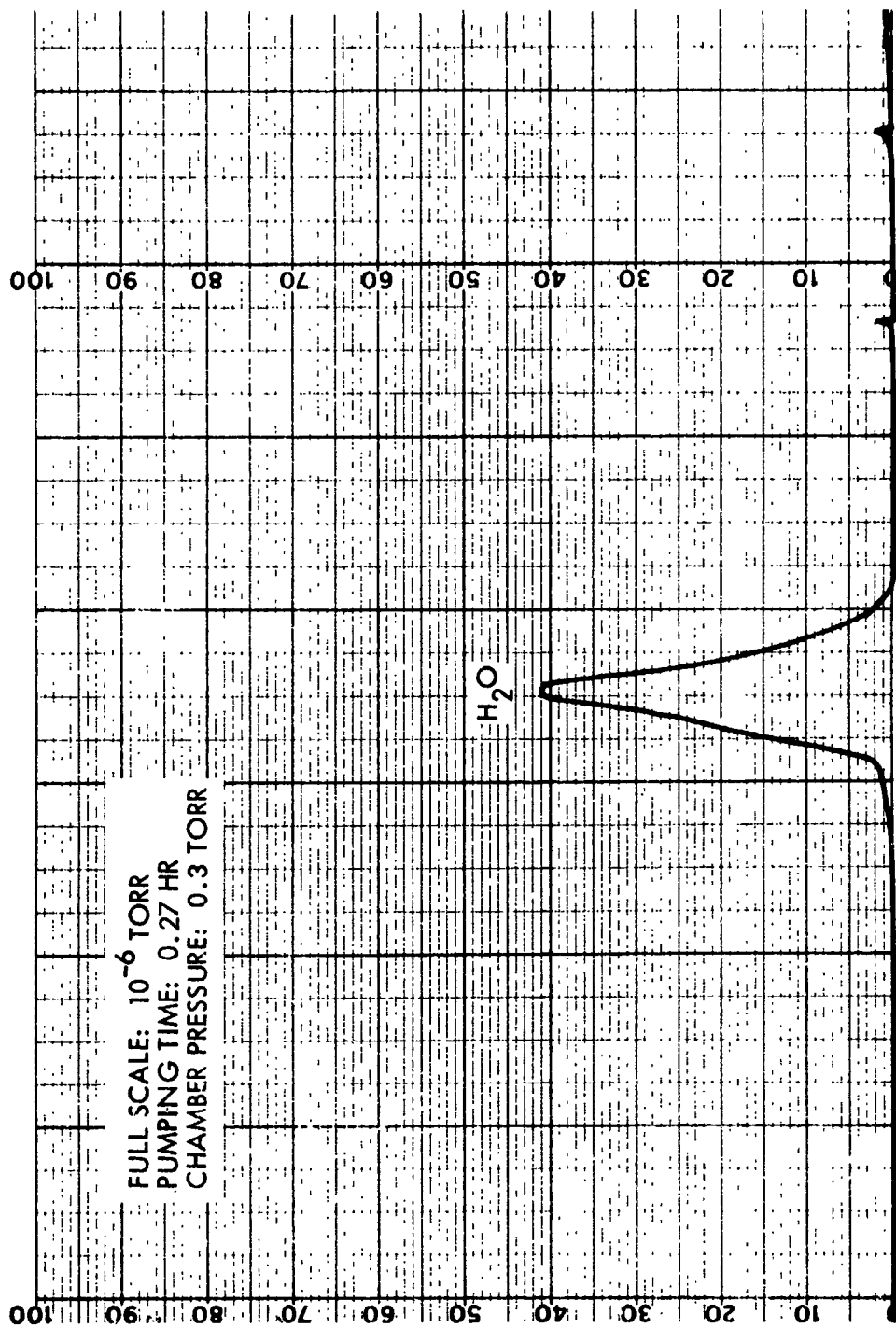


Fig. I-11 Test 1 - Partial Pressure Gage Scans at Four Different Times From Initiation of Pumpdown for Off-Shelf Double-Aluminized Mylar at 530° R: Part A

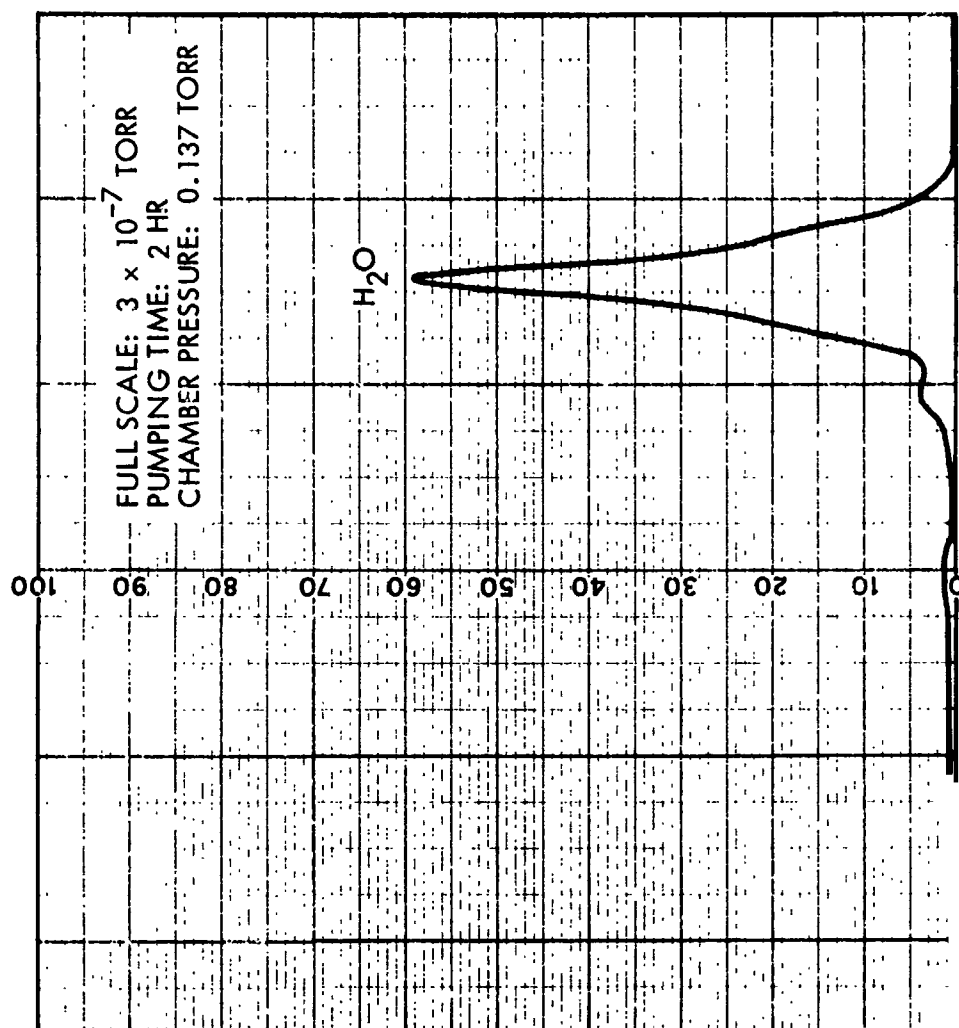


Fig. I-12 Test 1 - Partial Pressure Gage Scans at Four Different Times From Initiation of Pumpdown for Off-Shelf Double-Aluminized Mylar at 530° R: Part B

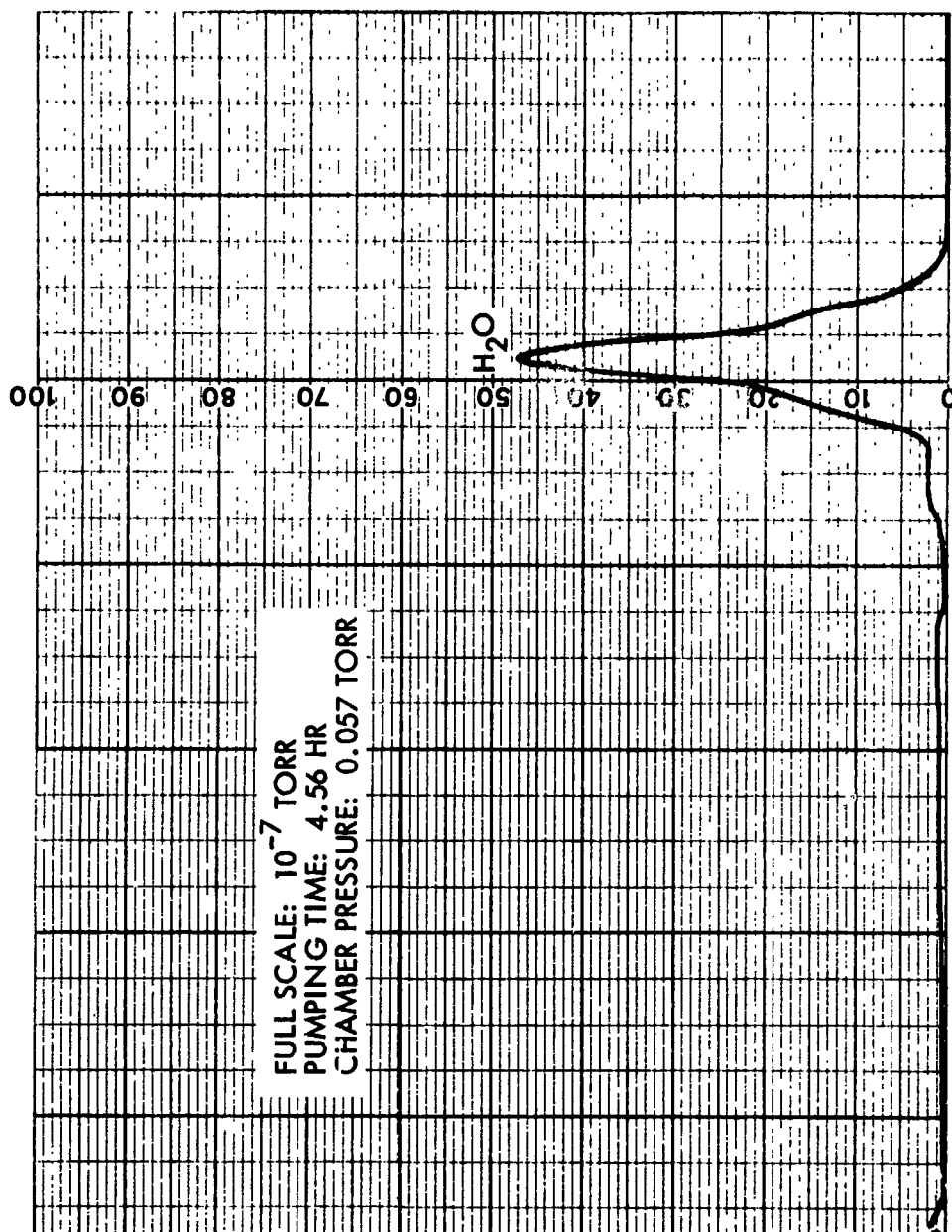
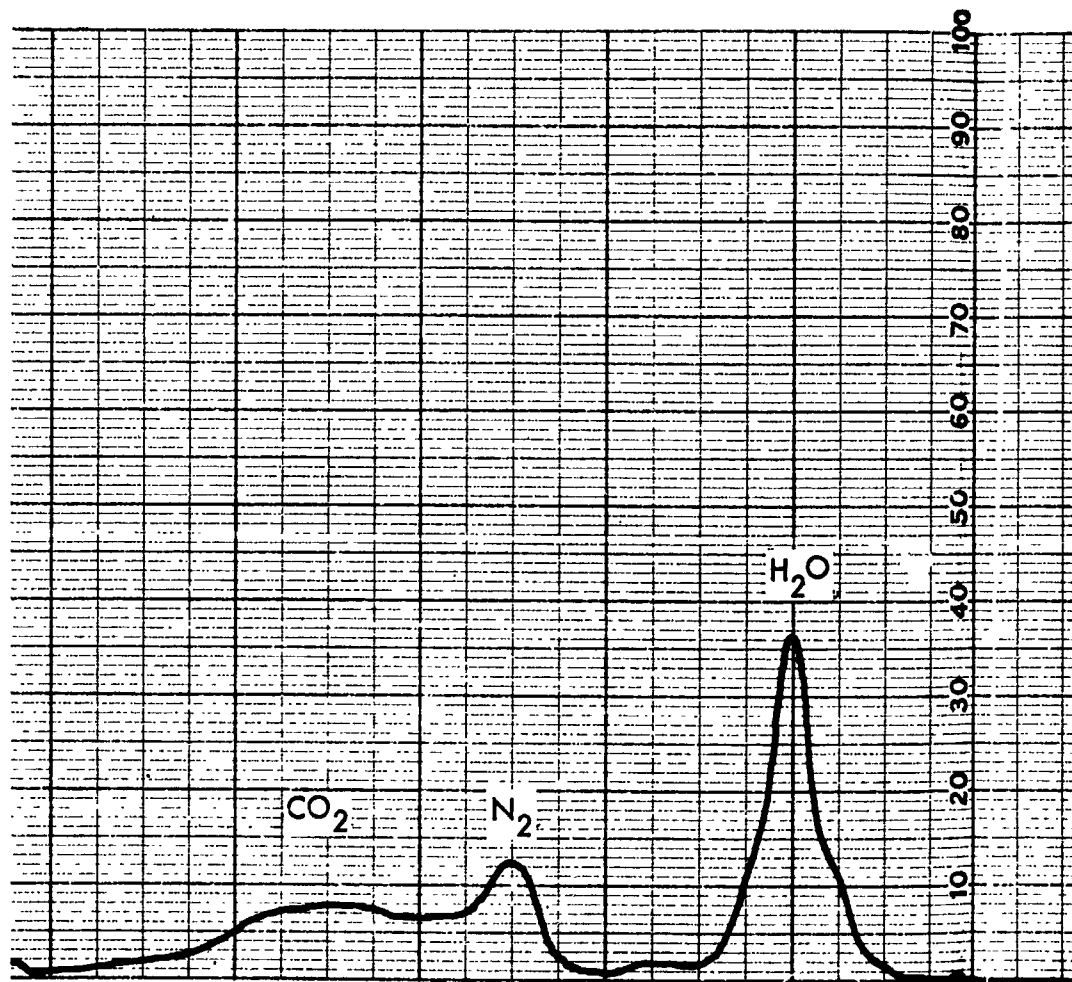


Fig. I-13 Test 1 - Partial Pressure Gage Scans at Four Different Times From Initiation of Pumpdown for Off-shelf Double-Aluminized Mylar at 530° R: Part C



FOLDBOUT FRAME /

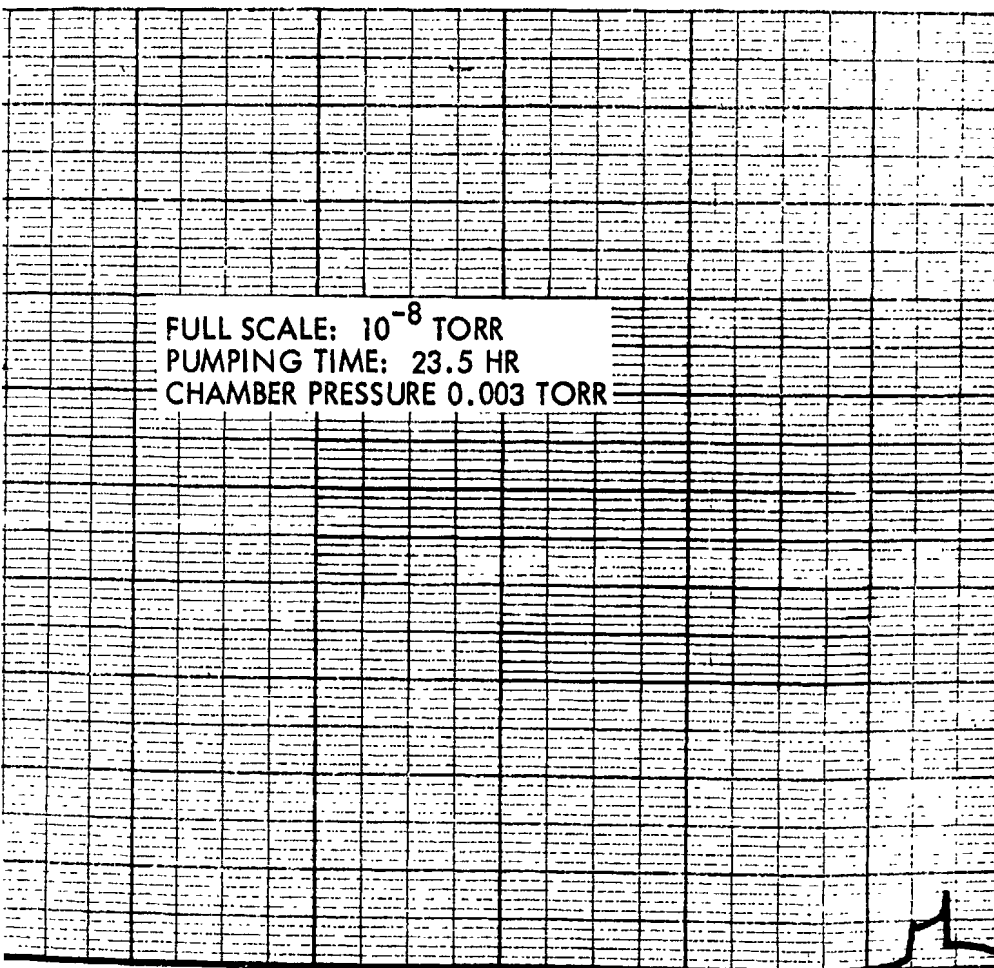


Fig. I-14 Test 1 - Pressure Gage Scans at Four  
Different Times From Initiation of Pump-  
down for Off-Shelf Double-Aluminized  
Mylar at 530° R: Part D

I-21

N70-30311

## Appendix J

### A METHOD FOR ESTIMATING "AS-INSTALLED" THERMAL CONDUCTIVITY VALUES

A comparison of large scale tank test results and cryostat results using the same insulation composite shows the heat flux increases on the order of 1.5 to 8.8 times. This increase is due to a number of factors such as insulation system design, fabrication technique, tank size and shape, compression due to button installations, number of layers, folding of flat materials over compound curvatures, variations in installed layer density, degradation due to parallel conduction in the multilayers around penetrations and radiation tunneling through joints.

Techniques are available for estimating the insulation degradation around penetrations (Ref. J-1); consequently, these effects can be accounted for. Also, since the total number of radiation shields and spacers are constant, the radiation heat flux component for the tank and the cryostat composites should be comparable.

Consequently, it appears the major portion of the increase in heat flux for installed insulations occurs due to an increase in the solid conduction component. If the simplified assumption is used that compression of the multilayers causes the increased heat flux values for tank installations, the following technique can be used to modify the thermal conductivity engineering relationships derived from cryostat tests to "as-installed" conductivity values using large scale tank test data. This technique is an over-simplification of the problem and only provides an indication of the thermal conductivity values to be expected. Nevertheless, until other techniques are developed for predicting the degradation due to insulation installation, these relationships are useful tools for estimating thermal performance of installed insulation systems.

The method shown below uses D-A-M/Tissuglas as an example. The remaining equations provided at the end of the Appendix for C-D-A-M/Tissuglas and NRC-2 used the same technique.



1. Solve for  $\bar{N}_s$  using the measured  $k_e$  from the large scale tank test results (where  $\bar{N}_s$  is a hypothetical layer density required to increase the solid conduction value to that which is measured on the tank)

$$k_e = 1.83 \times 10^{-12} (\bar{N}_s)^2 T_M + \frac{1.7\sigma (T_h^2 + T_c^2)(T_h + T_c)t}{(N - 1)[(2/\epsilon) - 1]} \quad (J.1)$$

solving for  $\bar{N}_s$  gives

$$\bar{N}_s = \sqrt{\frac{k_e - \frac{1.7\sigma (T_h^2 + T_c^2)(T_h + T_c)t}{(N - 1)[(2/\epsilon) - 1]}}{1.83 \times 10^{-12} T_M}} \quad (J.2)$$

where

$$\begin{aligned} k_e &= 1.74 \times 10^{-5} \text{ Btu/hr ft } ^\circ\text{R for a 9 ft } \sqrt{2} \text{ ellipsoidal LH}_2 \text{ tank (Ref. J-2)} \\ T_h &= 209^\circ\text{R} \\ T_c &= 40^\circ\text{R} \\ \bar{N}_s &= 274 \end{aligned}$$

2. Next, insert the ratio of  $(\bar{N}_s/\bar{N}_{\text{tank}}) = 274/140 = 1.96$  into the conductivity equation where  $\bar{N}_{\text{tank}}$  = installed layer density. This ratio increases the solid conduction component an amount equivalent to the increased heat flux noted for the large scale tank test results (as compared to the cryostat results).

$$(k_e)_{\text{tank}} = 1.83 \times 10^{-12} (1.96\bar{N})^2 T_M + \frac{1.7\sigma (T_h^2 + T_c^2)(T_h + T_c)t}{(N - 1)[(2/\epsilon) - 1]} \quad (J.3)$$

or D-A-M/Tissuglas

$$(k_e)_{\text{tank}} = 7.0 \times 10^{-12} (\bar{N})^2 T_M + \frac{1.7\sigma (T_h^2 + T_c^2)(T_h + T_c)t}{(N - 1)[(2/\epsilon) - 1]} \quad (J.4)$$

Similarly, the as-installed conductivity values for the other insulation composites were calculated to be:

C-D-A-M/Tissuglas

$$(k_e)_{\text{tank}} = 8.8 \times 10^{-12} (\bar{N})^2 T_M + \frac{1.7\sigma (T_h^2 + T_c^2)(T_h + T_c)t}{(N - 1) [(2/\epsilon) - 1]} \quad (\text{J. 5})$$

Test data from cylindrical SH<sub>2</sub> dewar 153-in. long by 42 in. diameter (Ref. J-3).

NRC-2

$$(k_e)_{\text{tank}} = 2.0 \times 10^{-10} (\bar{N})^2 T_M + \frac{\sigma (T_h^2 + T_c^2)(T_h + T_c)t}{(N - 1) \left( \frac{1}{\epsilon_a} + \frac{1}{\epsilon_b} - 1 \right)} \quad (\text{J. 6})$$

Test data from spherical 5-ft tank (Ref. J-4).

#### NOMENCLATURE FOR APPENDIX J

- $k_e$  = effective thermal conductivity, Btu/hr ft °R  
 $N$  = number of radiation shields  
 $N_s$  = hypothetical layer density, rad. shields/in.  
 $t$  = insulation thickness, ft  
 $T_c$  = temperature-cold boundary, °R  
 $T_h$  = temperature-hot boundary, °R  
 $\epsilon$  = emittance, dimensionless  
 $\sigma$  = Stefan-Boltzmann constant  $1.713 \times 10^{-9}$  Btu/ft<sup>2</sup> hr °R

## REFERENCES

- J-1. Lockheed Missiles & Space Co., Design of High-Performance Insulation Systems, Three-Dimensional Insulation Penetration Model, LMSC-A742593-111, Contract NAS-811347, 11 August 1965.
- J-2. -----,  $\text{LH}_2$  Storability in Space, LMSC-685104, 14 March 1968.
- J-3. -----, A Study of Hydrogen Slush and/or Hydrogen Gel Utilization, K-11-67, Contract NAS 8-20342, 11 March 1962.
- J-4. -----, Independent Missiles & Space Co., Independent Development Tests of 5' Tank, NRC-2 Insulation.

N70-30612

## Appendix K

### SAMPLE EFFECTIVE WEIGHT PENALTY CALCULATIONS

To illustrate how the effective weight penalty equations given in Task 1 were used to calculate performance data, sample calculations are provided here for the C-D-A-M/Tissuglas insulation composite. Refer to Task 1 for the derivation of the equations and input data used in the calculations.

In these calculations, the true optimum case was selected by determining the time when boiloff was initiated and comparing this time with the assumptions used in deriving the equations. The true optimum case can also be determined by calculating effective weight penalties for each case and selecting the minimum value.

#### EARTH DEPARTURE STAGE

Calculate  $\delta_{OPT_A}$  (boiloff assumed in Earth orbit) and  $\delta_{OPT_B}$  (no boiloff assumed in Earth orbit) and compare.

$$\delta_{OPT_A} = \sqrt{\frac{K_1 \Delta T_1 \theta_1 \phi_I}{\rho_1 \phi_{I_1} \lambda}}$$

$$\delta_{OPT_A} = \sqrt{\frac{(7.6 \cdot 10^{-6})(360)(720)(1.125)}{(0.75)(1.628)(1.90)}}$$

$$\delta_{OPT_A} = 0.095 \text{ ft} \quad (K.1)$$

$$\delta_{OPT_B} = \frac{K_1 A \Delta T_1 \theta_1}{Q_S - Q_P \theta_1}$$

$$\delta_{OPT_B} = \frac{(7.6 \times 10^{-6})(7968)(360)(720)}{1,025,640 - (373)(720)}$$

$$\delta_{OPT_B} = 0.021 \text{ ft} \quad (K.2)$$

Since  $\delta_{OPT_B} < \delta_{OPT_A}$  and no boiloff occurs in Case B, then  $(W'_T)_B < (W'_T)_A$  so the effective weight penalty is given by

$$(W'_T)_B = \phi_{I_1} \rho_I A \delta_{OPT_B}$$

$$(W'_T)_B = (1.628)(0.75)(7968)(0.021)$$

$$(W'_T)_B = 207 \text{ lb} \quad (K.3)$$

#### MARS BRAKING STAGE

Calculate  $\delta_{OPT_A}$  (boiloff assumed in Earth Orbit and Mars Transit)

$$\delta_{OPT_A} = \sqrt{\frac{K_1 \Delta T_1 \theta_1 \phi_1 + K_2 \Delta T_2 \theta_2 \phi_2}{\rho_I \phi_{I_2} \lambda}}$$

$$\delta_{OPT_A} = \sqrt{\frac{(7.6 \times 10^{-6})(360)(720)(1.208) + (1.7 \times 10^{-6})(180)(4960)(1.944)}{(0.75)(2.696)(190)}}$$

$$\delta_{OPT_A} = 0.118 \text{ ft} \quad (K.4)$$

Check to see if boiloff occurs in Earth orbit by calculating Earth orbit heating,  $Q_1$ , and compare to the heat storage capability,  $Q_S$ .

$$Q_1 = \left( \frac{K_1 A \Delta T_1}{\delta_{OPT_A}} + \dot{Q}_{P_1} \right) \theta_1$$

$$Q_1 = \frac{(7.6 \times 10^{-6})(5856)(360)(720)}{(0.118)} + (393)(720)$$

$$Q_1 = 380,880 \text{ Btu}$$

Since  $Q_S = 710,400 \text{ Btu}$   $Q_1 < Q_S$ . Therefore, no boiloff occurs in Earth orbit and Case A does not apply.

Next, calculate  $\delta_{OPT_B}$  (boiloff assumed in Mars transit only).

$$\delta_{OPT_B} = \sqrt{\frac{K_1 \Delta T_1 \theta_1 \phi_2 + K_2 \Delta T_2 \theta_2 \phi_2}{\rho_1 \phi_1 \lambda}}$$

$$\delta_{OPT_B} = \sqrt{\frac{(7.6 \times 10^{-6})(360)(720)(1.944) + (1.7 \times 10^{-6})(180)(4960)(1.944)}{(0.75)(2.696)(190)}}$$

$$\delta_{OPT_B} = 0.133 \text{ ft} \quad (K.6)$$

Check to see if boiloff occurs in Earth orbit.

$$Q_1 = \left( \frac{K_1 A \Delta T_1}{\delta_{OPT_B}} + \dot{Q}_{P_1} \right) \theta_1$$

$$Q_1 = \frac{(7.6 \times 10^{-6})(5856)(360)(720)}{0.133} + 393(720)$$

$$Q_1 = 370,080 \text{ Btu}$$

$$Q'_S = Q_S - Q_1 = 710,400 - 370,080$$

$$Q'_S = 340,320 \text{ Btu} \quad (K.7)$$

Therefore, no venting is required in Earth orbit.

Next, calculate the weight of boiloff in Mars transit.

$$W_{BO_2} = \left\{ \frac{\left[ \left( K_2 A \Delta T_2 / \delta_{OPT_B} \right) + \dot{Q}_{P_2} \right] \theta_2 - Q'_S}{\lambda} \right\}$$

where  $Q'_S = Q_S - \left[ \left( K_1 A \Delta T / \delta_{OPT_B} \right) + \dot{Q}_{P_1} \right] \theta_1$

$$W_{BO_2} = \left\{ \frac{[(1.7 \times 10^{-6})(5856)(180)/0.133] + 168}{190} 4960 - 340,320 \right\}$$

$$W_{BO_2} = 2934 \text{ lb} \quad (K. 8)$$

Since the boiloff number is positive, Case B is the correct optimum. Therefore, the effective weight penalty is given by

$$(W'_T)_B = \phi_2 (W_{BO_2}) + \phi_{I_2} \rho_I A \delta_{OPT_B}$$

$$(W'_T)_B = (1.944)(2934) + (2.696)(0.75)(5856)(0.133)$$

$$(W'_T)_B = 7278 \text{ lb} \quad (K. 9)$$

#### MARS DEPARTURE STAGE

Calculate  $\delta_{OPT_A}$  (boiloff assumed in Earth orbit, Mars transit and Mars orbit).

$$\delta_{OPT_A} = \sqrt{\frac{K_1 \Delta T_1 \theta_1 \phi_1 + K_2 \Delta T_2 \theta_2 \phi_2 + K_3 \Delta T_3 \theta_3 \phi_3}{\rho_I \phi_{I_3} \lambda}}$$

$$\delta_{OPT_A} =$$

$$\sqrt{\frac{(7.6 \times 10^{-6})(360)(720)(1.459) + (1.7 \times 10^{-6})(180)(4960)(2.195) + (5.5 \times 10^{-6})(310)(720)(3.334)}{(0.75)(5.941)(190)}}$$

$$\delta_{OPT_A} = 0.110 \text{ ft} \quad (K. 10)$$



Check to see if boiloff occurs in Earth orbit by calculating Earth orbit heating,  $Q_1$ , and compare to the heat storage capability,  $Q_S$ .

$$Q_1 = \left( \frac{K_1 A \Delta T_1}{\delta_{OPT_A}} + \dot{Q}_{P_1} \right) \theta_1$$

$$Q_1 = \left[ \frac{(7.6 \times 10^{-6})(6110)(360)}{(0.110)} + 393 \right] 720$$

$$Q_1 = 392,400 \text{ Btu} \quad (K.11)$$

Since  $Q_S = 745,920 \text{ Btu}$   $Q_1 < Q_S$ . Therefore, no boiloff occurs in Earth orbit and Case A does not apply.

Next, calculate  $\delta_{OPT_B}$  (boiloff assumed in Mars transit and Mars orbit).

$$\delta_{OPT_B} = \sqrt{\frac{K_1 \Delta T_1 \theta_1 \phi_2 + K_2 \Delta T_2 \theta_2 \phi_2 + K_3 \Delta T_3 \theta_3 \phi_3}{\rho_I \phi_{I_3} \lambda}}$$

$$\delta_{OPT_B} = \sqrt{\frac{(7.6 \times 10^{-6})(360)(720)(2.195) + (1.7 \times 10^{-6})(180)(4960)(2.195) + (5.5 \times 10^{-6})(310)(720)(3.334)}{(0.75)(5.941)(190)}}$$

$$\delta_{OPT_B} = 0.118 \text{ ft}$$

Check to see if boiloff occurs in Earth orbit by calculating Earth orbit heating,  $Q_1$ , and compare to the heat storage capability,  $Q_S$ .

$$Q_1 = \left( \frac{K_1 A \Delta T_1}{\delta_{OPT_B}} + \dot{Q}_{P_1} \right) \theta_1$$

$$Q_1 = \left[ \frac{(7.6 \times 10^{-6}) (6110) (360)}{(0.118)} + 393 \right] 720$$

$$Q_1 = 385,200 \text{ Btu}$$

$$Q_S > Q_1 \quad (K.13)$$

Therefore, no venting occurs in Earth orbit. Next, calculate the remaining heat storage capability in Mars Transit,  $Q'_S$ , and compare to the Mars Transit heating,  $Q_2$ .

$$Q'_S = Q_S - Q_1 = 745,920 - 385,200$$

$$Q'_S = 360,720 \text{ Btu}$$

$$Q_2 = \left( \frac{K_2 A \Delta T_2}{\delta_{OPT_B}} + \dot{Q}_{P_2} \right) \theta_2$$

$$Q_2 = \left[ \frac{(1.7 \times 10^{-6}) (6110) (180)}{(0.118)} + 168 \right] 4960$$

$$Q_2 = 911,648 \text{ Btu} \quad (K.14)$$

Since  $Q_2 > Q'_S$ , venting occurs during Mars transit and Case B is valid.

Next, calculate boiloff weights for Mars transit and Mars orbit and calculate overall weight penalty.

$$W_{BO_2} = \frac{Q_2 - Q'_S}{\lambda} = \frac{911,648 - 360,720}{190}$$

$$W_{BO_2} = 2899 \text{ lb} \quad (K.15)$$

$$W_{BO_3} = \left\{ \frac{\left[ \left( K_3 A \Delta T_3 / \delta_{OPT_B} \right) + \dot{Q}_{P_3} \right] \theta_3}{\lambda} \right\}$$

$$W_{BO_3} = \frac{\left[ \frac{(5.5 \times 10^{-6})(6110)(310)}{(0.118)} + 337 \right] 720}{190}$$

$$W_{BO_3} = 1611 \text{ lb} \quad (K.16)$$

Therefore, the overall weight penalty is

$$(W'_T)_B = \phi_2 W_{BO_2} + \phi_3 W_{BO_3} + \phi_{I_3} \rho_I A \delta_{OPT_B}$$

$$(W'_T)_B = (2.195)(2899) + (3.334)(1611) + (5.941)(0.75)(6110)(0.118)$$

$$(W'_T)_B = 14,941 \text{ lb} \quad (K.17)$$

A check is then made to see if Case C is valid (boiloff during Mars orbit only). First, calculate the optimum insulation thickness.

$$\delta_{OPT_C} = \sqrt{\frac{K_1 \Delta T_1 \theta_1 \phi_3 + K_2 \Delta T_2 \theta_2 \phi_3 + K_3 \Delta T_3 \theta_3 \phi_3}{\rho_I \phi_{I_3} \lambda}}$$

$$\delta_{OPT_C} =$$

$$\sqrt{\frac{(7.6 \times 10^{-6})(360)(720)(3.334) + (1.7 \times 10^{-6})(180)(4960)(3.334) + (5.5 \times 10^{-6})(310)(720)(3.334)}{(0.75)(5.941)(190)}}$$

$$\delta_{OPT_C} = 0.136 \text{ ft} \quad (K.18)$$

Then check to see if boiloff occurs in Earth orbit or Mars transit.

$$Q_1 = \left( \frac{K_1 A \Delta T_1}{\delta_{OPT_C}} + \dot{Q}_{P_1} \right) \theta_1$$

$$Q_1 = \left[ \frac{(7.6 \times 10^{-6})(6110)(360)}{(0.136)} + 393 \right] 720$$

$$Q_1 = 371,520 \text{ Btu} \quad (\text{K. 19})$$

$$Q'_S = Q_S - Q_1 = 745,920 - 371,520 = 374,400 \text{ Btu}$$

$$Q_2 = \left( \frac{K_2 A \Delta T_2}{\delta_{OPT_C}} + \dot{Q}_{P_2} \right) \theta_2$$

$$Q_2 = \left[ \frac{(1.7 \times 10^{-6})(6110)(180)}{(0.136)} + 168 \right] 4960$$

$$Q_2 = 902,720 \text{ Btu} \quad (\text{K. 20})$$

Since  $Q_2 > Q'_S$ , boiloff occurs during Mars transit and Case C is invalid.

## NOMENCLATURE FOR APPENDIX K

### Superscript

A	tank surface area, $\text{ft}^2$
K	thermal conductivity, $\text{Btu/hr ft } ^\circ\text{R}$
Q	heat, Btu
Q'	heat, Mars transit Btu
Q''	heat, Mars orbit, Btu
$\dot{Q}$	heat rate, $\text{Btu/hr}$
T	temperature, $^\circ\text{R}$
W	weight, lb
W'	effective weight, lb
$\delta$	thickness, ft
$\lambda$	heat of vaporization, $\text{Btu/lb}$
$\phi$	initial weight partial (partial of pounds in Earth orbit equivalent to pounds carried through designated mission duration), dimensionless
$\rho$	density, $\text{lb/ft}^3$
$\theta$	time, hr

### Subscript

1, 2, 3	Earth orbit, Mars transit, Mars orbit, respectively
A, B, C	Case A, B or C
BO	boiloff
I	insulation
OPT	optimum
P	penetrations
S	stored
T	total